Universidad Autónoma de Madrid
Facultad de Ciencias
Departamento de Física Teórica

Doctoral Thesis

Analytical and numerical models of radiative transfer in galaxies

---

Submitted by
Mario Romero Calleja
in fulfillment of the requirements for the degree of
Doctor in Astrophysics

Supervised by
Yago Ascasibar Sequeiros
(Departamento de Física Teórica, UAM)

and co-supervised by
Mercedes Mollá Lorente
(Departamento de Investigación Básica, CIEMAT)

Madrid, May 2022

Abstract

Galaxy formation and evolution involve several physical processes where stars, gas and dust play important roles. While analytical and numerical models have successfully accounted for most of them over the years, radiative transfer, that considers the interaction between light and the interstellar medium, is still *the elephant in the room*. Despite its importance as a driver of galactic evolution and as one of the main observables, radiation is often treated under very restrictive assumptions because an on-the-fly radiative transfer prescription is computationally expensive. This thesis advocates the importance and feasibility of including radiation by developing several models and codes with modest computational requirements. To illustrate this, I include radiation fields into the well-studied problem of supernova remnant evolution to study its effects, highlighting the main differences and improvements with respect to previous works in the literature. Then, I model the interstellar radiation field of the Milky Way in a self-consistent way, based on a distribution of stars, gas and dust predicted by chemical evolution models. This opens the door to use the interstellar radiation field both as a prediction to calibrate evolutionary galaxy models, as well as an efficient method to consider this ingredient on other physical processes, as done with supernova remnants.

Resumen

En la formación y evolución de galaxias hay involucrados varios procesos físicos donde las estrellas, el gas y el polvo juegan papeles importantes. Aunque los modelos analíticos y numéricos han ido añadiendo la mayoría de dichos procesos a lo largo de los años, el transporte radiativo, que considera la interacción entre la luz y el medio interestelar, sigue siendo *el elefante en la habitación*. A pesar de su importancia en la evolución de galaxias y de ser un observable primordial, la radiación sigue tratandose bajo aproximaciones muy restrictivas, ya que añadir una prescripción que incluya el transporte radiativo sobre la marcha es caro computacionalmente. Esta tesis defiende la importancia y la viabilidad de incluir dicha radiación desarrollando varios modelos y códigos con recursos computacionales modestos. Para ilustrarlo, incluyo campos de radiación en la evolución de remanentes de supernova, que es un problema bien estudiado, para señalar las diferencias y ventajas con trabajos previos de la literatura. Después, modelo el campo de radiación interestelar de la Vía Láctea de forma autoconsistente, a partir de una distribución de estrellas, gas y polvo, predicha por modelos de evolución química. Esto abre la puerta a usar el campo de radiación interestelar como una predicción que sirva para calibrar modelos de evolución de galaxías, tanto como método eficiente a considerar para otros procesos físicos, como se hizo con remanentes de supernova.

Declaration

I hereby declare that the thesis named *Analytical and numerical models of radiative transfer in galaxies* contains no material that have been submitted, in part of as a whole, for the award of any academic degree or diploma. I further state that this dissertation is the result of my own work, unless where specifically indicated. Some of the contents of this thesis have been published, or under review, to scientific journals, as the outcome of work done in collaboration. At the beginning of each chapter there is a note that contains information about authorship and publication status, and a more detailed list is presented below:

- **Chapter** 2. The work presented there is the result of my own work during the first and fourth year of the PhD. The contents of this chapter have not been submitted to a journal.
- **Chapter** 3. The work presented there is the result of my own work during the second to fifth years of the PhD. Some sections of this chapter are based on the publication *Impact of the ERF on the structure and evolution of SNRs*, by M. Romero, Y. Ascasibar, J. Palouš, R. Wünsch, and M. Mollá, published in MNRAS 505(4), pages 5301-5310 (2021). The work presented there have been made with my own code in combination with the publicly available code CLOUDY.
- **Chapter** 4. The chapter presents the results of a collaboration led by me during the fifth year of my PhD. The contents are based on the paper *Predicting interstellar radiation fields from chemical evolution models*, by M. Romero, P. Corcho-Caballero, I. Millán-Irigoyen, M. Mollá and Y. Ascasibar, submitted to MNRAS. The work presented there combines the publicly available codes CLOUDY and SKIRT with a code named MIXCLASK, written by me and P. Corcho-Caballero. I claim that I am the main developer and programmer of MIXCLASK. The initial conditions generated from chemical evolution models in section 4.2 were made by I. Millán-Irigoyen and M. Mollá, while the stellar population synthesis was made by P. Corcho-Caballero.
- **Appendices**. Derivations of appendices B.2 and C are my own work. Code introduced in appendix D has been written by me.

Mario Romero Calleja
Madrid, May 9, 2022

Agradecimientos

En primer lugar, quiero dar las gracias a mis directores Yago Ascasibar y Mercedes Mollá por acogerme todos estos años, que son muchísimos. Muchas gracias por dirigir la tesis doctoral, por vuestro consejo y ayuda. Sois unos científicos excelentes y tened muy claro que no podría haber tenido mejores mentores durante esta etapa, y también para las siguientes. Estoy en deuda con el departamento de Física Teórica de la Universidad Autónoma de Madrid por el soporte económico y por la plaza de ayudante. Estoy agradecido a Enrique Fernandez y Luís Labarga, así como al coordinador de los laboratorios en los que he estado de profesor, Ángel García, por darme la oportunidad de enseñar a estudiantes. También quiero extender mi gratitud a todos los profesores con los que he compartido las horas de docencia. También quiero agradecer al grupo de Física de Galaxias del Astronomical Institute of the Czech Academy of Sciences por darme la bienvenida cuando les visité. Gran parte de esta tesis esta motivada en los comentarios, consejos y discusiones realizadas con Richard Wünsch y Jan Palouš, en buscar ese 'heating' realista y calcularlo de la manera correcta. Muchas gracias por todo. Quiero dar las gracias a Alexander Knebe por su orientación a la hora de escribir códigos hidrodinámicos. Me has descubierto una pasión por la programación que va a ser irreemplazable para los años venideros. Esta tesis tampoco hubiera sido posible sin la introducción al código público Cloudy que me enseño Marina Rodríguez-Baras, por la que quiero darla las gracias. Quiero agradecer a Pablo Corcho-Caballero, Iker Millán-Irigoyen y Mara Pelayo-Baldárrago por todas las horas de trabajo y buenos momentos que hemos pasado.

Todo este esfuerzo no habría sido posible sin mis más queridos amigos y familiares. En ese aspecto, quiero agradecer muchísimo a mis amigos de toda la vida, Carlos, Bea y Álvaro, por todo el apoyo emocional que me han dado durante estos años. Querría agradecer a mis padres, Javier y Lorena, por ser la voz de la razón durante el doctorado. Extiendo esta gratitud a el resto de mis familiares, que me han apoyado también. Estoy agradecido a mis amigas Miriam y Vero, con quienes he compartido muchos buenos momentos, cafés, chocolates y churros. Doy las gracias a Ángel, Álex y Esther por todo el tiempo compartido jugando varios juegos online (y no tan online), que realmente me han ayudado a desestresarme durante el doctorado. Lucía, David, Iván, Ana, Daniel y Matías; aprecio mucho todas las comidas y buenos momentos que he compartido con todos vosotros en estos años.

Para finalizar, también quiero agradecerte a ti, lector, por tomarte tu tiempo para leer estas lineas. Esta tesis es la culminación de muchos años de sudor y sangre, pero también el orgullo y la alegría de un trabajo bien hecho. También marca el final de un largo capítulo de mi vida. No podría ser más feliz si esta tesis te ayuda a mejorar tu propio conocimiento y trabajo de investigación.

Muchísimas gracias por todos estos años,
Mario Romero.

Acknowledgements

First and foremost, I want to thank to my supervisors Yago Ascasibar and Mercedes Mollá for guiding me all these years, which are a lot. Thank you very much for supervise this thesis, your help and guidance. You are excellent researchers and bear in mind that I could have not asked for better mentors during this phase, and also for the following ones. I am indebted to the Departamento de Física Teórica de la Universidad Autónoma de Madrid for the financial support and the position of teaching assistant. I am grateful to Enrique Fernandez and Luís Labarga, as well as to the coordinator of the labs I have taught, Ángel García, for the opportunity to teach students. I also want to extend this gratitude to all teachers with whom I have shared teaching hours. I want to give my gratitude to the Physics of Galaxies group in the Astronomical Institute of the Czech Academy of Sciences for welcoming me when I visited them. A big amount of this dissertation is motivated on the comments, discussions and advice given by Richard Wünsch and Jan Palouš, in searching a realistic heating and to compute it correctly. I want to thank Alexander Knebe for his guidance in writing hydrodynamic codes. You have discovered me a passion for programming that it is going to be invaluable for coming years. This thesis

would have not been possible without the introduction to the public code Cloudy given by Marina Rodríguez-Baras, who I want to thank. I would like to thank Pablo Corcho-Caballero, Iker Millán-Irigoyen and Mara Pelayo-Baldárrago for all working hours and good moments we have shared.

All this effort would have not been possible with my dearest friends and family. In that regard, I greatly want to thank my longtime friends Carlos, Bea and Álvaro for all the emotional support they gave me during these years. I would like to thank my parents, Javier and Lorena, for being the voice of reason during my PhD. I also extend this gratitude to my other family members, who have greatly supported me as well. I am grateful to my friends Miriam and Vero, with whom I have shared very good moments, coffee, chocolates and churros. I thank to Ángel, Álex and Esther for all the time shared playing several online games (and not-so online ones), that really helped me to de-stress during my PhD. Lucía, David, Iván, Ana, Daniel and Matías; I truly appreciate all the meals and good moments we shared with all of you across these years.

Finally, I also want to thank you, the reader, for taking your time to read these lines. This thesis is the culmination of several years of my sweat and blood, but also the pride and joy of a work well done. It also marks the end of a long chapter in my life. I could not be happier if this thesis helps you to improve your own knowledge and research work.

Thank you very much for all these years,
Mario Romero.

Contents

The Elephant in the Room **7**

1 Basics of radiative transfer **10**
1.1 Brightness, mean intensity and luminosity . . . 10
1.2 Light interaction with the ISM . . . 10
1.2.1 Emission . . . 11
1.2.2 Absorption and scattering . . . 11
1.2.3 The equation of radiative transfer . . . 12
1.3 Gas interaction with light . . . 12
1.3.1 Radiative cooling and heating . . . 12
1.3.2 Shielded gas, and its relevance in the ISM . . . 14
1.4 The interstellar radiation field . . . 14

2 Analytical Models of Supernova Remnants Turning Radiative **16**
2.1 Basics of supernova remnants . . . 16
2.1.1 Canonical SNR evolution . . . 16
2.1.1.1 Ejecta-dominated phase . . . 17
2.1.1.2 Sedov-Taylor phase . . . 17
2.1.1.3 Snowplough phases . . . 18
2.1.2 Non-canonical evolution . . . 18
2.1.3 Characterizing the fate of a SNR . . . 18
2.1.3.1 Radiative (canonical) SNR . . . 18
2.1.3.2 Non-radiative SNR . . . 19
2.2 Modelling SNR temporal evolution . . . 20
2.3 Analytical solutions from energy balance . . . 21
2.3.1 Low-density regime . . . 21
2.3.2 Evolution to a radiative phase . . . 21
2.3.3 Pressure-Driven Snowplough . . . 22
2.3.4 Performance against numerical simulations . . . 23

3 Impact of an External Radiation Field on Numerical Supernova Remnants **25**
3.1 Eulerian fluid dynamics for supernova remnants . . . 25
3.1.1 Code structure . . . 27
3.1.1.1 Flux computation . . . 27
3.1.1.2 Time integration . . . 28
3.1.1.3 Computing pressure and thermodynamic variables . . . 29
3.1.1.4 Finding next timestep . . . 29
3.1.1.5 Adaptive Mesh Refinement . . . 30
3.1.2 Test cases . . . 30
3.1.2.1 Sod shock tube . . . 30
3.1.2.2 Comparison against FLASH . . . 30
3.1.3 Detecting shocks in supernova remnants . . . 32
3.2 Supernova remnants in the solar neighborhood . . . 32
3.2.1 The pre-supernova interstellar medium . . . 32
3.2.1.1 The average radiation field approximation . . . 32
3.2.1.2 Cooling and heating functions . . . 34
3.2.2 Supernova remnant evolution under a external radiation field . . . 35
3.2.2.1 Initial conditions . . . 35
3.2.2.2 Energy and momentum injection to the ISM . . . 37

3.2.2.3 Internal structure of the shell . . . 39
3.2.2.4 Limitations of this analysis . . . 42
3.2.2.5 Implications . . . 42
3.3 Supernova remnant evolution at extreme environments . . . 43
3.3.1 Initial conditions and SNR scenarios . . . 43
3.3.2 Radius, energy, momentum and luminosity . . . 44
3.3.3 Quantitative analysis of the SNR outcome . . . 44

4 The Interstellar Radiation Field from a Distribution of Stars, Gas and Dust 49
4.1 Modelling an external radiation field self-consistently . . . 49
4.1.1 Mixing CLOUDY and SKIRT . . . 49
4.1.1.1 The configuration input files . . . 51
4.1.1.2 SKIRT implementation . . . 51
4.1.1.3 CLOUDY implementation . . . 52
4.1.1.4 Iterative process and convergence . . . 53
4.1.2 Test case: HII region . . . 54
4.2 The interstellar radiation field of the Milky Way Galaxy . . . 55
4.2.1 Description of the selected Chemical Evolution Models . . . 55
4.2.1.1 MULCHEM model . . . 55
4.2.1.2 MMA model . . . 56
4.2.2 Stellar population synthesis . . . 57
4.2.3 MIXCLASK setup . . . 58
4.2.4 Results . . . 58

5 Final Remarks 61
5.1 Effects of the radiation field . . . 61
5.1.1 Structure, evolution and feedback of SNR . . . 61
5.1.2 Other environments and applications . . . 62
5.2 The technical side of this thesis . . . 63
5.3 Conclusions . . . 65
5.4 Conclusiones . . . 66

Bibliography 68

A Default Cloudy Abundances used in this Thesis 77

B Adiabatic Spherical Blastwaves 79
B.1 Shock jump conditions . . . 79
B.2 Internal structure . . . 79
B.2.1 Validating approximate profiles . . . 81

C Euler Time Derivatives in Cylindrical and Spherical Coordinates 83

D Proof-of-Concept of a Radiative Transfer Code 85
D.1 Some test cases . . . 85

The Elephant in the Room

The main components of a galaxy are dark matter, stars, and the interstellar medium (ISM). The latter is further subdivided in gas, where a few phases with different thermal and chemical states coexist in approximate pressure equilibrium; dust, made of very small solid particles and complex molecules; cosmic rays, i.e. electrons and bare nuclei moving at relativistic speeds; magnetic fields; and finally the photons that pervade the ISM, known as the interstellar radiation field (ISRF). A very basic picture of how these actors interplay with each other, alongside other events and processes that take place within a galaxy, is illustrated in Figure 1.

A star is a spheroidal entity that undergoes thermonuclear fusion (mainly H to He), which in turn prevents its gravitational collapse. They are in a galaxy in different types and properties. Here, I am using a classification based on their time span:

1. **Young stars**: These stars are massive (> 8 $M_\odot$) and the minority among all stars. However, they emit huge amounts of UV radiation into the ISM, enough to generate the warm ISM of Figure 1. These stars are called young because of their short lifetime, between 3 Myr and 30 Myr (Ferrière, 2001). When they die, they collapse under their own gravity and explode as supernovae (SNe), leaving either a neutron star or a black hole at their former location, as well as a shock wave that produces a hot ISM behind it for a very long time. The whole structure imprinted into the ISM, that is the shock wave and the hot interior, is called supernova remnant (SNR).

2. **Old stars**: Unlike their counterparts, they are less massive, more common, and they can live for several billion years, hence the name 'old'. Their deaths are not as violent as those of young stars. They release some of their gas as a planetary nebula, outshining the luminosity of a young star and leaving the naked core of the star as a white dwarf. In some cases, white dwarfs can also generate a SNR (for more details, see Maoz et al., 2005).

On the other hand, this thesis will consider only three phases for the ISM:

1. **Cold medium**: $T < 100$ K, $n > 100$ cm^{-3}. It consists of cold atomic gas and dispersed molecular clouds, well protected from radiation in the ISM. Half of the total gas mass is in this state, while occupying less than a 5 % in volume.

2. **Warm medium**: Composed of atomic and ionized material with temperatures in the $10^4 - 10^5$ K range and densities between 0.1 to 1 cm^{-3}. It coexists in equilibrium with the cold medium (e.g.: Wolfire et al., 1995) due to the existence of the ISRF that prevents the gas cooling at these temperatures.

3. **Hot medium**: Very ionized gas with a very low density (10^{-2} cm^{-3}) with a temperature of $T \sim 10^6$ K. Therefore, there is little gas mass is in this phase, but it covers a significant volume in the ISM. This phase is generated and maintained by supernova remnants (McKee and Ostriker, 1977) and the inefficient gas cooling.

In addition, a very important element for emission and absorption of light is the interstellar dust. Here, I consider two types of dust:

1. **Grains**: Solid particles with sizes between 0.3 nm to 0.3 μm made by heavy elements (Galliano et al., 2018).

2. **Polycyclic Aromatic Hydrocarbons (PAH)**: Complex chemical molecules featuring multiple benzene rings.

For a more interested reader in the ISM phases, see McKee and Ostriker (1977) and Ferrière (2001) for a review.

In terms of the processes involved in Figure 1, cold, molecular gas can form stars due to gravitational forces, and stars return part of it as hot ISM. Things become more complicated for the warm ISM. Cold gas can be ionized and sent to a warm state due to the interaction with cosmic rays, or by absorption of ISRF photons,

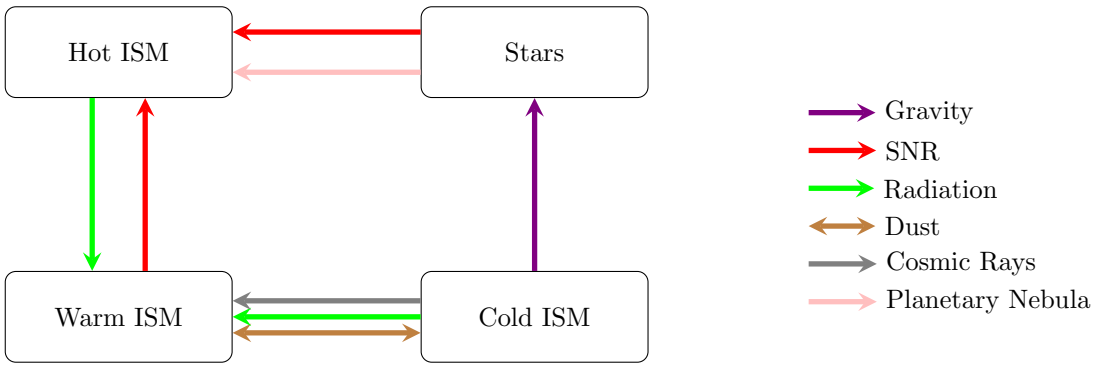

Figure 1: Basic scheme of the different states and actors found within a galaxy. Squares represent the main phases of the ISM plus stars, whereas arrows label main processes that intervene in each phase transition.

either by the interstellar gas, or by dust (e.g.: photoelectric effect), which also acts as catalyst of chemical reactions to form cold gas. Furthermore, it is possible generate warm gas from radiative cooling of hotter gas, but also heat it if a SNR sweeps through the gas.

This way, the literature is filled with several studies that address the big picture of Figure 1, as well as other works that deal individually with each one of these processes. Radiative processes become an *elephant-in-the-room* in most of these studies: the ISRF is always present within the galaxy, and observations rely on capturing photons in a telescope, but including it in models of galaxy formation and evolution is a formidable challenge.

When considered in the literature, there are two main approaches to radiative transfer. The first one is to solve it explicitly alongside other relevant equations, which makes the problem computationally expensive. This cost is, at minimum, similar to other ingredients needed for a full galaxy simulation, such as gas dynamics, chemical reactions, magnetic fields, etc. Therefore, it is necessary to use a supercomputer to perform such a simulation, using modules dedicated to perform this particular task in a optimal way (Grond et al., 2019; Wünsch et al., 2021). Alternatively, you can post-process the data of a simulation without radiation with several public codes to predict, for example, the ISRF, such as Mocassin (Ercolano et al., 2003, 2005), Sunrise (Jonsson, 2006), Skirt (Baes et al., 2003; Camps and Baes, 2020), Hyperion (Robitaille, 2011) or Radmc3d (Dullemond et al., 2012).

The other approach, which is far more popular, is to neglect the effect of the ISRF and assume that the gas is in purely collisional-ionization equilibrium (CIE). The problem is, however, that this is a very restrictive assumption, well known to break down in a variety of scenarios (e.g. Wiersma et al., 2009; Gnedin and Hollon, 2012; Oppenheimer and Schaye, 2013; Gnat, 2017; Robinson et al., 2021), and some authors have dealt with this issue by using pre-computed tables of gas cooling and heating under different illumination conditions (e.g.: Obreja et al., 2019; Ploeckinger and Schaye, 2020, Chapter 3).

Let me consider supernova remnants (SNR) as an example to illustrate the *elephant-in-the-room* character of radiative processes. To first order, a SN releases 10^{51} erg and leaves a SNR in the ISM that can last for a few million years, reaching a radius of ~ 100 pc at its late stages. We are talking about entities that have a similar life as young stars, covering the typical extent of a galactic thin disk, where new stars are forming. For that reason, they are one of the key ingredients of galaxy formation and evolution models (Naab and Ostriker, 2017). Early studies of SNR focused on the net energy injected by the SNR assuming spherical symmetry and a homogeneous ISM (Chevalier, 1974; Cioffi et al., 1988; Blondin et al., 1998; Thornton et al., 1998). In solar neighborhood environments, Thornton et al. (1998) found that only about 10 % or less of the injected energy is retained as kinetic energy, whereas the rest is radiated away. In the 2010 decade, there was a renewed interest in this problem, focusing more on the momentum injection into the ISM, since this quantity becomes constant in the late evolutionary stages of SNR evolution according to the analytical solution (e.g.: Oort, 1951; Ostriker and McKee, 1988; Bisnovatyi-Kogan and Silich, 1995). Modern works also studied SNR under less idealized conditions, such as non-homogeneous densities (Iffrig and Hennebelle, 2015; Kim and Ostriker, 2015; Li et al., 2015; Martizzi et al., 2015; Pittard, 2019), including magnetic fields (Petruk et al., 2016, 2018) or dust (Slavin et al., 2015; Martínez-González et al., 2018, 2019; Priestley et al., 2021). Some of them have even considered the radiation from the progenitor star (Green, 2014; Walch and Naab, 2015) or the SNR self-radiation (Sarkar et al., 2021). None of them have modelled the ISRF that is always present, although, as pointed by Badjin et al. (2016), the SNR structure and dynamics can be different due to the treatment of cooling (and hence radiation) at temperatures $< 10^4$ K.

In addition, modelling individual SNR in simulations at galactic (or higher) scales is impractical, as the temporal and spatial resolution required impose a fairly high computational cost. Therefore, phenomenological fits of the energy and momentum injected into the ISM by the SNR are often used, based on the results of single (or multiple) high-resolution SNR simulations. The most popular fit is the one provided by Thornton

et al. (1998), although I suggest to read Kim and Ostriker (2015); Li et al. (2015); Martizzi et al. (2015); Gentry et al. (2017) for more sophisticated solutions. On the other hand, analytical solutions for SNR evolution have also been developed since early times (for a review, see Ostriker and McKee, 1988; Bisnovatyi-Kogan and Silich, 1995). They are typically based on self-similar power-law solutions of the shock radius at different times of SNR evolution. Likewise, there are also semi-analytical models available today (Haid et al., 2016; Leahy and Williams, 2017; Jiménez et al., 2019) less idealized than these analytical solutions.

This thesis brings radiative transfer into the limelight, focusing on how to properly model radiation and its interaction with the ISM with humble resources, not beyond the reach of any modern personal computer. More precisely, I would like to argue that including radiative processes is of the utmost importance in the context of galaxy formation and evolution and advocate for the feasibility of doing so through different approximations at various levels that incur in low to moderate computational costs. To achieve that, I revisit the problem of SNR structure and evolution, from analytical models to numerical simulations, focusing on the differences associated to a more detailed treatment of the absorption and emission of photons.

In next Chapter, I will introduce the basic concepts of radiative transfer in an astrophysical context. Chapter 2 presents an analytical model of radiative SNR. There, I will show you how accounting for the luminosity of the remnant can produce analytical solutions that are consistent with numerical simulations and previous results in the literature. In Chapter 3, I develop my own hydrodynamic code to study SNR, where radiative cooling and heating are generated as a result of an external radiation field representing the ISRF in the solar neighborhood. At the end of that chapter, I extrapolate the results to more generic environments to see the extent of all the changes that may happen in the SNR evolution. Lastly, Chapter 4 will focus into modelling the ISRF. From a semi-analytical chemical evolution model that solves the system of differential equations associated to Figure 1), I use publicly available codes to compute the Milky Way ISRF and compare it with previous phenomenological results. I would like to argue that the ability to predict the ISRF is a stepping stone to better calibrate galaxy formation and evolution models, as well as to understand SNR evolution and feedback outside the solar neighborhood.

Chapter 1

Basics of radiative transfer

1.1 Brightness, mean intensity and luminosity

In astrophysics, radiation is measured with the specific intensity (or brightness), I. This magnitude measures the energy per unit of time, area and wavelength (or frequency), that is stored by an individual ray of photons (i.e.: also per unit of solid angle, Ω). In mathematical terms, this term I has two definitions, one for wavelengths and another for frequencies:

$$I_\lambda = \frac{dE}{dtdAd\Omega d\lambda} \quad ; \quad I_\nu = \frac{dE}{dtdAd\Omega d\nu}, \tag{1.1}$$

with both expressions related since $I_\lambda d\lambda = I_\nu d\nu$. Due to $\nu\lambda = c$, you can define a third intensity independent of wavelength or frequency as

$$\lambda I_\lambda = \nu I_\nu, \tag{1.2}$$

labelled in this thesis as its *neutral* definition, and it is valid with any radiation-related magnitude as long as it is not integrated in wavelength or frequency. Hereinafter, wavelength (I_λ) or neutral (λI_λ) definitions will be used in the text without loss of generality.

Although the specific intensity is the main quantity for computations, there are other variables that are convenient to be used in different cases. These are defined by integrating (1.1) in the solid angle (i.e.: all directions):

$$J_\lambda = \tfrac{1}{4\pi} \int_\Omega I_\lambda \; d\Omega' \tag{1.3}$$

$$F_\lambda = \int_\Omega I_\lambda \cos(\theta) \; d\Omega' \tag{1.4}$$

The first quantity is an average of all directions, and hence it takes the name of mean intensity. The second one is the energy per unit of time and wavelength that crosses a surface, which is the definition of a (radiative) flux. From the latter, it is possible to define the observed luminosity as the energy radiated by unit of time and wavelength of some entity by integrating in the surface dA:

$$\mathcal{L}_\lambda = \int_A F_\lambda \; dA \tag{1.5}$$

The three Eq. (1.3), (1.4) and (1.8) are used in different contexts in Astrophysics. The mean intensity is very useful for measuring the radiation within a continuous material such as the ISM, while the luminosity is more adequate for single entities such as stars. Fluxes, on the other hand, are necessary when dealing with observations. Since this thesis is theoretical, the flux will not be used as much here.

1.2 Light interaction with the ISM

A ray of photons travels through a space filled with material that alters the brightness along its path. There are three possibilities: emission, in which photons can be added through some sources; absorption, which is the opposite process; and scattering, where photons change their direction and can either increase or decrease the specific intensity.

In this subsection, I will explain the main radiative mechanisms of emission, and add some notes about absorption and scattering.

1.2.1 Emission

There are three emission processes that are relevant for this introduction:

1. **Black-Body emission**: Emitted by opaque matter in thermal equilibrium. That is, a body that absorbs all radiation and so only emits its own radiation. The intensity, considered isotropic ($I \neq I(\Omega)$), follows this spectrum:
$$I_\lambda = B_\lambda = \frac{2hc^2}{\lambda^5}(e^{\frac{hc}{\lambda k_B T}} - 1)^{-1} \tag{1.6}$$
This Eq. (1.6) has the relevant property that the wavelength at its maximum is associated to the temperature as: $T = b/\lambda_{max}$, where $b \approx 2898\,\mu$m K. For example, the optical band (≈ 0.4 to $0.7\,\mu$m) gives T in the range 7245 to 4140 K.

2. **Line emission**: These are produced by atoms, ions and molecules that are in an excited state for some reason, and then drops to a lower energy level by releasing a photon whose energy is the difference between levels, $\Delta E = \frac{hc}{\lambda}$. The probability to jump from one level to another are determined by the atomic physics, being some transitions more allowed than others. However, forbidden transitions does happen in Astrophysics as well. In particular, heavy ions (e.g.: NII, OIII, SIII...) reach a meta-stable level due to a collision with an electron, but if the medium density is very low, it is more common to their de-excitation by means of a forbidden transition[1] than from another collision.

3. **Bremsstrahlung**: Produced by accelerated charges. Specifically, in regions where collisions between charged particles (electrons, protons,...) can occur.

All these processes should be introduced in a macroscopic environment, where a big amount of particles are emitting photons. In that regard, a well-defined quantity is the energy emitted per unit of time, volume, wavelength and solid angle:
$$j_\lambda = \frac{dE}{dt dV d\Omega d\lambda} \tag{1.7}$$
dubbed as emissivity. Details about how to compute j_λ comes from complex calculations based on statistical mechanics, and lies outside the scope of this thesis. For a more interested reader, I refer to chapters 5 and 6 of Padmanabhan (2000).

In terms of brightness, the main change is that j_λ is per unit of volume instead of area, giving $dI_\lambda = j_\lambda ds$. Furthermore, emissivity can be also related with the emitted luminosity of an entity
$$L_\lambda = \iint_{V,\Omega} j_\lambda \, dV d\Omega \tag{1.8}$$
In contrast with observed luminosity (1.5), L_λ considers all photons from the source, unaltered due to the medium they are travelling. In this thesis, I consider only emitted luminosity (hereinafter just luminosity) to characterize the emission by different entities.

1.2.2 Absorption and scattering

For absorption, there are three major processes to bear in mind:

1. **Photo-ionization**: A process in which a photon has enough energy to unbound an electron from its atom (ion). In that regard, the most important ionization process is that of neutral Hydrogen. It happens when a photon has an energy equal or higher than 13.6 eV (i.e.: wavelengths of 91 nm and lower).

2. **Line Absorption**: Below the photo-ionization limit, the opposite process of line emission happens for photons whose energy is the difference between levels, exciting atoms/molecules that absorb said photons.

3. **Photoelectric effect**: Likewise, a photon with high enough energy, albeit lower than 13.6 eV to prevent H photo-ionization, can rip an electron from a dust grain.

From the intensity perspective, however, it is more illustrative to reclassify absorption and scattering into photon removal, also called extinction, and photon addition to the line of sight.

For the extinction, it is frequent to define a coefficient named opacity, α_λ (cm^{-1}), to represent the intensity loss along a line element ds, such as
$$dI_\lambda = -\alpha_\lambda I_\lambda ds \tag{1.9}$$

[1] Unlike allowed transitions, forbidden lines are labelled between brackets. For example, [OIII] $\lambda\lambda 4959, 5007$, where each λ tells us the number of wavelengths (in Angstroms).

In absence of sources of radiation, a medium with constant opacity will attenuate brightness as $I_\lambda(s) = I_\lambda(0)e^{-\alpha_\lambda s}$. The opacity is a function of the properties of the medium, as well as temperature and density. Hence, it is very common to define a quantity, called optical depth τ_λ, that stores the combined information of distance (i.e.: from $I_\lambda(0)$ to $I_\lambda(s)$) and optical properties of the material:

$$\tau_\lambda \equiv \int_0^s \alpha_\lambda \, ds \tag{1.10}$$

Two regimes can be distinguished following the value of τ_λ:

1. **Optically thin regime**: when $\tau_\lambda \ll 1$, it is said that media is transparent at that wavelength. Therefore, a negligible fraction of photons are either absorbed or scattered along the path and it is possible to see through the medium.

2. **Optically thick regime**: On the other hand, the medium is opaque to a wavelength if $\tau_\lambda \gg 1$. In radiative terms, it means that an observer cannot see what is inside the surface of an optically-thick medium, and also blocks any radiation that comes from behind.

To finish this subsection, I comment briefly how to deal with the photon addition due to scattering. Unlike extinction, where it does not matter to what new direction the photon is sent (of if it has been absorbed), for addition via scattering, however, you have to care from where the photon is coming, and if its wavelength (energy) changes, due to the scattering event. Needless to say that the complexity of this problem increases significantly, and going further would be out of the scope of this introduction.

1.2.3 The equation of radiative transfer

Once all processes have been addressed, the variation of brightness along one line of sight is

$$\frac{dI_\lambda}{ds} = j_\lambda - \alpha_\lambda I_\lambda + ... \tag{1.11}$$

Emission and extinction have been accounted in (1.11). Addition of photons by scattering is represented with the ellipsis, as for the most basic uses is typically ignored.

Analytical solutions of Eq. (1.11) can be found for very specific cases (see D.1 for some examples). In practice, solving Eq. (1.11) is a six-dimensional problem, as it involves the wavelength and directions (defined with two angle variables, ϕ and θ) per each point in space (x, y, z).

To handle with this task, the classical codes in the literature take two main strategies:1) On one hand, some codes, such as Trevr (Grond et al., 2019) and Treeray (Wünsch et al., 2021), trace rays (or cones) at different points and solve Eq. (1.11) explicitly for each one; 2) On the other hand, a different approach consists to follow the trajectories of particles, called packets, that represent photons. In this case, if a packet is emitted, absorbed or scattered is decided stochastically. Some examples of this methodology are Radmc3d (Dullemond et al., 2012) and Skirt (Baes et al., 2003; Camps and Baes, 2020).

In any case, solving radiation has two major technical issues. First, coupling Eq. (1.11) into other processes increases the computational cost of everything by adding new variables to track. Second, the radiation is coupled with the medium where it is travelling. This translates in that the original values of j_λ and α_λ are continuously modified, forcing the user to solve Eq. (1.11) iteratively until it converges.

1.3 Gas interaction with light

1.3.1 Radiative cooling and heating

Now, let me consider the other point of view. Radiation emitted by the gas removes energy from it, and vice-versa for absorption. In this aspect, it is common to define, for the gas, a thermal energy rate per unit of volume

$$\dot{u} \equiv \frac{dE}{dtdV} \tag{1.12}$$

or energy density rate. Equation (1.12) is a function of several thermodynamic variables. The most common ones are: the number of particles per volume, or number density, n; temperature, T; the mass fraction of metals (i.e.: elements heavier than He), or metallicity, Z; and the mean intensity field J_λ.

Energy loss is this context is called cooling, and it is generally complied as

$$\dot{u}_C = -n^2 \Lambda(n, T, Z, J_\lambda), \tag{1.13}$$

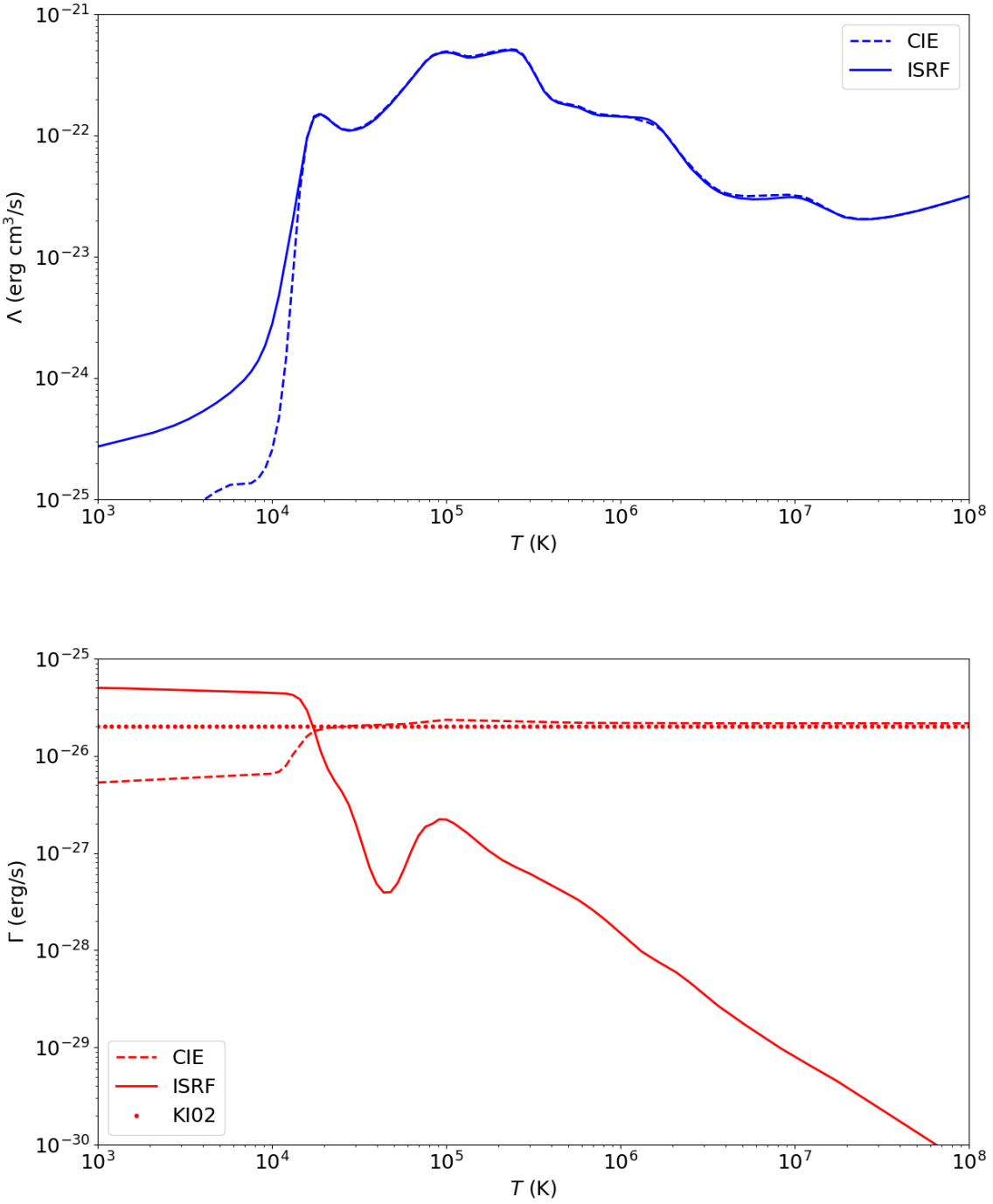

Figure 1.1: Top: Cooling function under Collisional Ionization Equilibrium (CIE, dashed line) and from the ISRF of Figure 1.2. Bottom: Heating rate for same cases plus Koyama and Inutsuka (2002) (KI02, dotted line). For both cases, $n_H = 1\,\mathrm{cm}^{-3}$ and neither dust nor cosmic rays are included.

where Λ is the bolometric cooling rate of the gas, more known as the cooling function. Top panel of Figure 1.1 displays a typical cooling function in the solar neighborhood and obtained with CIE approximation, being a good fit for $T > 10^4\,\mathrm{K}$. However, the important point is to know the processes that play a role at these temperatures. Bumps between $T = 10^4$ to $10^7\,\mathrm{K}$ are generated by line emission of metals, except the first one at $10^4\,\mathrm{K}$ which is generated by H. Bremsstrahlung is responsible of the cooling function increase at $T > 10^7\,\mathrm{K}$. Differences between both cases may have no effect for lower temperatures because other processes becomes more relevant (e.g.: dust and cosmic rays, which are not included in Figure 1.1 in order to show only radiative mechanisms).

What about absorption? In this case, we are considering the heating of the gas, and, thus it is possible to define a heating rate in a very similar way to Eq (1.13):

$$\dot{u}_H = n\Gamma(n, T, Z, J_\lambda) \tag{1.14}$$

Bottom panel of Figure 1.1 displays different heating functions. For $n_H = 1\,\mathrm{cm}^{-3}$, heating is several orders of magnitude below cooling, and therefore it has not gotten much attention. Main approaches in the literature consist in either turn cooling off at some threshold temperature (usually $10^4\,\mathrm{K}$), or to use the Koyama and Inutsuka (2002) constant value of $2 \cdot 10^{-26}\,\mathrm{erg/s}$ (also plotted in Figure 1.1). For the former recipe, this cutoff is motivated by the sharp jump that the cooling function has at $10^4\,\mathrm{K}$. On the other hand, Koyama and Inutsuka (2002) prescription is the result from the calculation of several processes of heating (not only radiative mechanisms) that take place in molecular clouds.

1.3.2 Shielded gas, and its relevance in the ISM

Let me consider this example: a massive star, emitting ionizing photons, surrounded by neutral gas. In that case, the closest neutral gas to the star will become ionized, and hence hotter, because it is exposed to the ionizing photons. The farther the gas is from the star, the lesser the number of ionizing photons that will reach that region. Beyond a certain distance from the star, called the Strömgren radius in textbooks, there are no more ionizing photons and the following gas will not be ionized.

In other words, the gas has become optically thick to ionizing radiation for distances higher than the Strömgen radius. Therefore, that gas away from the star is told to be self-shielded from its radiation, meaning that its heating mechanism is, in practice, disabled.

This example is critical to bear in mind, because it formally divides the ISM into two, since the radiation that can heat the gas will divide the medium into two phases: the unshielded gas that absorbes that radiation, which in turn becomes the warm ISM of Figure 1; and the gas deeply located within that gas, which is shielded from the heating radiation, generating the cold ISM.

1.4 The interstellar radiation field

The interstellar radiation field (ISRF) are all photons, created in a galaxy, that pervades the ISM. This is the result of all processes introduced and discussed throughout this chapter for all actors in a galaxy. Figure 1.2 shows the mean intensity spectra of the Milky Way Galaxy (MWG), separated by its main constituents:

1) Stars, from a radiative point of view, can be considered a Black-Body with (absorption, but no always) lines on it. The two bumps that they generate in Figure 1.2 correspond to the young stellar population, giving a major source of UV and ionizing photons, and to the old stellar population, responsible of the optical and near-IR part of the spectrum.

2) Dust absorbs and emits in the ISRF. To understand absorption, aside photoelectric effect, photons with similar wavelengths as the grain size heat dust. That heat is released as thermal emission as a Black-Body-like emission (for a detailed model, see Draine and Li, 2007), corresponding to a temperature of $\approx 20\,\mathrm{K}$ in the IR (Ferrière, 2001).

3) This explanation does not cover the peaks around 10 μm in the ISRF. In that range, the responsible are the vibrational bands of PAH. PAH also absorb UV photons that moves them into an excited state of the molecule. Then, it reemits photons as they perform line transitions in order to return to the PAH ground state.

4) Finally, we have the gas in the ISRF, which gives a significant contribution as emission lines. In the continuum (also called nebular) part of the ISRF, it only contributes to the absorption of the ionizing photons by generating the jump of three orders of magnitude in the ISRF mean intensity, according to Figure 1.2 at 91 nm.

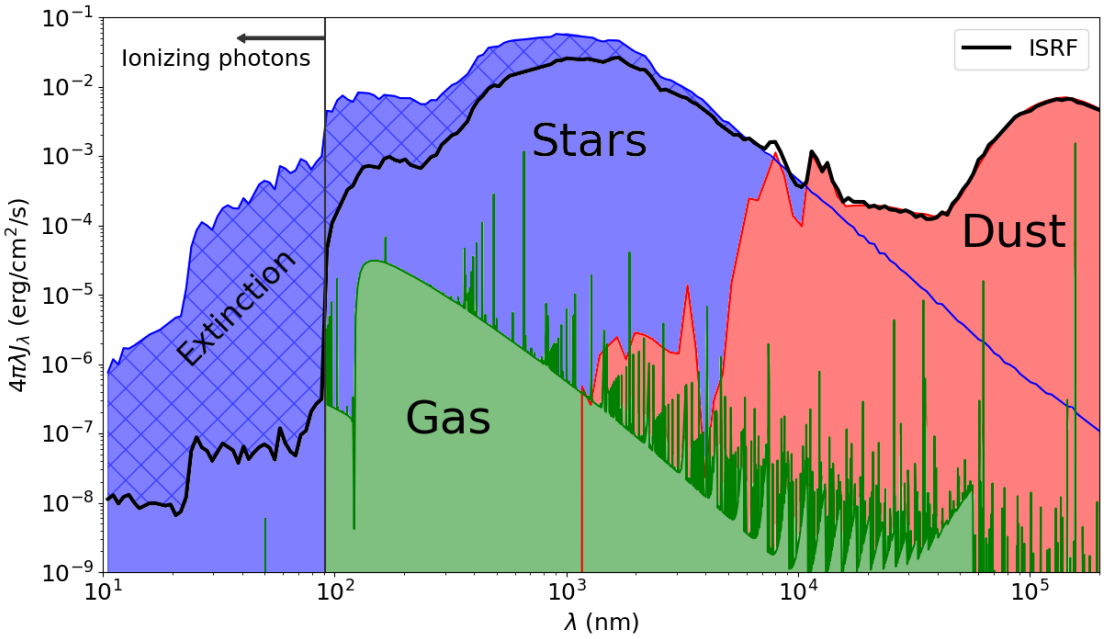

Figure 1.2: Scheme of the interstellar radiation field (ISRF, black line) of the Milky Way Galaxy (MWG) at the solar neighborhood. Hatched area represents the extinction by dust first and then gas (the threshold lies at $\lambda = 91\,\mathrm{nm}$). Emission of each component of the ISRF is plotted separately with different colors. Figure obtained from Chapter 4 results.

Chapter 2

Analytical Models of Supernova Remnants Turning Radiative

This chapter presents my own unpublished work.

2.1 Basics of supernova remnants

As commented in previously, a supernova remnant (SNR) is what remains after a SNe explosion. That is, it is the shock wave generated by the explosion and the ISM that is swept into the blast.

SNe lie into two categories regarding their progenitor: Core-Collapse (CC) SNe are produced when a young star dies due to gravitational collapse. The other kind is known as Type-Ia SNe. These are produced by a thermonuclear explosion of a white dwarf that exceeded a mass of $1.4\,\mathrm{M}_\odot$ (called the Chandrasekhar mass). Not all white dwarfs are fated to explode, and only those that have a companion may trigger a SN, either because the white dwarf has accreted mass from its stellar companion, or because it has merged with another white dwarf (for a review, see Maoz et al., 2014).

In terms of SNR modelling, there are analytical approaches, that I treat here, and the numerical route, which I leave it to the next chapter. Either way, both characterize a SNR in terms of just a few physical parameters:

1. **Shock radius** (R): distance between the (former, if Type-Ia) compact object and the shock discontinuity that the SN generates.

2. **Mach number** ($\mathcal{M}$): shock propagation velocity, compared to the ISM sound speed,

$$\mathcal{M} \equiv \sqrt{\frac{\rho_0 v_s^2}{\gamma P_0}} \tag{2.1}$$

   where $v_s = \frac{dR}{dt}$, and (ρ_0, P_0) denote the ISM density and pressure, respectively. The shock is strong when $\mathcal{M} \gg 1$ and weak if slightly above unity[1]. The end of any shock, and thus SNR, occurs when $\mathcal{M} = 1$.

3. **Logarithmic derivative** (η): defined as $\eta = \frac{d\ln(R)}{d\ln(t)}$, it is also referred to as 'deceleration parameter' or 'power-law exponent' in the literature. This characterisation of the shock propagation velocity is mainly used to compare with the first analytical solutions, of the form $R \propto t^\eta$ (see below).

4. **SNR energy** (E): total energy engulfed by the shock/remnant as a function of time. At the very beginning, it is equivalent to the initial $E_0 \sim 10^{51}$ erg injected by the initial explosion.

5. **SNR momentum** (p): In the last decade, the momentum injected by the SNR has become the most popular magnitude for two reasons. First, it is more suited for studying turbulence generated by the explosion and, second, it becomes constant: $p \sim 4 \cdot 10^5\,\mathrm{M}_\odot\,\mathrm{km/s}$, although it has a mild dependence with ISM density at the end of the SNR life.

2.1.1 Canonical SNR evolution

Most SNR in the solar vicinity follow a similar evolutionary path. From the initial explosion to the thermalization of the shock wave (i.e.: it is no longer a shock), SNR go into several phases with different physical processes taking a role. The simplest solutions apply several approximations in order to model each one of these phases:

[1] The threshold between the strong and weak shock regimes is $\mathcal{M} \approx 3$, but the reader should be aware that this limit is a blurred one.

1. The radius of the SNR evolves as a power law, $R \propto t^{\eta}$.
2. The external ambient pressure P_0 is negligible against the post-shock pressure P_1 (i.e. strong shock).
3. The solution is self-similar, implying that you can treat the internal structure of the SNR and the radial evolution (i.e. the shock radius) separately.

Before presenting any model, let me please review the main canonical phases of a SNR from very basic principles (For a more detailed derivation, see Ostriker and McKee, 1988; Bisnovatyi-Kogan and Silich, 1995).

2.1.1.1 Ejecta-dominated phase

After the initial explosion, the SNR starts an ejecta-dominated, or free-expansion, phase. Here, the evolution is dictated by the mass returned to the ISM by the SNe (between 1.4 and 10 $M_{\odot}$, depending on its origin).

To better understand this phase, I would like to invoke the analogy to the free expansion experiment, from the typical thermodynamics text book. In that analogy, you have two containers separated by a piston, one filled with gas and other empty. Then, the piston is suddenly removed and the gas expands into the empty container. In order to apply this to SNR, the filled and empty containers are the ejected gas mass from the progenitor and the ISM, respectively; while the action of removing the piston is the SNe explosion itself.

As an adiabatic phase, energy is conserved during the free expansion. From a dimensional analysis, it means that the quantities with units of energy are conserved. Thus, considering the product:

$$M(t)v_s^2(t) = constant, \tag{2.2}$$

where $M(t) \approx M_0$ is the ejected mass. From (2.2), the velocity must be constant, and, therefore, the only possibility is that:

$$R \propto t \quad ; \quad \eta = 1 \tag{2.3}$$

Obviously, the picture of a empty ISM does not last forever. First, the ISM gas will push the expansion back and produces a reverse shock that thermalizes the SNR interior. Then, the ejecta-dominated phase finishes when the swept-up mass by the SNR is similar to M_0:

$$M_{sw}(t) = \frac{4\pi}{3}\rho_0 R^3 \sim M_0, \tag{2.4}$$

2.1.1.2 Sedov-Taylor phase

Eventually, $M(t) \rightarrow M_{sw}(t)$, and so the SNR enters in the so-called Sedov-Taylor phase, although the name of 'adiabatic phase', in singular, is also used.

Energy is still conserved during this phase, and thus we can apply the same reasoning made in the Ejecta-Dominated phase. If we introduce Eq. (2.4) into Eq. (2.2) assuming that the ISM density, ρ_0, is constant, we find that the product:

$$R^3 v_s^2 = constant, \tag{2.5}$$

yielding:

$$R \propto t^{\frac{2}{5}} \quad ; \quad \eta = \frac{2}{5} \tag{2.6}$$

The exact solution derived by Sedov (1959) and Taylor (1950) gives:

$$R(t) = (\tfrac{\chi E_0}{\rho_0})^{\frac{1}{5}} t^{\frac{2}{5}} \tag{2.7}$$

$$v_s(t) = \tfrac{dR}{dt} = \tfrac{2}{5}(\tfrac{\chi E_0}{\rho_0})^{\frac{1}{5}} t^{-\frac{3}{5}}, \tag{2.8}$$

where $\chi \approx 2$ for $\gamma = \frac{5}{3}$, and $E_0 \sim 10^{51}$ erg is the initial SNR energy. This way, the product (2.5) yields:

$$R^3 v_s^2 = \frac{4\chi E_0}{25\rho_0} \tag{2.9}$$

The Sedov-Taylor phase ends when the gas radiative cooling becomes relevant. Before that, the gas is cooling adiabatically from the expansion and, when its temperature reaches $T \sim 10^5$ K, the cooling by lines becomes very efficient. This happens in the regions closer to the shock front, where the gas is more dense and has a lower temperature than in the interior.

2.1.1.3 Snowplough phases

When the cooling becomes relevant, the SNR develops a thin cold shell that pushes into the ISM like a snowplough. Moreover, the hot interior and the surrounding ISM are separated by this thin shell, that can be thought as a piston if we return into thermodynamic-textbook examples. Hence, this initial phase is also called Pressure-Driven Snowplough (PDS).

Now, the energy is no longer conserved, but we may instead consider the Newton's second law:

$$\frac{d}{dt}(Mv_s(t)) = 4\pi R^2(P_{hot} - P_0), \tag{2.10}$$

where the change of momentum is equal to the force made by the difference between hot interior pressure, P_{hot}, and ISM pressure, P_0. $P_{hot} \gg P_0$ in this phase and the gas interior expands adiabatically, giving the functional dependence:

$$P \propto V^{-\gamma} \propto R^{-3\gamma} \tag{2.11}$$

where γ is the adiabatic constant. Therefore, a solution of the form $R \propto t^{\eta}$ into Eq. (2.10) gives

$$\eta = \frac{2}{2+3\gamma} \tag{2.12}$$

For $\gamma = \frac{5}{3}$, proper of monoatomic gases, $\eta = \frac{2}{7}$.

After a certain time, the hot interior pressure will be equal to the ambient one, leaving a shell moving by its own inertia. At this point, the SNR enters in its last phase dubbed Momentum-Conserving snowplough (MCS). According to Eq. (2.10), the right-hand side is now equal to zero. In that case, a power-law solution yields

$$R \propto t^{\frac{1}{4}} \quad ; \quad \eta = \frac{1}{4} \tag{2.13}$$

This solution was originally derived by Oort (1951). For a more complex solution of these phases, I refer to Cioffi et al. (1988); Ostriker and McKee (1988) and Coughlin (2020).

2.1.2 Non-canonical evolution

However, this scheme changes when the ISM density takes extreme, albeit realistic, values:

On one hand, when the ISM density is very high, $\gtrsim 10^5\,\mathrm{cm}^{-3}$, proper of very cold mediums,the SNR skips the Sedov-Taylor phase entirely as Jiménez et al. (2019) found. In this case, radiative cooling becomes relevant at the ejecta-dominated phase, and this has an impact in both the leading and reverse shock that this SNR stage features.

On the other hand, at very low densities, $\lesssim 10^{-2}\,\mathrm{cm}^{-3}$, as found in the hot gas of elliptical galaxies (e.g.: Dorfi and Voelk, 1996; Brighenti and Mathews, 2005; Tang and Wang, 2005) or in the halo of the spiral ones (Hakobyan et al., 2017), the Sedov-Taylor SNR stage evolves into a weak-shock regime and then it merges with the ambient before turning radiative. This difference is critical, as it means that the SNR injects the full 10^{51} erg of the initial explosion into its surroundings instead of being radiated away. Solutions of this evolution involves hypergeometric functions, as found by Tang and Wang (2005) and Raga et al. (2012).

2.1.3 Characterizing the fate of a SNR

The evolutionary paths that a SNR can take may be different than the classical one if certain conditions, as a high ISM density, are met. Rather than using a canonical/non-canonical classification, it is more convenient to divide evolution into radiative, including classic and Jiménez et al. (2019) SNR, and non-radiative for low-density SNR.

2.1.3.1 Radiative (canonical) SNR

In the literature, it is usual to estimate the time when the SNR becomes radiative, denoted here as t_c. Following Franco et al. (1994) (see also Kim and Ostriker, 2015; Jiménez et al., 2019), if an infinitely small gas region is shocked by the SNR at a time t, then it cools at $t + t_\Lambda$. The time that minimizes the summation is just the time when the SNR becomes radiative:

$$\frac{\partial(t+t_\Lambda)}{\partial t}|_{t_c} = 0 \tag{2.14}$$

in this expression, t_Λ is related with the cooling function evaluated just after the shock radius (dubbed here with subindex 1):

$$t_\Lambda = \frac{u_1}{|\dot{u}_{C,1}|} = \frac{3P_1}{2n_1^2\Lambda(T_1)} \tag{2.15}$$

In that regard, equation (2.15) have a cooling function that can be approximated as:

$$\Lambda(T) \approx \Lambda_a (\frac{T}{T_a})^a, \tag{2.16}$$

where $\Lambda_a = 10^{-22}\,\mathrm{erg\,cm^3/s}$, $T_a = 10^5\,\mathrm{K}$ and $a = -0.9$.

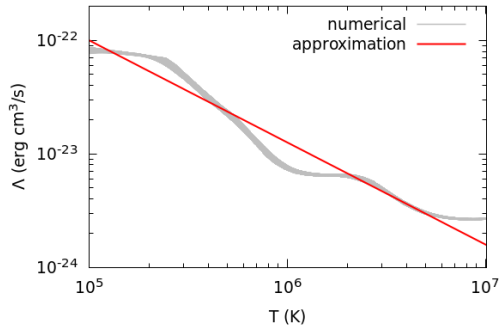

Figure 2.1: Power-law approximation proposed in (2.16) against the cooling function used in the numerical simulations at 2.3.4. Full numerical curve is shown in the lower-left plot from the upper panel of Figure 3.7, and instructions on how to reproduce it are in section 3.2.1.

In Figure 2.1 I show that this expression is a decent approximation between $T = 10^5$ to $10^7\,\mathrm{K}$, which is the range of temperatures where the gas is expected to cool from a hot to a warm phase.

We can make an estimate of t_c. First, I introduce (2.16) into (2.15), and assuming that temperature $T_1 = \frac{P_1}{n_1 k_B}$:

$$t_\Lambda = \frac{3(n_1 k_B T_a)^a}{2 n_1^2 \Lambda_a} P_1^{1-a}, \tag{2.17}$$

where P_1 and n_1 are the post-shock values of the ISM density and pressure for a strong shock:

$$n_1 = 4 n_0 \tag{2.18}$$

$$P_1 = \tfrac{3}{4}\rho_0 v_s^2, \tag{2.19}$$

t_c can be obtained by including (2.19) into (2.17), and introducing (2.8) to remove v_s in (2.19). As a result, a long expression is obtained, which, in the end, shows that $t_\Lambda \propto t^{\frac{6}{5}(1-a)}$. It is now possible to solve (2.14), to obtain an estimate of t_c. For the case of a mean atomic weight, $\mu = \frac{\rho}{m_H n}$, equal to $\frac{3}{5}$, proper to hot ionized gas, the following expression is obtained:

$$t_c^{\frac{1}{5}(11-6a)} = \frac{81(1-a) m_H}{1600 n_0 \Lambda_a} (\frac{9 m_H}{80 k_B T_a})^{-a} (\frac{16 \chi E_0}{375 n_0})^{\frac{2}{5}(1-a)} \tag{2.20}$$

To visualize t_c, left panel of Figure 2.2 shows equation (2.20) as a blue line. From this graph we can compare the current lifespan of the SNR (i.e.: t) against t_c. Given an ambient density, any SNR above the line is already in a radiative phase, whereas anything below it is still in the Ejecta-dominated, Sedov-Taylor or low-density phases.

2.1.3.2 Non-radiative SNR

As mentioned in 2.1.2, a SNR evolving in a low-density medium will reach the weak-shock regime before t_c. Therefore, I want to suggest to use the ambient energy swept up by the SNR, rather than t_c, to characterise

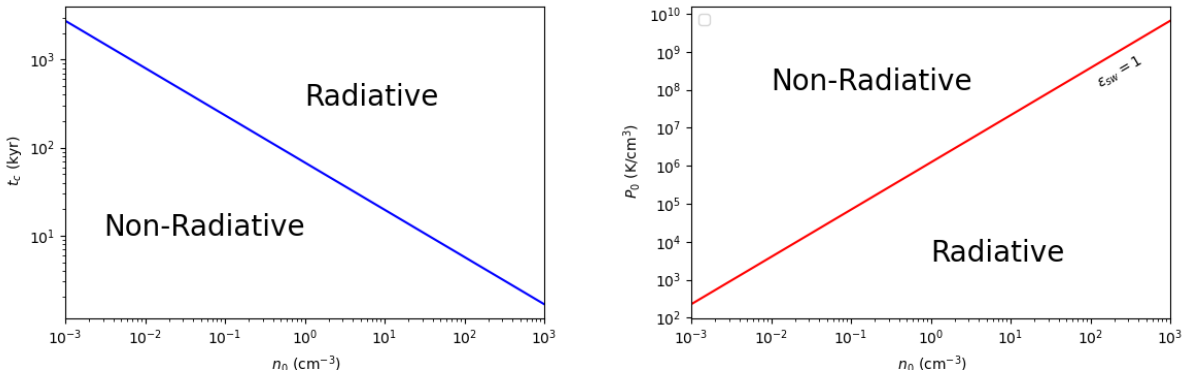

Figure 2.2: Left panel: time in which the SNR becomes radiative, t_c, in terms of ambient number density, n_0. Any SNR whose lifespan is higher than t_c (blue line) has become radiative. Right panel: map of environment conditions $\{n_0, P_0\}$, where the red line is the frontier between radiative and non-radiative SNR (i.e.: $\varepsilon_{sw} = 1$). Any SNR whose surroundings are above the line dies before turning radiative.

the lifetime of the Sedov-Taylor phase. Assuming that $\gamma = \frac{5}{3}$ for the rest of this chapter, the swept-up energy is given by:

$$E_{sw} = 2\pi P_0 R^3 \tag{2.21}$$

Replacing P_0 with Mach number definition (2.1) and, then, the product (2.9), this gives

$$E_{sw} = \frac{6\pi\rho_0}{5\mathcal{M}^2} R^3 v_s^2 = \frac{24\pi\chi}{125} \frac{E_0}{\mathcal{M}^2} \approx 1.2 \frac{E_0}{\mathcal{M}^2}, \tag{2.22}$$

which vanishes if $\mathcal{M} \to \infty$. In other words, we can say that the low-density regime starts when $E_{sw} \sim E_0$, somewhat equivalent to the weak-shock condition. This establishes an analogy with the transition from the Ejecta-dominated to Sedov-Taylor phase, which is the same condition but with mass (i.e.: $M_{sw} \sim M_0$, being M_0 the mass ejected by the SN).

In order to wrap together the radiative and non-radiative scenarios, I define a dimensionless energy fraction:

$$\varepsilon_{sw} = \frac{2\pi P_0}{E_0} \left(\frac{\chi E_0}{\rho_0}\right)^{\frac{3}{5}} t_c^{\frac{6}{5}} \tag{2.23}$$

With this parameter, $E_{sw} = \varepsilon_{sw} E_0 (\frac{t}{t_c})^{6/5}$ if a Sedov-Taylor radius (2.7) is assumed. If the SNR dies at $t > t_c$, then $\varepsilon_{sw} \ll 1$ and the evolutionary path will be the canonical one. On the other hand, if $\varepsilon_{sw} \gtrsim 1$ the ambient cannot be neglected and the SNR evolution will resemble the results of Tang and Wang (2005).

Right panel of Figure 2.2 shows the frontier between radiative and non-radiative SNR evolution, set at $\varepsilon_{sw} = 1$. Given an environment (n_0, P_0), this plot tells us *how* the SNR is going to die, in contrast with the other panel, which is about *what phase* is the SNR undergoing at that moment.

2.2 Modelling SNR temporal evolution

To find an equation to describe the time evolution of SNR, I suggest using energy balance. The initial SNR energy E_0 changes over time in two directions: A SNR can gain energy by sweeping the ISM as it advances, and it can lose energy radiatively with a term involving the total luminosity of the remnant. Therefore, the SNR energy balance should be:

$$E(t) = E_0 + E_{sw}(t) - \int_0^t L(t)\, dt \tag{2.24}$$

To solve (2.24), I propose this ansatz:

$$R(\hat{t}) = \left(\frac{\chi E_0}{\rho_0}\right)^{\frac{1}{5}} t_c^{\frac{2}{5}} \left[\int_0^{\hat{t}} \mathcal{I}(\hat{t})\, d\hat{t}\right]^{\frac{2}{5}} \tag{2.25}$$

$$v_s(\hat{t}) = \frac{dR}{dt} = \frac{2}{5}\left(\frac{\chi E_0}{\rho_0}\right)^{\frac{1}{5}} t_c^{-\frac{3}{5}}\, \mathcal{I}(\hat{t}) \left[\int_0^{\hat{t}} \mathcal{I}(\hat{t})\, d\hat{t}\right]^{-\frac{3}{5}}, \tag{2.26}$$

in terms of a dimensionless parameter $\hat{t} = \frac{t}{t_c}$ that takes into account the time in which the SNR becomes radiative, t_c. On the other hand, $\mathcal{I}$ is one of the main quantities of the suggested model. It has three useful properties:

1. If $\mathcal{I}(\hat{t}) = 1$ you recover Sedov-Taylor solution (2.7). From this point of view, $\mathcal{I}$ measures how the result drifts from its phase.
2. It takes advantage of $R^3 v_s^2 =$ constant and transforms it into $R^3 v_s^2 \propto \mathcal{I}^2$.
3. As consequence of the above statements, $E(\hat{t}) = E_0 \mathcal{I}^2$. Taking into account that Sedov-Taylor solution conserves E_0 (for a more solid proof, see B.2), it is evident that $\mathcal{I}$ has a physical meaning related to the fraction of energy that the SNR has at time $\hat{t}$.

Next step is to write (2.24) in terms of $\mathcal{I}$ and solve the I-function instead.

First, the swept-up energy comes from writing (2.21) in terms of (2.25) and (2.23)

$$E_{sw} = \varepsilon_{sw} E_0 \left[\int_0^{\hat{t}} \mathcal{I} d\hat{t}'\right]^{\frac{6}{5}} \tag{2.27}$$

The above expression allows to define another function, in terms of the integral of $\mathcal{I}$:

$$\mathcal{T} \equiv \int_0^{\hat{t}} \mathcal{I}\, d\hat{t}' \tag{2.28}$$

or $\dot{\mathcal{T}} = \frac{d\mathcal{T}}{d\hat{t}} = \mathcal{I}$. $\mathcal{T}$ is a dimensionless time that remaps time from the Sedov-Taylor solution (recovered when $\mathcal{T} = \hat{t}$).

Finally, the luminosity term of (2.24) is the more complex one, as it drastically changes over the course of the SNR evolution. For now, allow me to rewrite L in terms of $\{\hat{t}, \mathcal{I}, \mathcal{T}\}$ as:

$$L = f(\hat{t})\mathcal{I}^n \mathcal{T}^m E_0, \tag{2.29}$$

and we will see below particular solutions of different SNR phases that adapt into expression (2.29).

This way, we can now express (2.24) in terms of either $\mathcal{I}$ or $\mathcal{T}$:

$$\mathcal{I}^2(\hat{t}) = 1 + \epsilon_{sw}\mathcal{T}^{\frac{6}{5}} - \int_0^{\hat{t}} f(\hat{t})\mathcal{I}^n\mathcal{T}^m \, d\hat{t}' \tag{2.30}$$

$$\ddot{\mathcal{T}} = \tfrac{3}{5}\varepsilon_{sw}\mathcal{T}^{\frac{1}{5}} - \tfrac{1}{2}f(\hat{t})\dot{\mathcal{T}}^{n-1}\mathcal{T}^m \tag{2.31}$$

where $\mathcal{I}(\hat{t} = 0) = 1$ is used as initial condition.

2.3 Analytical solutions from energy balance

Instead of solving equations (2.30) and (2.31) numerically with your favourite differential equation solver, I prefer to show you the power of this approach by deriving analytical solutions, covering different phases described in 2.1.1 and 2.1.2.

2.3.1 Low-density regime

Let me consider first the case in which the swept-up ambient energy is important, and you can neglect radiative losses. From (2.30) and using $\dot{\mathcal{T}} = \mathcal{I}$

$$\dot{\mathcal{T}}^2 = 1 + \epsilon_{sw}\mathcal{T}^{\frac{6}{5}} \tag{2.32}$$

However, this equation brings some difficulties. You can found a analytical solution for $\hat{t}$ as function of $\mathcal{T}$

$$\hat{t}(\mathcal{T}) = \int_0^{\mathcal{T}} \frac{d\mathcal{T}}{\sqrt{1 + \epsilon_{sw}\mathcal{T}^{6/5}}} = \mathcal{T}\ {}_2\mathbb{F}_1(\frac{1}{2}, \frac{5}{6}; \frac{11}{6}; -\epsilon_{sw}\mathcal{T}^{\frac{6}{5}}) \tag{2.33}$$

where ${}_2\mathbb{F}_1$ is the hypergeometric function. These type of functions also appear in the radius derived by Tang and Wang (2005) and Raga et al. (2012), but it also tells that reverting $\mathcal{T}(\hat{t})$ is not an easy task.

From here, you can still obtain a relation for $\mathcal{I}(\mathcal{T})$ deriving (2.33) by $\hat{t}$:

$$\mathcal{I}(\mathcal{T}) = [{}_2\mathbb{F}_1(\frac{1}{2}, \frac{5}{6}; \frac{11}{6}; -\epsilon_{sw}\mathcal{T}^{\frac{6}{5}}) - \frac{3\epsilon_{sw}}{11}\mathcal{T}^{\frac{6}{5}}\ {}_2\mathbb{F}_1(\frac{3}{2}, \frac{11}{6}; \frac{17}{6}; -\epsilon_{sw}\mathcal{T}^{\frac{6}{5}})]^{-1} \tag{2.34}$$

In addition to the exact analytical solution involving hypergeometric functions, let me discuss both $\hat{t} \to 0$ and $\hat{t} \to \infty$ limits. For the former, you may ignore the ambient term in (2.32), yielding that $\dot{\mathcal{T}} = \mathcal{I} \approx 1$, the Sedov-Taylor solution by construction. For the latter, $\hat{t} \to \infty$ means that the swept-up energy is much higher than the ejected energy by the SNe, and thus (2.32) can be approximated to $\dot{\mathcal{T}}^2 = \mathcal{I}^2 \approx \varepsilon_{sw}\mathcal{T}^{6/5}$. This differential equation gives that $\mathcal{T} \propto \hat{t}^{5/2}$ (or $\mathcal{I} \propto \hat{t}^{3/5}$). If introduced into (2.26), we obtain that velocity is constant, as expected for a SNR that asymptotically becomes a sound wave.

2.3.2 Evolution to a radiative phase

For radiative SNR evolution, you can obtain an analytical solution that is more sophisticated that Sedov-Taylor one for $\hat{t} < 1$. Although for this phase the ambient can be safely ignored, now you have to compute the luminosity with the help of the cooling function of the gas inside the SNR:

$$L = \int_V n^2 \Lambda(T) \, dV \tag{2.35}$$

This forces us to assume an internal structure. Specifically, a profile for number density and temperature. Reaching these equations needs a very long detour, and so I prefer to leave the whole derivation into appendix B.2. Instead, I am going straight to the point giving you the approximate final solution of appendix B.2 for $\mu = \frac{3}{5}$:

$$n \approx n_1 \hat{r}^9 \tag{2.36}$$

$$T \approx \tfrac{P_1}{5n_1 k_B}(2\hat{r}^{-9} + 3\hat{r}^{13}), \tag{2.37}$$

where $\hat{r} = \frac{r}{R}$ is a dimensionless radius, while n_1 and P_1 are in (2.18) and (2.19)

Now we can integrate (2.35) approximately[2] to obtain:

$$L \approx \frac{64\pi}{90\cdot 5^a} n_0^2 \Lambda_a \left(\frac{P_1}{n_1 k_B T_a}\right)^a R^3 \tag{2.39}$$

From here, you can use (2.15) into (2.39) to have:

$$L = \frac{\pi}{4\cdot 5^{a+1}} \frac{\rho_0}{t_\Lambda} R^3 v_s^2 = \frac{\pi\chi}{5^{a+3}} \frac{E_0}{t_\Lambda(\hat{t})} \mathcal{I}^2, \tag{2.40}$$

and finally an expression for luminosity in terms of (2.29) is given:

$$L = \frac{6(1-a)\pi\chi}{5^{4+a}} \hat{t}^{\frac{6}{5}(1-a)} \mathcal{I}^2 E_0 = f_c \hat{t}^b \mathcal{I}^2 E_0, \tag{2.41}$$

where it is defined $f_c = \frac{6(1-a)\pi\chi}{5^{4+a}} \approx 0.488$ and $b = \frac{6}{5}(1-a) = 2.28$ (provided that $a = -0.9$) to clean the long expressions a bit. Equation (2.31) can be solved analytically in terms of $\mathcal{I} = \dot{\mathcal{T}}$ with $\varepsilon_{sw} = 0$:

$$2\dot{\mathcal{I}} = -f_c \hat{t}^b \mathcal{I}, \tag{2.42}$$

whose solution is:

$$\mathcal{I}(\hat{t}) = e^{\frac{-f_c}{2(b+1)}\hat{t}^{b+1}} \tag{2.43}$$

One property of this solution is that we can compute the energy fraction that remains inside the SNR at $\hat{t} = 1$:

$$\mathcal{I}(1) = \varepsilon_q = e^{\frac{-f_c}{b+1}} \approx 0.862 \tag{2.44}$$

That is, a roughly $\sim 15\%$ of E_0 is lost due to radiation before any proper radiative snowplough phase begins.

To obtain $\mathcal{T}$, it is possible to integrate (2.43) in terms of the incomplete gamma function. However, it is more illustrative to do a Taylor series of (2.43) at $\hat{t} = 0$ to get an approximation of $\mathcal{T}$:

$$\mathcal{I} \approx 1 - \frac{f_c}{2(b+1)}\hat{t}^{b+1} + \frac{f_c^2}{8(b+1)}\hat{t}^{2(b+1)} \tag{2.45}$$

$$\mathcal{T} \approx \hat{t}\left(1 - \frac{f_c}{2(b+1)}\frac{\hat{t}^{b+1}}{b+2} + \frac{f_c^2}{8(b+1)^2}\frac{\hat{t}^{2(b+1)}}{2b+3}\right) \tag{2.46}$$

2.3.3 Pressure-Driven Snowplough

In the canonical radiative scenario, it is often assumed that, once cooling becomes efficient ($\hat{t} > 1$), all the swept-up energy is immediately radiated away, right behind the shock front (fully radiative shock approximation). From Cioffi et al. (1988), the luminosity in that case is:

$$L \approx 2\pi\rho_0 R^2 v_s^3 = \frac{16\pi\chi E_0}{125 t_c} \mathcal{I}^3 \mathcal{T}^{-1} \tag{2.47}$$

Therefore, $f(\hat{t}) = f_r = \frac{16\pi\chi}{125} \approx 0.8$, $n = 3$ and $m = -1$. Neglecting the term associated to $\epsilon_{sw} \ll 1$, equation (2.31) becomes

$$2\mathcal{T}\ddot{\mathcal{T}} + f_r \dot{\mathcal{T}}^2 \approx 0, \tag{2.48}$$

which has the analytical solution

$$\mathcal{T}(\hat{t}) = c_2[c_1 + (2+f_r)\hat{t}]^{\frac{2}{2+f_r}}, \tag{2.49}$$

being $\{c_1, c_2\}$ the integration constants, whose value is set by the conditions at $\hat{t} = 1$ derived above.

The approximate expression $\mathcal{T}(\hat{t})$ that I obtain, and hence the shock radius ($R \propto \mathcal{T}^{2/5}$), is an offset power-law. This result is reminiscent of the ansatz given by Cioffi et al. (1988) for this specific SNR phase, but here I provide an analytical derivation from physical grounds instead of an ansatz.

Another interesting property of this solution appears when you compute the logarithmic derivative (i.e. the power-law exponent):

$$\eta \equiv \frac{d\ln(R)}{d\ln(t)} = \frac{2\hat{t}}{5}\frac{\mathcal{I}}{\mathcal{T}} \tag{2.50}$$

[2] The main issue with the integral is that you end with

$$\int_0^1 \hat{r}^{20}(2\hat{r}^{-9} + 3\hat{r}^{13})^a \, d\hat{r} = \frac{2^a \; {}_2\mathbb{F}_1(-a, -\frac{3}{22}(3a-7); \frac{1}{22}(43-9a); -\frac{3}{2})}{21-9a} \tag{2.38}$$

We do not want that hypergeometric function to appear, and therefore I suggest to compute the integral numerically. For $a = -0.9$, this yields approximately $\frac{1}{90}$.

From here, you can compute $\mathcal{I}$ and η of (2.49):

$$\mathcal{I}(\hat{t}) = 2c_2[c_1 + (2+f_r)\hat{t}]^{\frac{-f_r}{2+f_r}} \tag{2.51}$$

$$\eta(\hat{t}) = \tfrac{4}{5}[\tfrac{c_1}{\hat{t}} + (2+f_r)]^{-1} \tag{2.52}$$

which, in the limit of $\hat{t} \to \infty$, η becomes:

$$\lim_{\hat{t}\to\infty} \eta = \frac{4}{5(2+f_r)} \approx \frac{2}{7} \tag{2.53}$$

meaning that this solution converges to $t^{2/7}$, consistent with the classical PDS power-law solution derived in 2.1.1.3 from Newton's second law.

2.3.4 Performance against numerical simulations

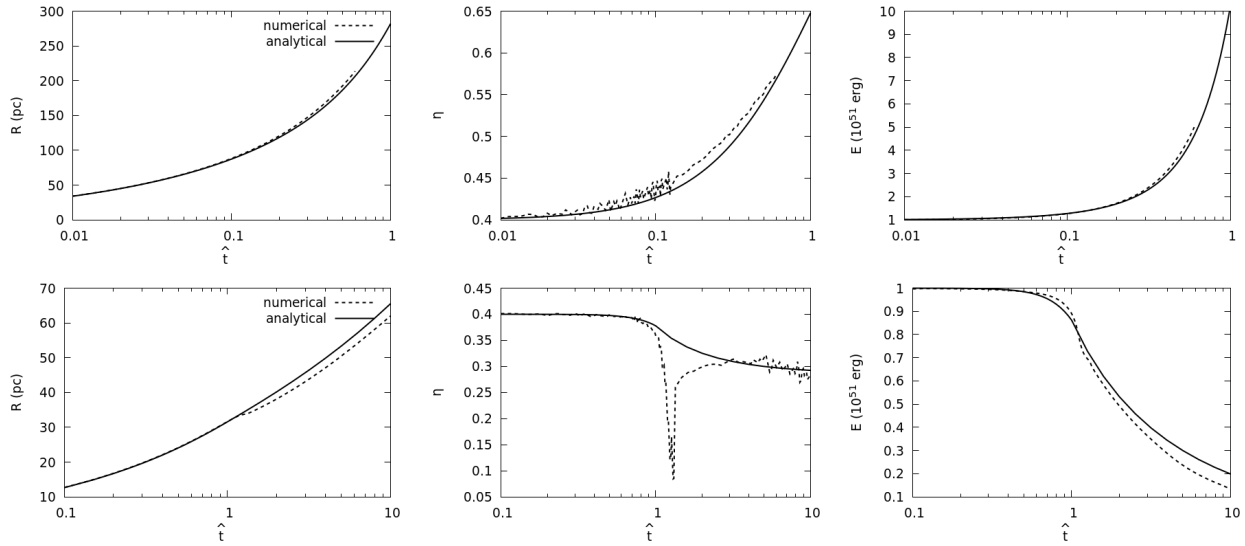

Figure 2.3: Predicted radius, its logarithm derivative η and total energy (solid line) against a numerical simulation (dashed line) of a SNR with $E_0 = 10^{51}$ erg and $n_0 = 10^{-2}\,\mathrm{cm}^{-3}$ (top row) and $n_0 = 1\,\mathrm{cm}^{-3}$ (bottom row).

In order to test the analytical solutions derived above, I run two numerical simulations with an ISM pressure $\frac{P_0}{k_B} = 16205\,\mathrm{K/cm}^3$ and explosion energy of $E_0 = 10^{51}$ erg as common initial conditions. To cover the three different regimes considered in this section, the top row of Figure 2.3 the results obtained for an initial number density $n_0 = 10^{-2}$ cm^{-3}, yielding $\varepsilon_{sw} \approx 4.1$, so the blastwave dies before turning radiative (section 2.3.1). The bottom row corresponds to $n_0 = 1\,\mathrm{cm}^{-3}$, where $\varepsilon_{sw} \approx 0.01$, and thus is representative of the solution discussed in 2.3.2 and 2.3.2 for $\hat{t} < 1$ and $\hat{t} > 1$, respectively, where the ambient swept-up energy is negligible, and the SNR will become radiative at $t_c \approx 68\,kyr$. In both cases, Figure 3.9 displays the shock radius, R; its logarithmic derivative, η; and the total energy inside the SNR, E.

First, let me consider the non-radiative SNR of Figure 2.3 top row briefly. There, the agreement between analytical and numerical values is excellent for all magnitudes, albeit numerical simulations appear truncated, as I do not follow numerical shocks below $\mathcal{M} < 1.3$ to avoid detecting spurious features not related with the SNR shock front (see 3.1.3 for details).

The SNR with $n_0 = 1\ cm^{-3}$ is a test of both a Sedov-Taylor phase turning radiative 2.3.2 and the PDS solution 2.3.3. Before the transition, both R and η fit the numerical results. Total energy is also consistent, albeit the numerical value of ε_q is a bit higher than the predicted 0.86, by about 10%. At $\hat{t} = 1$, the sharp transition in η is not well followed, and this slightly affects the shock radius and total energy. Nevertheless, setting the integration constants $\{c_1, c_2\}$ of (2.49) with the estimated values of $\mathcal{I}$ and η at $\hat{t} = 1$ yields differences that remain of the order $\sim 10\%$, and both the predicted and the numerical values of the logarithmic slope η slowly converge towards $\eta \to \frac{2}{7}$ at late times.

In any case, the method proposed to derive analytical solutions can give more sophisticated approximations than found in the literature. The accuracy of the solution heavily relies on the luminosity of the SNR. To illustrate this, I show in Figure 2.4 the analytical solution and the numerical result of SNR luminosity of the simulation with $E_0 = 10^{51}$ erg and $n_0 = 1\,\mathrm{cm}^{-3}$. Before and after $\hat{t} = 1$, the power-law fit I used for both regimes is consistent with the numerical values. At the peak of L, these two approximations fail to generate

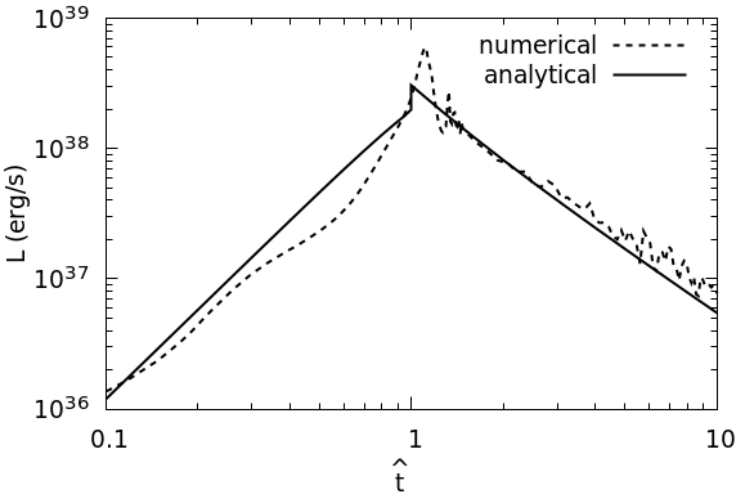

Figure 2.4: SNR luminosity from the simulation with $E_0 = 10^{51}\,\mathrm{erg}$ and $n_0 = 1\,\mathrm{cm}^{-3}$.

the overluminosity, suggesting that another ansatz, for times closer to $\hat{t} = 1$, would be needed to recreate the full η curve. Unfortunately, SNR luminosity is usually ignored and works that provide it as output (e.g. Franco et al., 1994; Thornton et al., 1998; Jiménez et al., 2019) are far less frequent than those that discuss the energy and momentum input to the ISM.

To finish this chapter, I would like to discuss the features that this model offers compared with the modern semi-analytical models of Haid et al. (2016) and Jiménez et al. (2019). On one hand, these models have a better treatment for SNR evolution at $\hat{t} = 1$ and can handle less idealized environments. In the case of Jiménez et al. (2019) model, it covers all phases of the canonical SNR evolution of 2.1.1. On the other hand, my model integrates the low-density SNR evolution with the canonical, radiative scenario. Moreover, it allows some versatility because you can solve (2.31) numerically in a semi-analytical fashion, and you can derive analytical solutions relevant to the SNR evolution as well.

Chapter 3

Impact of an External Radiation Field on Numerical Supernova Remnants

This chapter is based on the publication:
"Impact of the ERF on the structure and evolution of SNRs"
by M. Romero, Y. Ascasibar, J. Palouš, R. Wünsch, and M. Mollá
Published in MNRAS 505(4), pages 5301-5310 (2021)
Sections 3.1 and 3.3 are my own unpublished work

3.1 Eulerian fluid dynamics for supernova remnants

As an alternative to the previous chapter, it is possible to solve SNR with a numerical technique, following the equations of fluid mechanics. In astrophysics, most gases have low enough densities to ignore internal friction between particles, and also viscosity effects can be also ignored for most problems, such as SNR. Hence, the main equations to solve gas dynamics are the Euler equations:

$$\frac{\partial \rho}{\partial t} + \vec{\nabla} \cdot (\rho \vec{v}) = 0 \tag{3.1}$$

$$\frac{\partial}{\partial t}(\rho \vec{v}) + \vec{\nabla}(\rho \vec{v}^2 + P) = 0 \tag{3.2}$$

$$\frac{\partial \epsilon}{\partial t} + \vec{\nabla} \cdot [\vec{v}(\epsilon + P)] = 0 \tag{3.3}$$

These equations represent the conservation of mass, momentum and energy in terms of their densities $\{\rho, \rho\vec{v}, \epsilon\}$.

To close these equations, the gas pressure P needs to be defined. For the same reasons as the Euler equations are used, we can consider the thermodynamics of an ideal gas, giving a relation for P:

$$P = (\gamma - 1)(\epsilon - \frac{1}{2}\rho v^2), \tag{3.4}$$

The value of γ can be safely set to $\frac{5}{3}$, the value obtained for mono-atomic gases. Furthermore, for the H_2 molecule, the most common in the ISM, $\gamma = \frac{5}{3}$ still holds, because the H_2 appears at very low temperatures ($\sim$ 10 K) when its rotational states, which would give $\gamma = \frac{7}{5}$ at higher temperatures, are suppressed due to quantum effects.

There are two strategies to solve Eqs. (3.1)-(3.3):

1. On one hand, Smoothed particle hydrodynamics (SPH) algorithms consist in discretizing the fluid into particles that carry the relevant quantities. This method is also called *Lagrangian*, as these algorithms follow the path of all particles. This approach effectively transforms the problem into a N-body one, with its particular force calculation.

2. On the other hand, the other approach is dubbed *Eulerian*, which is the method followed here. In this case, the space is discretized into a mesh, where each quantity is computed at each point.

In this chapter, I present a code I wrote from scratch. It is an Eulerian finite-volume 1D hydrodynamical code with Adaptive Mesh Refinement (AMR). This code solves the Euler equations of mass, energy and momentum in 1D, written in a generic way as:

$$\frac{\partial \rho}{\partial t} + \frac{1}{r^q}\frac{\partial}{\partial r}(r^q \rho v) = 0 \tag{3.5}$$

$$\frac{\partial \epsilon}{\partial t} + \frac{1}{r^q}\frac{\partial}{\partial r}[r^q v(P + \epsilon)] = \dot{u}_H - \dot{u}_C \tag{3.6}$$

$$\frac{\partial}{\partial t}(\rho v) + \frac{1}{r^q}\frac{\partial}{\partial r}[r^q(\rho v^2 + P)] = 0 \tag{3.7}$$

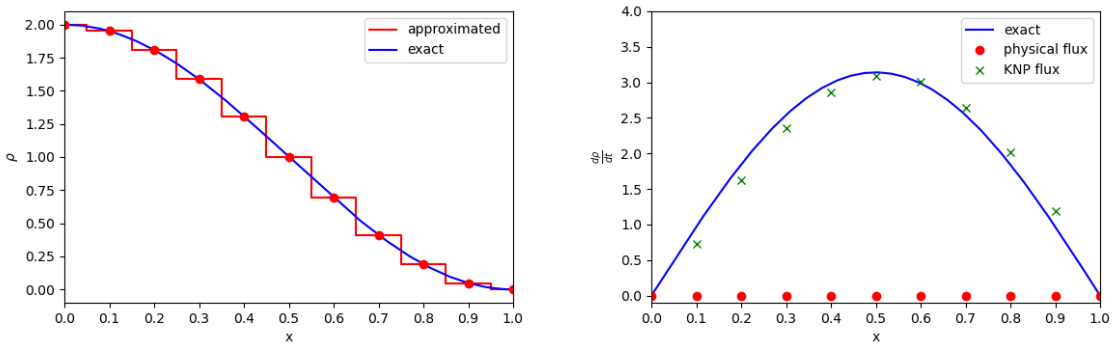

Figure 3.1: In Cartesian coordinates (i.e.:$q = 0$), left panel shows mass density ($\rho = \cos(\pi x) + 1$, blue line), in favourite units, approximated with a fluid Euler scheme (red line). Right panel displays the time derivative of ρ (blue line) against the formula (3.11) (red points) and the corrected flux formula used in this code (green crosses, see 3.1.1.1). For flux computation, velocity is 1 and sound speed is 0.5 for all x.

where $q = \{0, 1, 2\}$ for Cartesian, cylindrical and spherical coordinates, respectively; and $\dot{u}_C$ and $\dot{u}_H$ denotes the energy density change due to cooling and heating, also respectively.

Solving Euler equations are not straightforward. To better understand this, consider this generalization into one differential equation

$$\frac{\partial \mathbf{y}}{\partial t} + \frac{1}{r^q}\frac{\partial}{\partial r}(r^q \mathbf{f}) = \mathcal{U}, \tag{3.8}$$

where $\mathbf{y} = (\rho, \epsilon, \rho v)$ are the quantities of the Euler equations (3.5)-(3.7) that are referred to the center of the cell, $\mathbf{f}$ denotes the fluxes of $\mathbf{y}$:

$$\mathbf{f} = \begin{pmatrix} \rho v \\ (P + \epsilon)v \\ \rho v^2 + P \end{pmatrix} \tag{3.9}$$

and $\mathcal{U} = (0, \dot{u}_H - \dot{u}_C, 0)$ includes the source terms. Equation (3.8) can be integrated over a volume ΔV where $\{\mathbf{y}, \mathcal{U}\}$ can be approximated as constant, which should be fulfilled without much effort if the space is discretized enough.

The integral of (3.8) between the left $(-)$ and right $(+)$ borders of the cell yields

$$\frac{d\mathbf{y}}{dt} \approx -\frac{1}{\Delta V}\int_{(-)}^{(+)} \frac{1}{r^q}\frac{\partial}{\partial r}(r^q \mathbf{f}) dV + \mathcal{U} \tag{3.10}$$

For Cartesian, cylindrical or spherical coordinates, the integral of fluxes can be converted (see the detailed derivation in Appendix C) in:

$$\frac{d\mathbf{y}}{dt} = -(q+1)\frac{r^q_{(+)}\mathbf{f}_{(+)} - r^q_{(-)}\mathbf{f}_{(-)}}{r^{q+1}_{(+)} - r^{q+1}_{(-)}} + \mathcal{G} + \mathcal{U} \tag{3.11}$$

where $r_{(\pm)}$ is the location of the right and left interface of the cell $\mathbf{y}$. $\mathcal{G}$ is a term that considers if the coordinate system is Cartesian, cylindrical or spherical. This term is zero for all terms except for the momentum density outside Cartesian coordinates, which gives:

$$\mathcal{G}^{(\rho v)} = (q+1)\frac{r^q_{(+)}P_{(+)} - r^q_{(-)}P_{(-)}}{r^{q+1}_{(+)} - r^{q+1}_{(-)}} - \frac{P_{(+)} - P_{(-)}}{r_{(+)} - r_{(+)}} \tag{3.12}$$

Now that we have an expression for the time derivative of $\mathbf{y}$, nothing stop us to use our favourite ordinary differential equation (ODE) solver to advance to next timestep, say, the simplest one:

$$\mathbf{y}(t + \Delta t) = \mathbf{y}(t) + \Delta t \frac{d\mathbf{y}}{dt} \tag{3.13}$$

There is one problem though: this does not work. To illustrate this, consider the example of Figure 3.1 in Cartesian coordinates ($q = 0$). In favourite units, $\mathbf{y} = \rho = \cos(\pi x) + 1$, $v = 1$ and the sound speed, $c_s = 0.5$. Under these conditions, ρ, and so its flux $f = \rho v$, are constants within each cell, and thus (3.11) gives 0 as a result per cell, which is wrong.

Above paragraphs were written to highlight the basic procedure and difficulties that you encounter with an Eulerian code, adapted to the algorithms I present you at next section. To avoid the issue that arises with the derivatives in the example of Figure 3.1, one solution relies on redefining the fluxes (see 3.1.1.1), denoted here as $\mathbf{F}$, to make the change $\mathbf{f} \rightarrow \mathbf{F}$ so (3.11) gives valid results to apply our favourite ODE solver (3.13)[1].

3.1.1 Code structure

I took as basis the methods and equations shown in Doumler and Knebe (2010, AMIGA), but also from Ziegler (2004, 2005) for some details as well. There are also some differences that I want to recall: First, the architecture is written in `C`, whereas this code has been programmed with `C++`. This will allow me to take advantage of the object-oriented programming paradigm. Second, AMIGA is meant to be used in cosmological simulations, which differs significantly from the scope of this chapter (and thesis), which is focused on SNR, that is, a much smaller scale. Therefore, some physical processes implemented in AMIGA are not needed for SNR, such as 3D and dark matter; while other, such as radiative cooling and heating, must be included into the code, and adapt other ones implemented in Doumler and Knebe (2010)

The code developed for this study has a class named `cell` as its main units. Per each timestep, the simulation domain is divided in a grid of cells. Each one contains:

1. All physical quantities relevant to the hydrodynamic equations (3.5)-(3.7), as well as entropy S. These values are evaluated in the center of the cell.

2. All chemical and thermodynamical magnitudes needed to perform the cooling. These are the temperature, T, cooling time, t_Λ, and the mean atomic weight, μ. Likewise, they are the values in the center of the cell.

3. All methods needed to update these quantities for subsequent timesteps.

4. Two pointers that tell to the cell who their neighbors are.

For simplicity, the actual cell I am talking is going to be labelled as *current* cell. *Left* and *right* cells denotes the previous and following cells. Spatially, left cells have lower values of the position r compared with the current one and vice-versa for right cells (i.e.: $r_{i-1} < r_i < r_{i+1}$, where i denotes the current cell).

Figure 3.2 shows the flowchart followed by my code. First, it computes the corrected fluxes $\mathbf{F}$ to compute the time derivative (3.11). Then, I advance in time with a more complex ODE solver than the example (3.13), requiring two evaluations of $\mathbf{y}$, and so you need to repeat the flux and derivative computation twice. At the end of the second evaluation, I also remap the number of cells to have adaptive resolution. Next subsections break down each process, and I leave the initial conditions for each test and scientific problem.

3.1.1.1 Flux computation

The initial step is to evaluate the fluxes of each physical quantity. This evaluation has to be done at both interfaces (+ for right, − for left) of the current cell, as demanded with the physical fluxes $\mathbf{f}$ of (3.11). In most cases, I consider that $\mathbf{y}_i$ does not change across the cell, as shown in the left panel of Figure 3.1. However, when the specific quantity of y_i is a maximum or a minimum compared with its closest neighbors, there is a risk to generate an spurious oscillation. To remedy that, I compute particular values of $y^{(+)}$ and $y^{(-)}$, following van Leer (1977) method:

$$\mathbf{y}_i^{(\pm)} = \mathbf{y}_i \pm \delta\mathbf{y}_i, \tag{3.14}$$

where δy_i is known as the slope limiter:

$$\delta\mathbf{y}_i = \frac{\max[(\mathbf{y}_{i+1} - \mathbf{y}_i)(\mathbf{y}_i - \mathbf{y}_{i-1}), 0]}{\mathbf{y}_{i+1} - \mathbf{y}_{i-1}} \tag{3.15}$$

A slope limiter is an expression meant to minimize the numerical oscillations that may happen during the simulation, which is critical when studying shock waves. Expression (3.15) recovers $y_i^{(\pm)} = y_i$ when $y_{i-1} < y_i < y_{i+1}$ or $y_{i-1} > y_i > y_{i+1}$.

[1] Actually, the motivation of finding these redefined fluxes lies in the discontinuities that are inherent to the Eulerian grid. The solution of this issue, called the Riemann problem, is exact, albeit is computationally expensive for its use in fluid mechanics. Therefore, there is a whole industry devoted to find approximate but faster solutions, like the one shown in Figure 3.1. For an interested reader in these topics, I refer to Springel (2016).

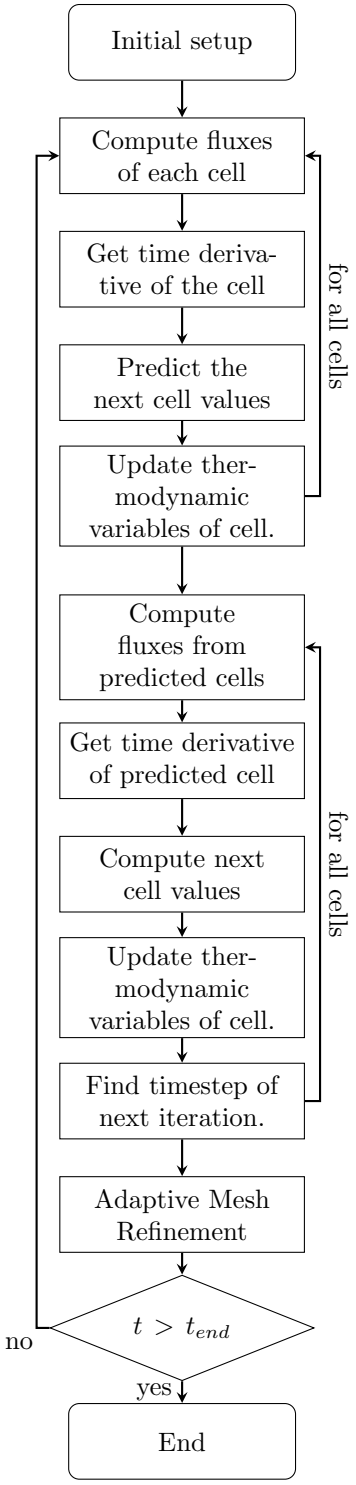

Figure 3.2: Flowchart of the numerical code presented in this chapter.

Evaluated $\mathbf{y}_i^{(\pm)}$, next step is to get $\mathbf{f}_i^{(\pm)}$ and then calculate the corrected fluxes, $\mathbf{F}_i^{(\pm)}$. Here, I use the approximate method developed by Kurganov et al. (2001) (hereinafter KNP, but see also Ziegler, 2004), where they define $\mathbf{F}_i^{(\pm)}$ as:

$$\mathbf{F}_i^{(-)} \equiv \frac{a_{max}^{(-)}\mathbf{f}_{i-1}^{(+)} - a_{min}^{(-)}\mathbf{f}_i^{(-)} + a_{max}^{(-)}a_{min}^{(-)}[\mathbf{y}_i^{(-)} - \mathbf{y}_{i-1}^{(+)}]}{a_{max}^{(-)} - a_{min}^{(-)}} \tag{3.16}$$

$$\mathbf{F}_i^{(+)} \equiv \frac{a_{max}^{(+)}\mathbf{f}_i^{(+)} - a_{min}^{(+)}\mathbf{f}_{i+1}^{(-)} + a_{max}^{(+)}a_{min}^{(+)}[\mathbf{y}_{i+1}^{(-)} - \mathbf{y}_i^{(+)}]}{a_{max}^{(+)} - a_{min}^{(+)}} \tag{3.17}$$

$a^{(\pm)}$ defines the local velocity at the cell interfaces. That is, both the fluid velocity of Euler equations, v; and the sound speed of the medium, c_s

$$c_s = \sqrt{\frac{\gamma P}{\rho}} \tag{3.18}$$

The local speed a can vary between $a_{min} = v - c_s$ and $a_{max} = v + c_s$. Per cell interface, you have to compare the values obtained for both current cell and its corresponding neighbor, which typically are not the same values. For the sake of completeness, I also provide here the formulas for each a of equations (3.16) and (3.17):

$$a_{max}^{(-)} = \max[a_{max,i}^{(-)}, a_{max,i-1}^{(+)}, 0] \tag{3.19}$$

$$a_{min}^{(-)} = \min[a_{min,i}^{(-)}, a_{min,i-1}^{(+)}, 0] \tag{3.20}$$

$$a_{max}^{(+)} = \max[a_{max,i}^{(+)}, a_{max,i+1}^{(-)}, 0] \tag{3.21}$$

$$a_{min}^{(-)} = \min[a_{min,i}^{(+)}, a_{min,i+1}^{(-)}, 0] \tag{3.22}$$

As shown in right panel of Figure 3.1, this flux is able to reproduce the time derivative, albeit with some error inherent of the method.

3.1.1.2 Time integration

Once defined the corrected fluxes, it is possible to compute the time derivative of $\mathbf{y}_i$ as:

$$\frac{d\mathbf{y}_i}{dt} = -(q+1)\frac{r_{i+\frac{1}{2}}^q \mathbf{F}_i^{(+)} - r_{i-\frac{1}{2}}^q \mathbf{F}_i^{(-)}}{r_{i+\frac{1}{2}}^{q+1} - r_{i-\frac{1}{2}}^{q+1}} + \mathcal{G}_i, \tag{3.23}$$

where I changed $\mathbf{f} \to \mathbf{F}$ and $r_{(\pm)} \to r_{i\pm\frac{1}{2}}$ from (3.11) to make clear that you have to compute this derivative per cell.

In addition, I removed the source term in accordance with the ODE solver I am going to use below. In this regard, I follow the predictor-corrector scheme of Doumler and Knebe (2010) to advance $\mathbf{y}_i(t)$ a timestep Δt. First, I compute a predictor, $\mathbf{y}_i^*$, of $\mathbf{y}_i$ at the next timestep as:

$$\mathbf{y}_i^* = \mathbf{y}_i + \Delta t \cdot \frac{d\mathbf{y}_i}{dt} \tag{3.24}$$

Equation (3.24) is (3.13), and the procedure shown until here is roughly the same as introduced in 3.1. Nevertheless, $\mathbf{y}_i^*$ is used as an estimate of $\mathbf{y}_i$ at $t + \Delta t$, and not as a final value, in order to achieve better accuracy. Therefore, the final value $\mathbf{y}_i(t + \Delta t)$, dubbed as the corrector, needs a few more steps. From here, I estimate the value of $\mathbf{y}_i$ at half timestep with the average:

$$\langle \mathbf{y}_i \rangle = \frac{1}{2}(\mathbf{y}_i + \mathbf{y}_i^*) \tag{3.25}$$

Next, fluxes and time derivatives have to be calculated again with the predicted values $\mathbf{y}_i^*$. After that, the corrector, and hence next timestep values of $\mathbf{y}$, are:

$$\mathbf{y}_i(t + \Delta t) = \langle \mathbf{y}_i \rangle + \frac{1}{2}\Delta t \frac{dy_i^*}{dt} + \Delta t \mathcal{U}_i(\langle \mathbf{y}_i \rangle) \tag{3.26}$$

This step is meant to refine the predictor value and get a more accurate result of $\mathbf{y}_i(t + \Delta t)$. That is why source terms $\mathcal{U}$ enter here, evaluated at half timestep values.

3.1.1.3 Computing pressure and thermodynamic variables

To compute relevant thermodynamic variables, I use (3.4) to get pressure first. However, when the fluid is highly supersonic, equation (3.4) gives a negative value due to truncation errors. To avoid this issue, I implement the dual energy formalism of Ryu et al. (1993) (see also Doumler and Knebe, 2010). This consists in introducing a modified entropy

$$S = \frac{P}{\rho^{\gamma-1}} \tag{3.27}$$

as an extra hydrodynamic quantity, whose differential equation is given by

$$\frac{dS}{dt} = \frac{\partial S}{\partial t} + \frac{1}{r^q}\frac{\partial}{\partial r}(r^q S v) = \frac{(\gamma-1)}{\rho^{\gamma-1}}(\dot{u}_H - \dot{u}_C) \tag{3.28}$$

Left-hand side of (3.28) comes from equation (2.4) and (39) from Ryu et al. (1993) and Doumler and Knebe (2010), respectively; whereas right-hand side is the propagation of source terms of mass (3.5) and energy (3.6) Euler equations[2].

Entropy is solved like the other hydrodynamic variables $\mathbf{y}_i$, whose flux being defined as $f_S = Sv$ for its computation in 3.1.1.1.

Before computing the thermodynamic variables, I first check these two conditions per cell:

$$\frac{\epsilon - \frac{1}{2}\rho v^2}{\epsilon} < \delta \tag{3.29}$$

$$\frac{1}{r^q}\frac{\partial}{\partial r}(r^q v) \geq 0 \tag{3.30}$$

The first equation checks if the thermal energy density is below some fraction δ, whereas the latter finds if the cell is not undergoing a shock. About the former, the value $\delta = 0$ is enough to guarantee numerical stability, but I use $\delta = 0.3$ to track temperature accurately even if it is an order of magnitude higher than established by other works (e.g.: Ryu et al., 1993; Doumler and Knebe, 2010; Gentry et al., 2017).

If both (3.29) and (3.30) are true, the pressure is not computed with the energy density, as shown in (3.4), but with the entropy instead:

$$P = S\rho^{\gamma-1} \tag{3.31}$$

Furthermore, the energy density ϵ for that cell, usually found by the equation (3.6), is now calculated with the expression:

$$\epsilon = \frac{1}{2}\rho v^2 + \frac{S\rho^{\gamma-1}}{\gamma-1} \tag{3.32}$$

On the other hand, if either (3.30) or (3.29) are false, entropy is rewritten with (3.31) instead.

Once the pressure has been computed, temperature and source terms $\dot{u}_C$ and $\dot{u}_H$ are obtained by interpolating within the tables[3] obtained from Cloudy, which give these values as function of ρ and P.

Other values that are also computed are the mean atomic weight and the cooling time:

$$\mu = \frac{\rho k_B T}{m_H P} \tag{3.33}$$

$$t_\Lambda = \frac{P}{(\gamma-1)\dot{u}_C} \tag{3.34}$$

where k_B and m_H are the Boltzmann constant and the Hydrogen mass.

3.1.1.4 Finding next timestep

After the values of the current cell, i.e.: $\mathbf{y}_i(t + \Delta t)$, are calculated from (3.26), I compute a dynamic timestep based on the Courant condition:

$$\Delta t_{D,i} = \varepsilon_{CFL}\frac{\Delta r_i}{\max(v_i, c_{s,i})}, \tag{3.35}$$

where Δr is the width of the current cell, and $\varepsilon_{CFL} < 0.5$ for numerical stability. Next, I compare with a cooling timestep, defined as $\Delta t_{\Lambda,i} = \varepsilon_\Lambda t_\Lambda$ where ε_Λ serves the same purpose as ε_{CFL}. The optimal timestep for the current cell is then $\Delta t_i = \min(\Delta t_{D,i}, \Delta t_{\Lambda,i})$, and the next timestep used for advancing time is the smallest Δt among all cells.

[2]Proof: Thermal energy density is $u = P/(\gamma-1)$, then $\frac{du}{dt} = \dot{u} = \dot{u}_H - \dot{u}_C = \frac{\dot{P}}{\gamma-1}$. If total derivative of S is computed, then $\dot{S} = \frac{\dot{P}}{\rho^{\gamma-1}} - (\gamma-1)\frac{P}{\rho^\gamma}\dot{\rho}$. Second term is zero because there are not mass sinks or sources in (3.5), while the first becomes the right-hand side of (3.28).

[3]Early builds were made with the Grackle chemistry and cooling library (Smith et al., 2017, https://grackle.readthedocs.io/) for thermodynamic calculations. For this code, it was used in its *equilibrium mode* and only for radiative cooling (i.e.: chemistry functions of Grackle were not included). In practice, this code asked Grackle to compute the temperature following a iterative process and then read self-tabulated tables from Cloudy to compute the cooling time (see their section 4.1.2). Later, heating ($\dot{u}_H$) was included in the SNR code by reading tabulated tables originating in Cloudy. By consistency and because I was doing the same as I was asking to Grackle, I dropped Grackle in favour of these new interpolating tables of T and $\dot{u}_C$ from the same Cloudy simulation as the heating table.

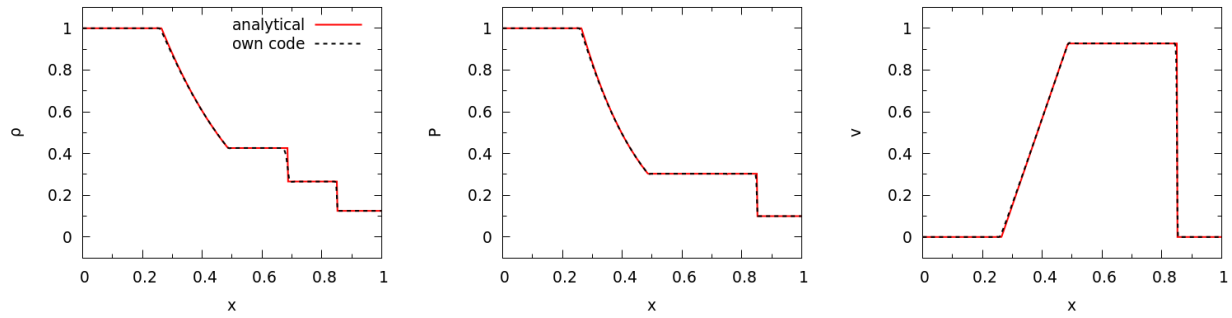

Figure 3.3: Density, pressure and velocity, in favourite units, of the Sod shock test at $t = 0.2$. Dashed line represent this code output while solid line is the analytical result of cococubed webpage.

3.1.1.5 Adaptive Mesh Refinement

An AMR consists in modifying the grid of cells during runtime to achieve an optimal spatial resolution. That is, adding more cells in regions to increase resolution (e.g.: in shocks), and removing them in others where having too many cells is inefficient (e.g.: constant values).

In this code, I implemented AMR by defining a pool of cells. Per time iteration, some cells in the pool are used for the calculation and some others do not. Used cells know who are their neighbors with two pointers (left and right), and so it implicitly defines the grid of that iteration. For the very first timestep, all cells begin at maximum refinement allowed, which is defined by the user, thus using the full pool.

Merging two cells means that one of them become unused for the next iteration. I follow a criterion based on energy density to merge cell i with $i+1$

$$|\frac{\epsilon_{i+1} - \epsilon_{i-1}}{\epsilon_i}| < 0.005, \tag{3.36}$$

as long as both have the same resolution.

On the other hand, splitting a cell takes an unused one from the pool. The criterion used is also (3.36) but when the quotient is higher than 0.1 and the target cell is not at maximum refinement. If the latter is true, I split its closest neighbors instead unless they are also at maximum refinement.

3.1.2 Test cases

3.1.2.1 Sod shock tube

To validate this code, I first perform the well-known Sod shock tube test (Sod, 1978). It consists in a region between $x = 0$ to $x = 1$, in Cartesian coordinates, with these initial conditions:

$$\rho = \begin{cases} 1 & ; \quad x < 0.5 \\ 0.125 & ; \quad x \geq 0.5 \end{cases} \quad ; \quad P = \begin{cases} 1 & ; \quad x < 0.5 \\ 0.1 & ; \quad x \geq 0.5 \end{cases} \quad ; \quad v = 0 \tag{3.37}$$

in your favourite units. The simulation is run from $t = 0$ to $t = 0.2$, and with adiabatic constant of 1.4, following Sod (1978). Any cooling/heating processes are deactivated.

Figure 3.3 shows own code against the exact solver found in the cococubed webpage[4]. Both solutions found that the contact discontinuity of (3.37) has evolved to a rarefaction to the left whereas the shock advances to the right, without any differences between them.

3.1.2.2 Comparison against Flash

Finally, I also run the same SNR simulation with this code and FLASH v4 (Fryxell et al., 2000). On one hand, this allows to do the Sedov-Taylor test, which is one of the phases of a SNR and also a standard hydrodynamical test. On the other hand, radiative cooling can be tested as well since both codes have a different implementation, but share the same cooling function.

I show in Figure 3.4 three snapshots at different times of the evolution of a SNR with a ejected mass of $10\,M_\odot$ in an homogeneous medium of $\frac{\rho_0}{m_H} = 0.5\,\mathrm{cm}^{-3}$ and $T_0 = 10^4\,\mathrm{K/cm}^3$. First panel reflects the Sedov-Taylor phase of the SNR, when cooling is not relevant. The agreement between shock profiles is excellent but they show differences in the ambient pressure, outside the SNR.

[4] http://cococubed.asu.edu/code_pages/exact_riemann.shtml

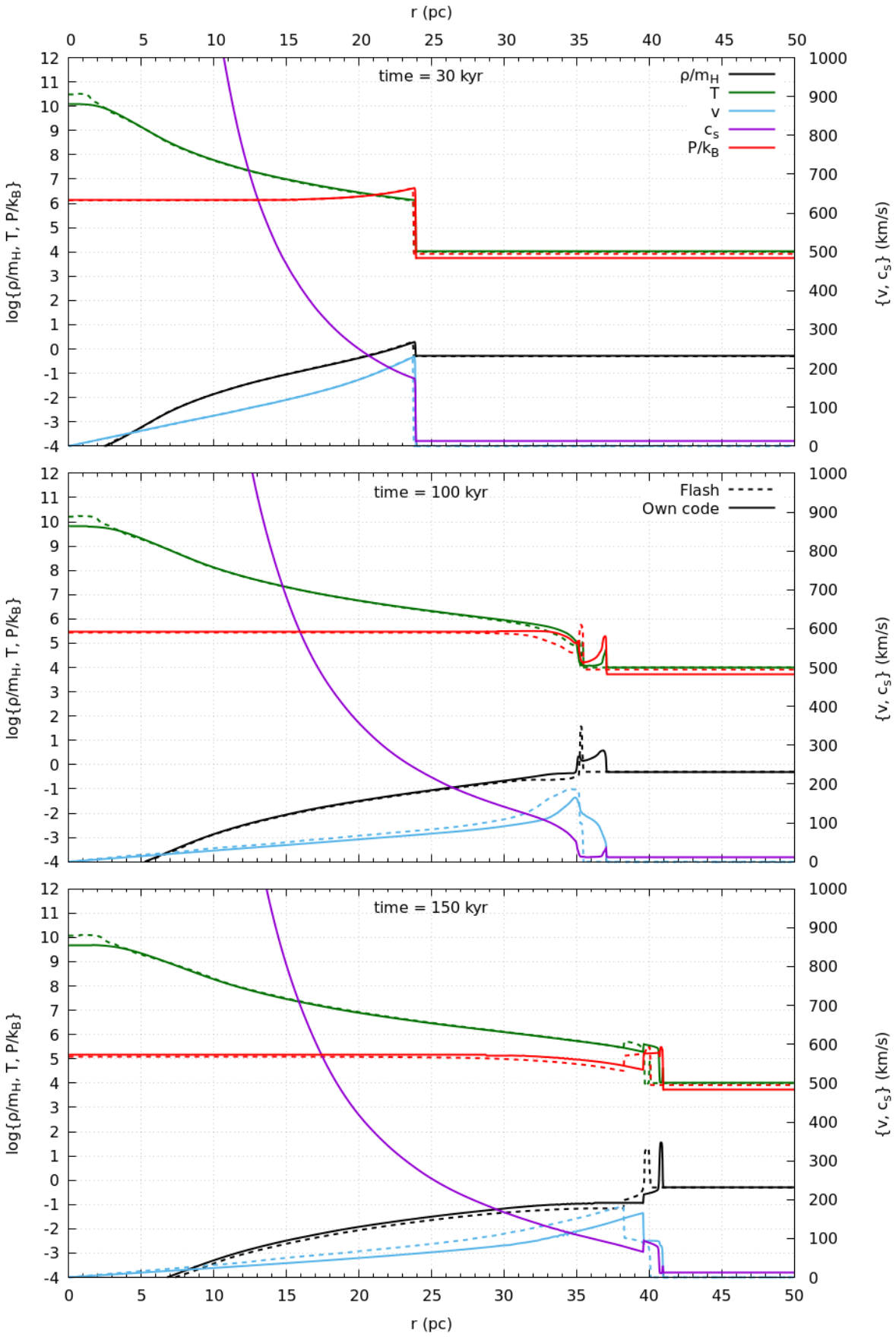

Figure 3.4: Comparison between FLASH (solid lines) and this code (own, dashed lines) for several quantities: mass density $\rho/m_H\,(\mathrm{cm}^{-3})$, temperature $T\,(\mathrm{K})$, fluid and sound velocities $v, c_s\,(\mathrm{km/s})$ and pressure $P/k_B\,(\mathrm{K/cm}^3)$ in different colors, as labelled. Upper panel shows the SNR during its Sedov-Taylor phase, middle panel when own SNR forms its shell, and the bottom panel is the radiative phase.

Computing the atomic weight with (3.33), FLASH gives a value of $\mu \approx 0.5$, proper of ionized medium, for the whole domain; whereas own code gives $\mu \approx 1$, which characterizes warm medium, outside the SNR. This discrepancy propagates when shell is forming, as FLASH begins earlier and ends behind own SNR with slight differences in the shell profile.

3.1.3 Detecting shocks in supernova remnants

With an hydrodynamical code, it is not evident to the machine what cells in the grid does belong to a shock. To detect it, I follow the criteria given in Schaal and Springel (2015) and Pfrommer et al. (2017):

$$\nabla \cdot \mathbf{v} < 0 \tag{3.38}$$

$$\nabla T \cdot \nabla \rho > 0 \tag{3.39}$$

$$\mathcal{M} > 1.3 \tag{3.40}$$

The first condition implies that the cell is being compressed, whereas the second one discriminates a shock wave from a cold front discontinuity. Ideally, the Mach number $\mathcal{M}$ should be higher than 1 to find a shock, but a higher value is recommended to avoid false positives caused by spurious numerical oscillations in the thermodynamical variable.

For supernova remnants, this analysis can be done at post-process, after the simulation. Moreover, for isolated SNR in a homogeneous medium, the shock radius $R(t)$ will always be the farthest shock detected from the initial explosion at $t = 0$.

3.2 Supernova remnants in the solar neighborhood

3.2.1 The pre-supernova interstellar medium

I first want to make an emphasis into the conditions of the ISM where the supernova explosion takes place, as they are the initial conditions of the hydrodynamic simulation and can significantly alter the evolution and extension of SNR. Early classical studies of SNR (e.g.: Chevalier, 1974; Thornton et al., 1998, and references therein) have focused on solar-neighborhood like environments, with different, but constant along the simulation, ISM densities and metallicites. I would like to briefly review what happens if you change anyone of these conditions:

1. **Location**: This generally implies to change the density to a very low value ($n \lesssim 10^{-2}$ cm^{-3}, to give an upper limit). This means that the SNR will follow the non-radiative path of Figure 2.2, from previous chapter. These SNR does certainly exist, as these low densities occur in elliptical galaxies or outside a disk in a spiral one (Hakobyan et al., 2017; Barkhudaryan et al., 2019, for a statistical study). SNR under these conditions were found in Dorfi and Voelk (1996) and later described in Tang and Wang (2005): No cooling takes place, which implies that the SNR ends retaining all its energy during its whole evolution.

2. **Inhomogeneities**: Realistically, the ISM is far from homogeneous and it leads to the fragmentation of the SNR shell. However, inhomogeneities do not alter the momentum and energy injection into the ISM by more than a factor of 2 (Walch and Naab, 2015; Martizzi et al., 2015; Kim and Ostriker, 2015) compared to those made in homogeneous media.

3. **Nearby previous events**: these events refer, mainly, to the radiation from the progenitor star (Green, 2014; Walch and Naab, 2015) and previous SNR (Sharma et al., 2014; Keller et al., 2014; Gentry et al., 2017, 2019), which form superbubbles. Their effects are more indirect than previous one, because they can alter the distribution of the ISM density near them.

A difference that it is not fully explored is the external radiation field (ERF) that comes from far sources, within and outside the galaxy, and it is known that plays an important role in determining the physical conditions of the ISM (Wolfire et al., 1995).

Since the purpose of this chapter is to convince the reader that radiation fields matter in SNR evolution, I will restrict the ISM to the solar neighborhood for this section, because they are the usual initial conditions found in SNR works in the literature. Nevertheless, I discuss briefly what may happen if you combine different heating fields and locations in 3.3.

3.2.1.1 The average radiation field approximation

To correctly model the impact of radiation in the interstellar gas, I have to consider both the cooling and heating processes. Although a detailed study of radiation would involve radiative transfer, I present here an approximate method.

Commands	Comments
`# INPUT`	
`hden [value1]`	$\log(n_{H,0})$
`abundances ism`	Add `no grains` to remove dust.
`table ISM`	Interstellar radiation field
`table HM12 redshift 0`	Haardt and Madau (2012) extragalactic background
`CMB`	Cosmic Microwave Background
`cosmic rays background`	Cosmic-Ray H^0 ionization rates (see caption)
`stop column density [value2]`	$\log(N_{H,eff})$
`stop temperature off`	To allow CLOUDY to proceed when $T < 10^4$ K
`iterate to convergence`	To get optimal accuracy in the output
`# OUTPUT`	
`save transmitted continuum "Filename1" last`	$4\pi\nu J_{\nu,0}(n_{H,0}, N_{H,eff})$ of last iteration
`save abundances "Filename2" last`	Saves number density of each element, from H to Zn
`save overview "Filename3" last`	save different magnitudes (see text)

Table 3.1: CLOUDY input needed in order to generate the average radiation field. Default values of `abundances ism` are shown in Table A.1. Cosmic ray H^0 ionization are the default values given in Glassgold and Langer (1974) and Indriolo et al. (2007).

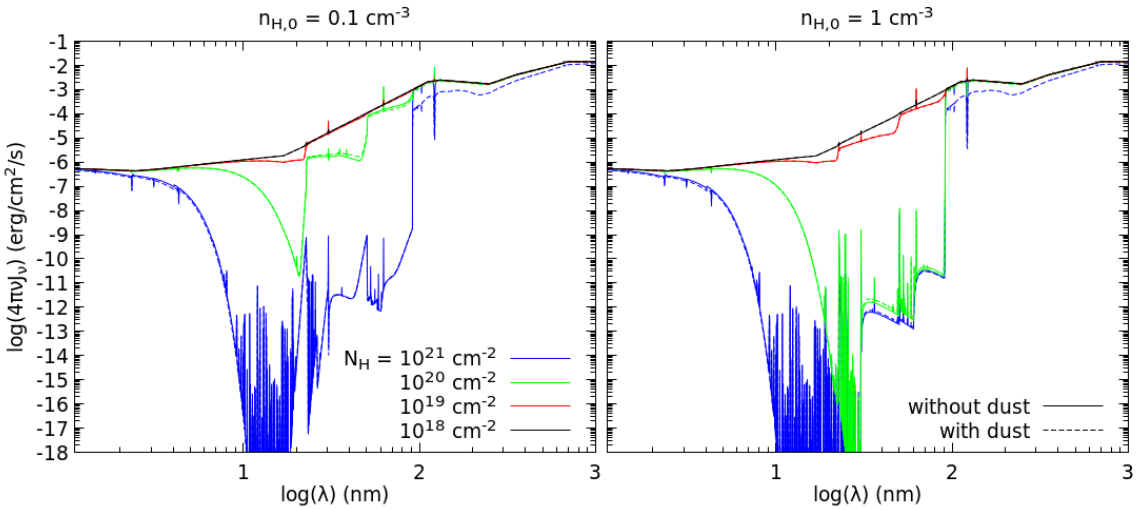

Figure 3.5: Transmitted continuum spectra given by CLOUDY for different combinations of $n_{H,0}$ and $N_{H,eff}$. Dashed and solid lines represent if the computation have been done with `no grains` or not (see Table 3.1). This figure was originally shown in Romero et al. (2021).

I utilize the photoionization code CLOUDY v17.01 (Ferland et al., 2017) to compute the ERF that traverses a region with a ambient number density, $n_{H,0}$. In this regard, I compute the radiation field attenuated beforehand by the interstellar gas that lies outside the physical region of interest (e.g.: the simulation domain of a hydrodynamic code). This effect can be parametrized by an effective Hydrogen column density, $N_{\mathrm{H},eff}$. It reflects the effective optical depth towards the unabsorbed radiation sources, and hence it may depart from the simple expectation $N_{\mathrm{H},eff} \sim n_{\mathrm{H},0} l$, where l is the spatial extent of the physical region. For instance, it would be larger if most of the surrounding ionising stars are heavily obscured, while it would be lower if they find a clear line of sight towards the ambient medium.

I show in Table 3.1 the input to generate the average radiation field, expressed in $4\pi\nu J_{\nu,0}$, given $(n_{H,0}, N_{H,\mathrm{eff}})$ as parameters. I plot in Figure 3.5 the main result as a function of wavelength for the UV and X-ray range. The selected values of $\{n_{H,0}, N_{H,\mathrm{eff}}\}$ are meant to represent the warm ionized and atomic medium of the ISM, consistent with Wolfire et al. (1995) and Ferrière (2001). $N_{H,\mathrm{eff}} = 10^{21}\,\mathrm{cm}^{-2}$ is higher than the values expected for the solar neighborhood, but these column densities can be found in the Milky Way (see the Figure 1 of Ferrière, 2001) and other galaxies can reach even higher values, according to observational data (Leroy et al., 2008).

Figure 3.5 shows two major regimes: On one hand, shielded cases, found for ($N_{H,\mathrm{eff}} \gtrsim 10^{21}\,\mathrm{cm}^{-2}$ for $n_{H,0} = 0.1\,\mathrm{cm}^{-3}$ or $N_{H,\mathrm{eff}} \gtrsim 10^{20}\,\mathrm{cm}^{-2}$ for $1\,\mathrm{cm}^{-3}$, where the UV radiation of external sources are heavily absorbed by the interstellar gas. On the other hand, unshielded cases, found for $N_{H,\mathrm{eff}} \lesssim 10^{20}\,\mathrm{cm}^{-2}$ for

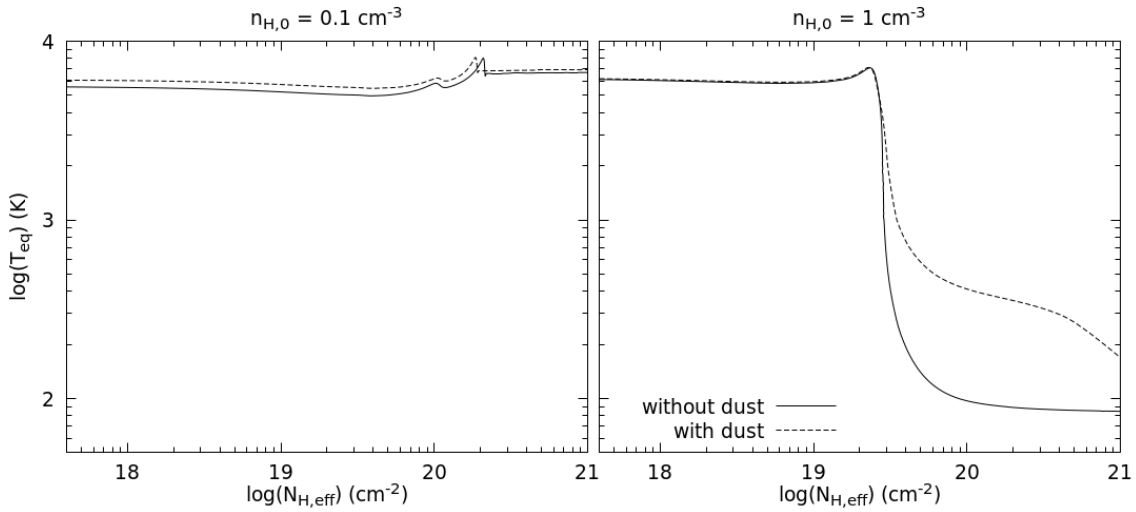

Figure 3.6: Equilibrium temperature of the cloud modelled in CLOUDY as a function of effective column density. This figure was originally shown in Romero et al. (2021).

$n_{H,0} = 0.1\,\mathrm{cm}^{-3}$ or $N_{H,\mathrm{eff}} \lesssim 10^{19}\,\mathrm{cm}^{-2}$ for $1\,\mathrm{cm}^{-3}$, where the ionizing radiation reaches the environment without being absorbed.

We will see that this distinction have major implications in the subsequent results presented for the solar neighborhood. Other output that can be obtained is the equilibrium temperature of the ISM, T_{eq}, which is shown in Figure 3.6. In general, the equilibrium temperature of the unshielded cases is of the order of $\sim 7000\,\mathrm{K}$, whereas it drops by more than an order of magnitude for the shielded cases. For $n_{\mathrm{H},0} = 0.1\,\mathrm{cm}^{-3}$, however, if $N_{\mathrm{H,eff}} = 10^{21}\,\mathrm{cm}^{-2}$, a warm T_{eq} is maintained, due to the effect of the cosmic-ray heating. The cooling and heating functions, on the other hand, are similar to the other shielded cases.

Both Figure 3.5 and 3.6, and subsequent results at this chapter, consider the presence of dust in the ISM to only bracket the maximum possible impact of dust heating and cooling (or lack thereof) on the evolution of the SNR [5]. This is achieved by adding `no grains` command after `abundances ism` in the CLOUDY input to remove dust. The presence of dust in the ISM has only a minor effect on the final spectrum in the vicinity of the SNR, which is almost fully determined by the effective column density $N_{\mathrm{H,eff}}$ and the ambient density $n_{\mathrm{H},0}$, but it will have a significant impact on the cooling and heating functions at high gas temperatures, as we will see.

3.2.1.2 Cooling and heating functions

In order to handle heating and cooling in the environment, we assume that each simulation cell is illuminated by the mean radiation field computed in previous section for the selected ambient hydrogen density and equilibrium temperature. To do that, I perform a second CLOUDY using the spectra of Figure 3.5 as incident radiation field of the cloud, while keeping the other characteristics of the ISM identical to those of the ambient medium. This new input is shown in Table 3.2

Commands	Comments
`# INPUT`	
`hden [value1]`	$\log(n_{H,0})$
`abundances ism`	Add `no grains` to remove dust (see Table 3.1)
`table read "Filename2" scale 1`	Radiation field obtained in Table 3.1
`cosmic rays background`	Cosmic-Ray H^0 ionization rates (see Table 3.1)
`# OUTPUT`	
`save map "Cooling", zone 0 range 1 to 9`	Saves $\dot{u}_C$ and $\dot{u}_H$ between $T = 10$ to 10^9 K.

Table 3.2: CLOUDY input needed in order to generate $\dot{u}_C$ and $\dot{u}_H$, needed for equation (3.6). This input is generated for a range of Hydrogen densities between 10^{-6} to $10^4\,\mathrm{cm}^{-3}$.

The relevant outputs are the quantities $\dot{u}_H$ and $\dot{u}_C$ at the illuminated face of the cloud (i.e.: when the radiation field hits the start of the cloud modelled in CLOUDY), which are saved as a function of the temperature

[5] Dust has additional effects on SNR evolution, and vice-versa, but they are outside the scope of this chapter. I refer the interested reader to see Slavin et al. (2015); Martínez-González et al. (2019); Priestley et al. (2021) and references therein.

(between 10 and 10^9 K) and Hydrogen density (from 10^{-6} to $10^4\,\mathrm{cm}^{-3}$) that the gas cells may reach during the simulation. These values should not to be confused with the initial values T_{eq} and $n_{\mathrm{H},0}$ of the ambient medium, which are the initial conditions of the hydrodynamic simulation.

Then, I translate the output of this second CLOUDY run, $\dot{u}_C$ and $\dot{u}_H$ as a function of n_H and T, to a set of three tables, giving $\{T, \dot{u}_C, \dot{u}_H\}$, in terms of the total mass density ρ and the pressure P of the gas cell, which are the physical variables internally used by the hydrodynamical code (see section 3.1.1.3). Mass density is computed from the number densities of all elements considered in CLOUDY

$$\rho = \sum_{i=H}^{Zn} A_i n_i m_H \tag{3.41}$$

Pressure can be also obtained from the number densities of each element plus the contribution of free electrons in the ISM:

$$P = (n_e + \sum_{i=H}^{Zn} n_i) k_B T \tag{3.42}$$

Figure 3.7 shows the cooling and heating functions of the interstellar gas

$$\Lambda \equiv (\tfrac{\mu m_H}{\rho})^2 \dot{u}_C \quad ; \quad \Gamma \equiv \frac{\mu m_H}{\rho} \dot{u}_H \tag{3.43}$$

for both shielded and unshielded cases. Figure 3.8 displays the ratio between heating and cooling rates, $\dot{u}_H/\dot{u}_C$.

For each one of these three quantities, we have four panels, the top rows plot two representative examples of the unshielded cases, while bottom rows show shielded ones. In turn, left columns show dust-free media, while the effect of dust particles is illustrated on the right ones. In general terms, shielded and unshielded cases present different behaviour at temperatures below $\sim 10^4$ K, whereas dust tends to increase them above $\sim 10^5$ K and $\sim 10^4$ K, respectively.

As can be seen in Figure 3.8 differences in the heating rate are irrelevant for $T > 10^4$ K and $\frac{\rho}{m_H} > 10^{-2}\,\mathrm{cm}^{-3}$, because heating is absolutely negligible compared to cooling in this regime. At high temperatures, though dust becomes the main cooling agent, and it dramatically enhances the cooling rate at $T > 10^6$ K. A detailed treatment of the destruction of dust grains would be of the utmost importance in order to accurately model the cooling rate, but we consider that the two extreme cases may illustrate the associated uncertainties on the evolution of SNR.

In any case, the gas will eventually cool down towards the equilibrium temperature. For temperatures lower than 10^4 K, there are obvious qualitative differences between the shielded and unshielded cases. If the ISM radiation field is heavily attenuated, the cooling function is very close to collisional ionisation equilibrium, and the heating function is similar, albeit slightly lower, to the $2 \cdot 10^{-26}$ erg/s advocated by Koyama and Inutsuka (2002). For shielded cases, the ratio $\dot{u}_H/\dot{u}_C$ between the heating and cooling rates is very sensitive to the gas density, as the colored region is very wide in the lower panels of Figure 3.8, and it is flat on the temperature range between $\sim 10^2$ and 10^4 K. For that reason, the equilibrium temperature of the ISM changes drastically between these extremes at densities around $\sim 1\,\mathrm{cm}^{-3}$.

This contrasts with unshielded cases, where heating is indisputably more important than cooling for $T < 10^4$ K. No gas can exist for long periods of time below that temperature because there are not any density crossing the black line in Figure 3.8. This situation is akin to the classical models where the radiation field is ignored, but cooling is manually switched off below a certain threshold of the order of the equilibrium temperature.

3.2.2 Supernova remnant evolution under a external radiation field

3.2.2.1 Initial conditions

Once the numerical code and the environment have been set, I can now proceed to compute SNR simulations. In this case, I select a sample of simulations with $n_{H,0} = \{1, 0.1\}\,\mathrm{cm}^{-3}$, with column densities of $N_{\mathrm{H,eff}} = \{10^{18}, 10^{19}, 10^{20}, 10^{21}\}$ cm^{-2}, which establishes the initial temperature, T_{eq}, according to figure 3.6. These conditions are used twice, one without dust, and a second with it.

Each simulation consists of a sphere of radius $8 \cdot 10^{20}$ cm (≈ 260 pc). I use a pool of 52000 cells within the AMR scheme, giving a maximum resolution of roughly 0.005 pc.

At $t = 0$, the simulation starts modelling a Sedov-Taylor phase, thus skipping the ejecta-dominated phase that comes before. To achieve that, energy density and entropy are injected following the recipe given by Truelove and McKee (1999) for the first 400 cells closest to the center:

$$\epsilon_i = \epsilon_0 + \tfrac{E_0}{\Delta V_i} f(\tfrac{r_i}{5\Delta r_i}) \tag{3.44}$$

$$S_i = (\gamma - 1)\tfrac{\epsilon_i}{\rho_i^{\gamma-1}}, \tag{3.45}$$

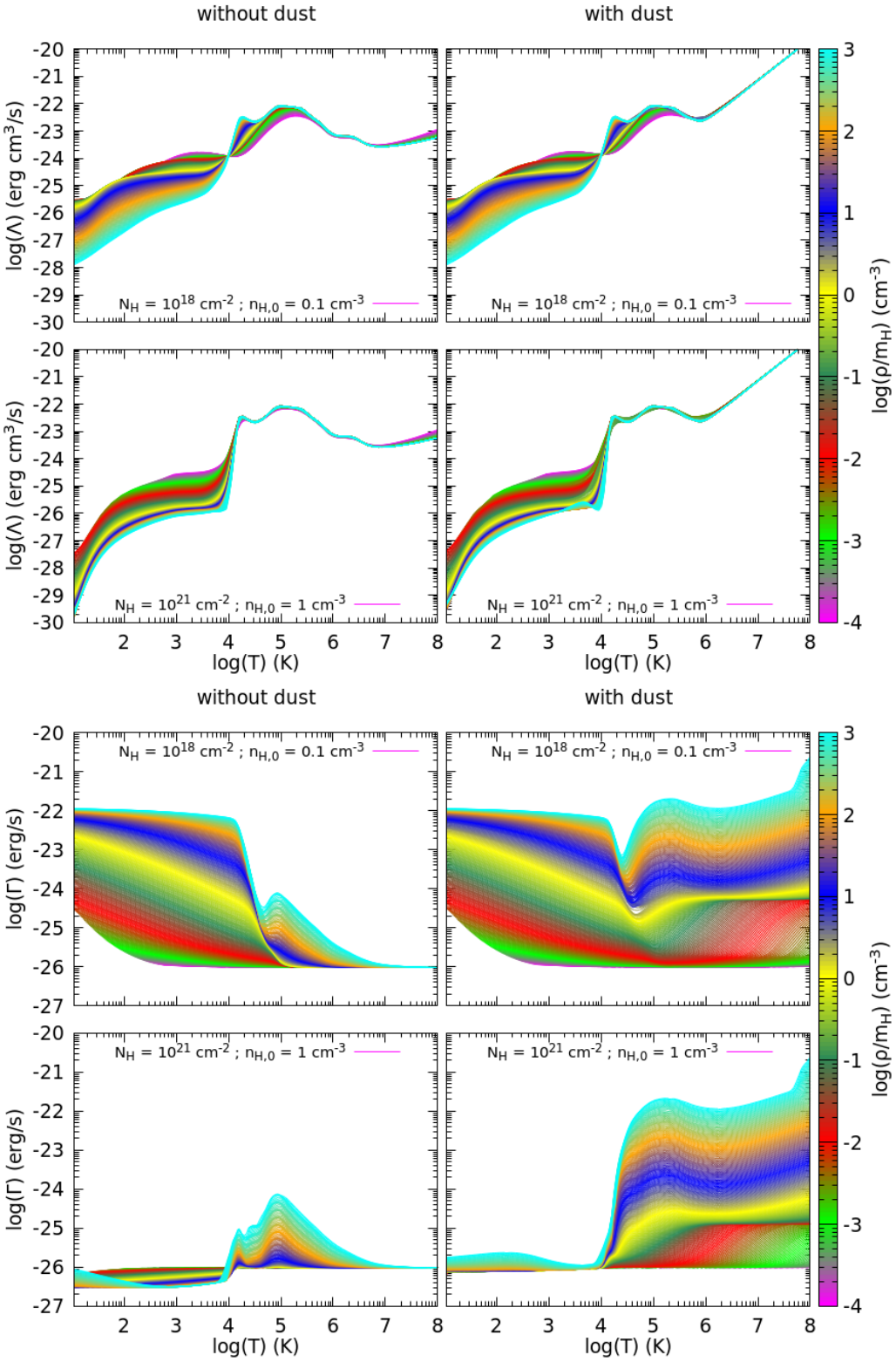

Figure 3.7: Cooling ($\Lambda \equiv (\frac{\mu m_H}{\rho})^2 \dot{u}_C$, upper panel) and heating ($\Gamma \equiv \frac{\mu m_H}{\rho} \dot{u}_H$, bottom panel) functions of four representative cases. Top and bottom rows within each panel show unshielded and shielded cases, respectively. This figure was originally shown in Romero et al. (2021).

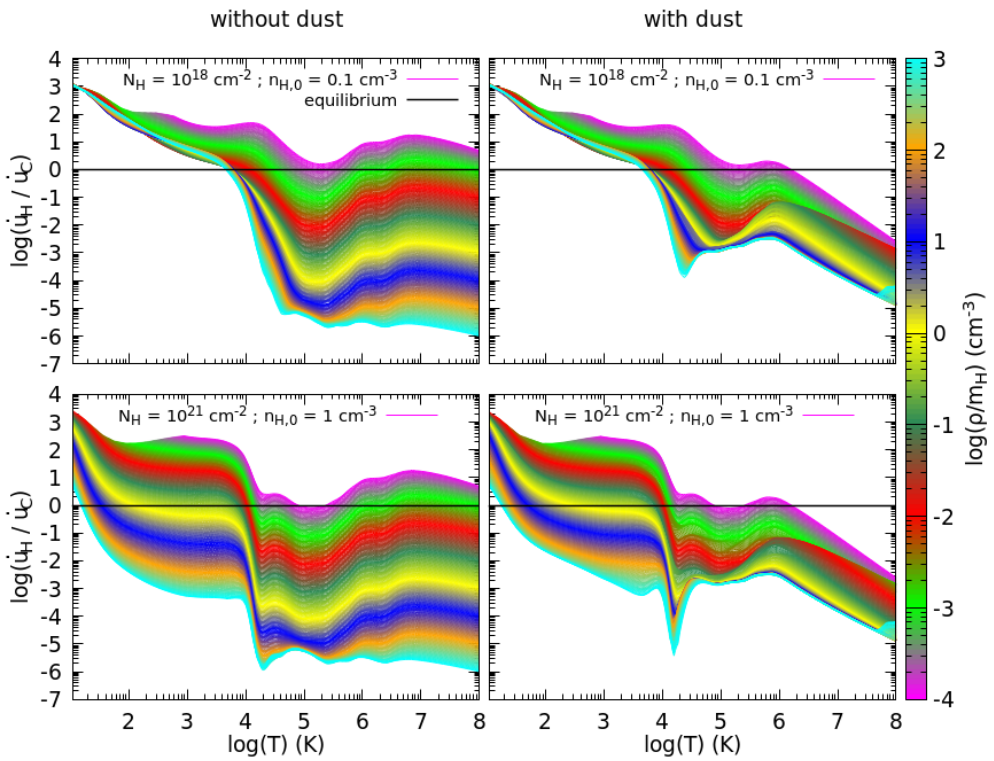

Figure 3.8: Ratio between energy density gain ($\dot{u}_H$) and loss ($\dot{u}_C$) due to radiative processes, for the same four cases of Figure 3.7. Any point with color represent a gas with some density and temperature, whereas the black line represents the (radiative) equilibrium. Therefore, anything above the line will heat towards the equilibrium and will cool if the point is below the line. Top and bottom rows within each panel show unshielded and shielded cases, respectively. This figure was originally shown in Romero et al. (2021).

where $E_0 = 10^{51}\,erg$, ΔV_i and Δr_i are the cell volume (cm^3) and width (cm), respectively, and $f(x) \propto e^{-x^2}$, is a function normalized to 400 cells.

In an astrophysical context, this set up is valid for an isolated explosion. This case may correspond to a white dwarf exploding as SN Ia or a runaway OB star (Gies and Bolton, 1986). These events can take place anywhere within the ISM, albeit they are more likely to occur in the disk (Johnson and MacLeod, 1963; Hakobyan et al., 2017).

3.2.2.2 Energy and momentum injection to the ISM

I start with the quantities that are usually found in the literature when studying SNR evolution, which are energy and momentum injected to the ISM.

Once $R(t)$ defined following 3.1.3, energy and momentum injected are calculated by the integrals:

$$E(t) = \int_0^{R(t)} \epsilon \; 4\pi r^2 dr \tag{3.46}$$

$$p(t) = \int_0^{R(t)} (\rho v) \; 4\pi r^2 dr \tag{3.47}$$

In order to show the importance of energy radiated by the SNR, the luminosity of the SNR is also computed as:

$$L(t) = \int_0^{R(t)} \dot{u}_C \; 4\pi r^2 dr \tag{3.48}$$

The evolution of these quantities is plotted in Figure 3.9. From the point of view of SNR dynamics, there is barely any significant difference between shielded and unshielded cases as long as the shock remains strong ($\mathcal{M} \gg 1$). For instance, at 1 kyr, differences in radius and momentum are less than 5 and 10 percent, respectively. Energy, on the other hand, show higher differences, up to a factor of 2, because the shock is no longer strong in the unshielded case. In the weak-shock regime, at the latest stages of the evolution, the equilibrium temperature and pressure, T_{eq} and P_{eq}, of the ambient medium become relevant, explaining the changes in R, E and p at late times that one can observe in Figure 3.9. Basically, the sound speed is lower in the shielded cases, and therefore the weak shock regime, as well as the associated upturn in the total energy within the SNR, are delayed with respect to the unshielded cases. These results suggest that a more complex heating and cooling scheme would

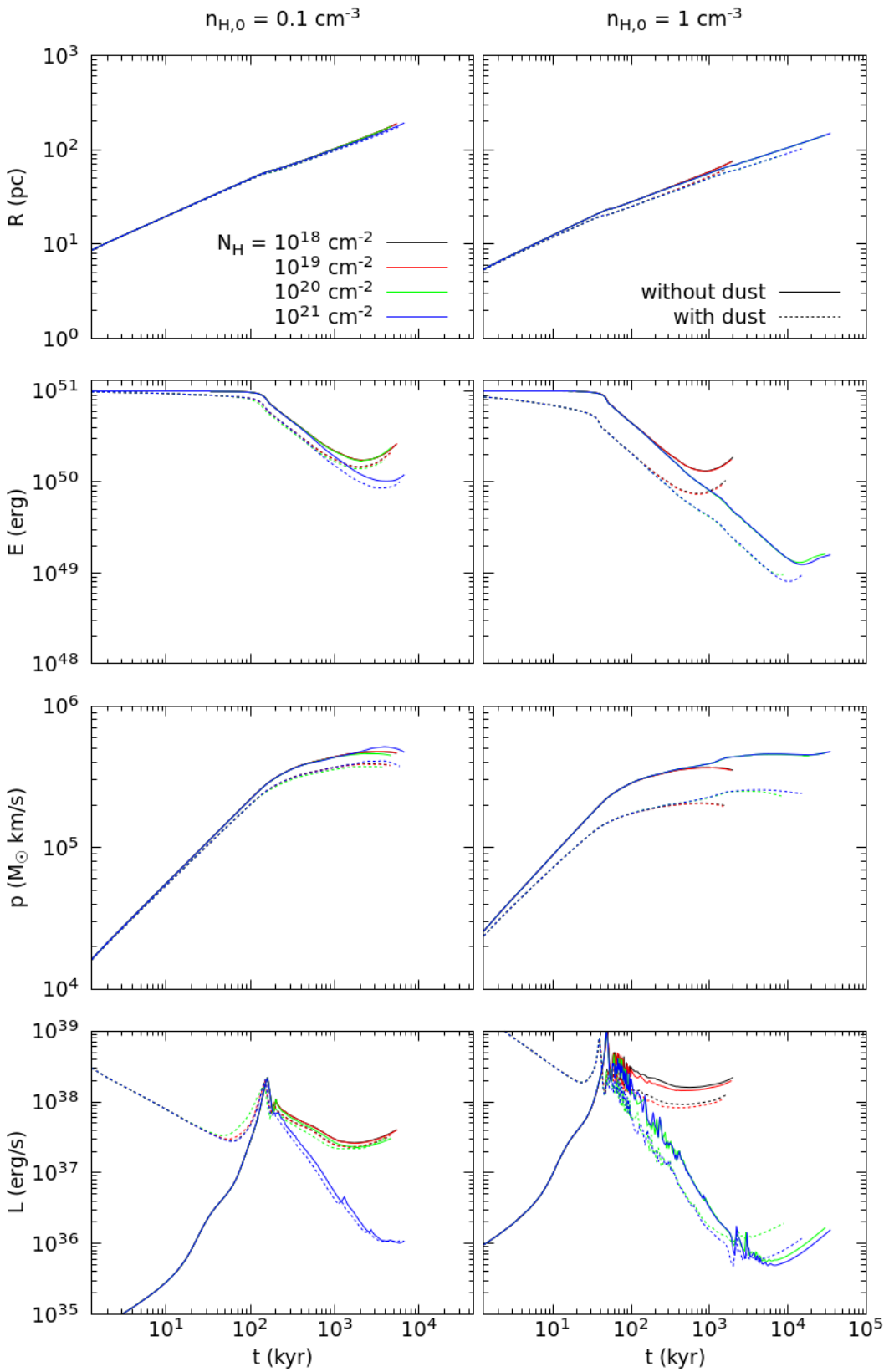

Figure 3.9: Temporal evolution of the shock radius, R, total energy, E, momentum, p, and luminosity, L, as function of time for all SNR cases. This figure was originally shown in Romero et al. (2021).

not have a strong effect on the evolution of the SNR as a whole (i.e. shock radius, total energy and momentum), in agreement with the recent results reported by Sarkar et al. (2021).

The evolution of the shielded cases is consistent with the results of previous studies based on the Koyama and Inutsuka (2002) heating prescription (e.g. Walch and Naab, 2015; Kim and Ostriker, 2015; Haid et al., 2016), while unshielded cases match the evolution obtained by switching off cooling at a warm equilibrium temperature (e.g. Cioffi et al., 1988; Thornton et al., 1998; Martizzi et al., 2015; Slavin et al., 2015; Pittard, 2019).

However, the balance between heating and cooling processes is very different under both situations, even if the net effect is similar. In the end, the SNR must dissipate the kinetic energy of the gas that is incorporated to the shock, $L_{\rm iso} = 2\pi\rho_0 R^2 \dot{R}^3$ (see e.g. Cioffi et al., 1988, or 2.3.3), which is roughly the same in both cases, given that the evolution of the shock radius is almost identical. On the other hand, the energy absorbed from the radiation field is radically different for a shielded and unshielded environment, being significantly higher for the latter. The heating rate is thus much higher, but the total cooling rate (i.e. the luminosity of the SNR) increases as well, until the bulk of the absorbed energy is immediately re-radiated by the gas, and it has a minor impact on the evolution of the shock radius and the integrated energy and momentum.

The presence or absence of dust particles does not alter this conclusion, although it plays a significant role in the SNR dynamics at early times, when the temperature of the hot interior is higher than 10^6 K and dust is the major coolant. If the supernova ejecta enriched the gas with newly synthesised dust and/or a fraction of the pre-existing grains survived the shock passage, radiative losses during this phase will not be negligible, at variance with the classical Sedov-Taylor regime. Once the post-shock temperature drops below $\sim 10^5$ K, other cooling agents become dominant, and shell formation proceeds exactly as in the classical case. The main difference is that the energy lost during early evolution is not negligible (about 10 percent for $n_{H,0} = 0.1\,{\rm cm}^{-3}$ and 40 percent for $n_{H,0} = 1\,{\rm cm}^{-3}$). Shell formation happens slightly sooner in the dusty simulations, and early radiative losses result in a lower final energy and momentum injection into the ISM.

3.2.2.3 Internal structure of the shell

Figures 3.10 and 3.11 show the radial profiles of gas density and temperature, directly taken from the code output, near the shock as a function of r/R, where r is the radial coordinate, for a few times between 50 to 1600 kyr, mostly focused on the radiative phase of the SNR evolution. Figures 3.10 and 3.11 also include the luminosity internal profile, which is equation (3.48) with the upper limit changed to r:

$$L(r,t) = \int_0^r \dot{u}_C 4\pi r'^2 \, dr' \tag{3.49}$$

After the Sedov-Taylor phase, unshielded and shielded cases diverge significantly in the predicted structure of the post-shock shell. Unshielded shells become thicker and less dense over time, displaying a structure that is similar to a classical isothermal shock. On the other hand, shielded cases are better described by the infinitely thin-shell approximation over a long period of time. Its density is much higher, and its temperature much lower, than the unshielded case. At very late times, though, shielded cases eventually develop a warm region at $T \sim 10^4$ K after the shock, roughly similar (albeit much thinner) to the unshielded case. The thin shell, about two orders of magnitude colder, is slightly displaced inwards, delineating the boundary between the warm region and the hot bubble.

As mentioned above, there are important differences in the total luminosity radiated by the shielded and unshielded cases after the shell is formed. Moreover, the physical properties of the emitting gas and the structure of the emission are very different in both scenarios. In the unshielded case, the emissivity is smoothly distributed over the shell, and cooling is dominated by the recombination and collisional emission lines characteristic of a $T \gtrsim 10^4$ K gas, above the equilibrium temperature. In contrast, the (much lower) luminosity of the shielded case may be separated into the contribution of the gas cooling from the post-shock temperature to the equilibrium temperature, which is similar to the unshielded case, and the emission from the very dense, cold shell at ~ 100 K near the hot bubble. The fractional contribution of the latter varies from with time, but it is always of the order of $\sim 20 - 50$ per cent. The warm region between them at $T \sim T_{eq}$ has no significant contribution.

The physical reason between these differences can be understood from the ratio between the heating and cooling rates depicted in Figure 3.7. In the unshielded cases, is barely impossible for the gas to cool down below the equilibrium temperature, whereas a much wider range of stable configurations exist in the shielded scenario, where sufficiently dense gas is allowed to reach much lower temperatures.

Although dust particles may effect the evolution in time of the shock radius, they barely have any impact on the morphology of the shell during the strongly radiative phase. Simulations including dust feature a shorter cooling time (see Figure 3.9), and therefore the profiles shown in Figure 3.10 correspond to a more evolved state. In addition, the presence of dust also affects the equilibrium temperature of the ambient medium (see Figure 3.6), as well as the heating and cooling rates of the post-shock gas. Although this plays a major role on the total luminosity radiated by the SNR, it has a minimal effect on its internal structure.

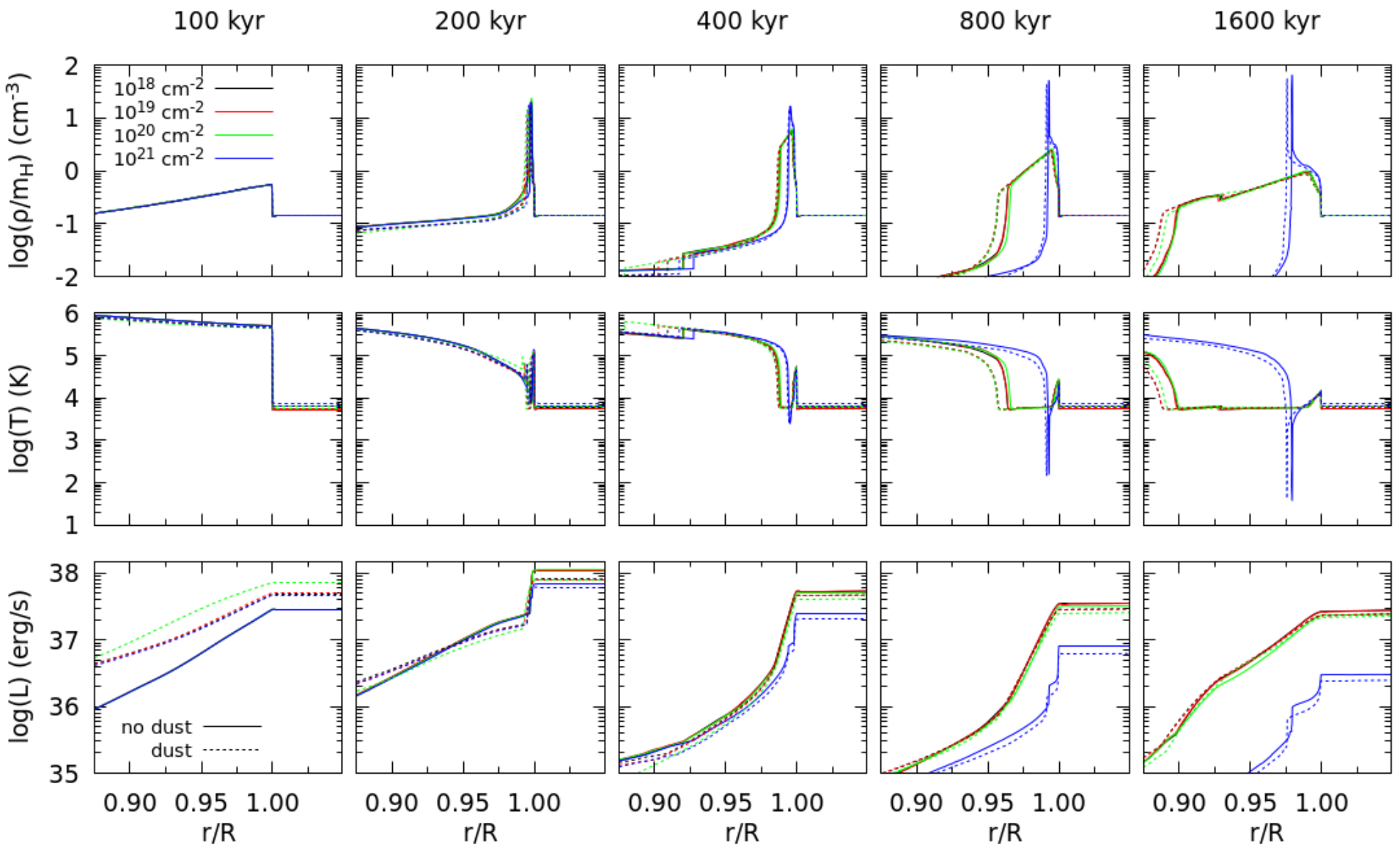

Figure 3.10: Integrated radial profiles of mass density, temperature, and luminosity normalized to the shock radius (i.e.: 1 is R) for particular time outputs for all SNR simulations with $n_{H,0} = 0.1\,\mathrm{cm}^{-3}$. Each color represent a column density. This figure was originally shown in Romero et al. (2021).

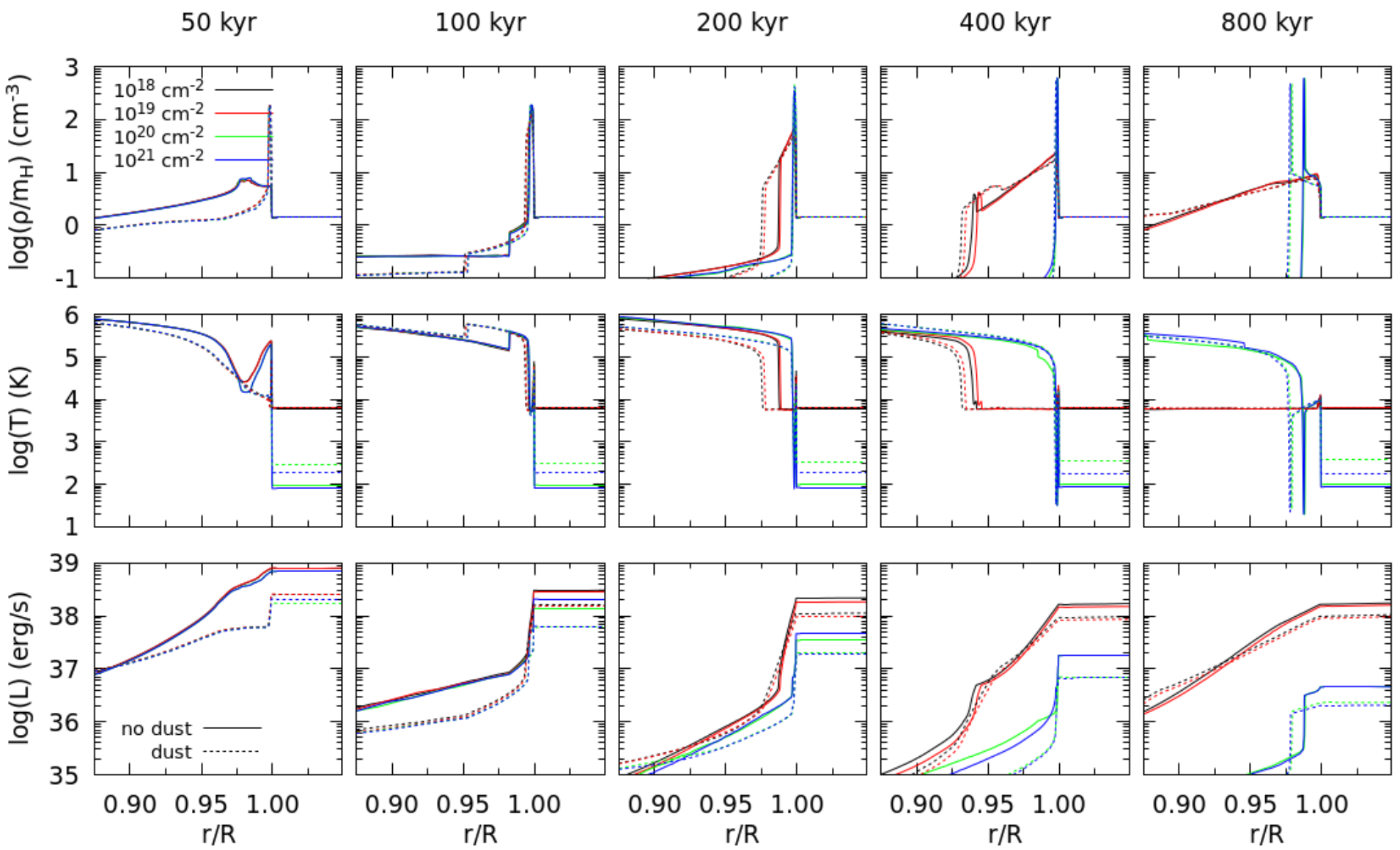

Figure 3.11: Same as Figure 3.10, but with $n_{H,0} = 1\,\mathrm{cm}^{-3}$. This figure was originally shown in Romero et al. (2021)

3.2.2.4 Limitations of this analysis

This exercise was meant to illustrate the effects of an external radiation field. In a true astrophysical context, this approach has its shortcomings and limitations. In addition to the restrictions made to the ISM at the beginning of section 3.2.1, there are other caveats related to the average radiation field approximation and the assumption of spherical symmetry.

Starting with the former, the SNR shell is prone to instabilities that distorts its shape, and cannot be followed by one-dimensional simulation. According to the analytical calculation of Vishniac and Ryu (1989), verified by the numerical results of Blondin et al. (1998), a realistic isothermal shock would be unstable at any Mach number higher than ~ 3 if the post-shock gas cannot cool below the ambient temperature, as in our unshielded conditions. On the other hand, Pittard et al. (2005) found that this limit drops to lower Mach numbers if the gas is allowed to cool further, as in our shielded case. The distinction between both regimes is thus important in this particular context.

Next, it should be noted that these calculations were made under the assumption of ionization equilibrium. Non-equilibrium effects reduce the cooling function, from a factor of 2 up to an order of magnitude, for temperatures lower than 10^6 K (Gnat and Sternberg, 2007; Vasiliev, 2013), although these differences may be overestimated in presence of an extragalactic background (Oppenheimer and Schaye, 2013). The recent work by Sarkar et al. (2021) studied this particular issue finding that, furthermore, at the shell formation time, when the temperature drops below 10^6 K, the cooling function increases compared with those in ionization equilibrium (see their Figure 5). These differences have a negligible effect into the dynamics and energetics of the SNR, but they cannot be neglected for predicting observable quantities, such as emission spectra.

If individual sources of radiation (i.e. stars close to the SN) were to be included, on-the-fly radiative transfer would be necessary. Even in the spherically symmetric case, the assumption of an average radiation field would not hold anymore, as the radiation field would vary as a function of both position and time. In addition, nearby stars would also enter the hot interior of the SNR as it increases in size, and their (almost unattenuated) radiation would reach the inner interface of the shell, potentially altering its morphology in the shielded scenario, which would cease to be valid.

On the other hand, unshielded SNR are more robust with respect to the details of the individual sources of radiation, as the whole medium is assumed to be optically thin, but they are prone to self-shielding of the shell, which can potentially become opaque. According to Figure 3.6, this transition occurs around $N_{H,thick} \sim 2 \cdot 10^{20}$ cm^{-2} for $n_{H,0} = 0.1\,\mathrm{cm}^{-3}$ and $N_{H,thick} \sim 3 \cdot 10^{19}\,\mathrm{cm}^{-2}$ for $n_{H,0} = 1\,\mathrm{cm}^{-3}$. We can make a rough estimation of the associated SNR radius R_{thick} at the time of the transition by assuming that all the swept-up mass is concentrated inside an infinitely thin shell, $N_{H,thick} \sim \frac{n_{H,0}}{3} R_{thick}$. This yields $R_{thick} \sim 2\,\mathrm{kpc}$ for $n_{H,0} = 0.1$ cm^{-3} and $R_{thick} \sim 30$ pc for $n_{H,0} = 1$ cm^{-3}. Thus, full radiative transfer, including absorption within the shell, should be taken into account when modelling a SNR with an unshielded ERF propagating in a dense medium.

One may extend the procedure presented in section 3.2.1.1 to less idealized environments by taking into account that the incident radiation field will vary across the simulation box along the evolution of the SNR. Rather than fully solving radiative transport, it should be possible to devise a fast algorithm that uses the column density towards individual sources to identify localized shielded and unshielded regions, neglecting the narrow transition (see Figure 3.6) between the two cases. Average radiation fields, as well as cooling and heating functions, could then be estimated within each region from previously computed tables.

3.2.2.5 Implications

The main result of the present work is that the most relevant effect of an ERF is to set the heating and cooling functions, and thus the conditions of the ambient medium where the SNR propagates. Broadly speaking, these numerical experiments can be classified in two different scenarios, dubbed as shielded and unshielded cases, separated by a hydrogen column density around $N_{H,eff} \sim 10^{20}\,\mathrm{cm}^{-2}$, albeit there is some dependence with the ISM number density (see Figures 3.5 and 3.6). The evolution of the main global properties of the SNR is fairly robust and does not depend strongly on the details of the radiation field, with the only exception of the total luminosity, which may vary by more than an order of magnitude. Moreover, our results also show that the internal structure of the shell is very different in the shielded and unshielded cases.

Observationally, these differences arise at very late times, of the order of $\sim 0.3-3\,\mathrm{Myr}$ after explosion, where detecting SNR is challenging. Surveys based on X-rays (e.g. Long et al., 2010; Leonidaki et al., 2010; Sasaki et al., 2012) are better suited to trace the earliest stages of SNR evolution, whereas the latter phases of the radiative shells are more readily observed in the optical (e.g. Lee and Lee, 2014a,b) or radio (e.g. Green, 2014; Dubner and Giacani, 2015) bands. Very old SNR have interacted so much with the inhomogeneous environment that only fragments of the shell may be observed. There are some individual objects reported as probable candidates for very old SNR, such as e.g. G55.0+0.3 (Matthews et al., 1998), G106.3+2.7 (Pineault and Joncas, 2000), FVW172.8+1.5 (Kang et al., 2012) or GSH 90-28-17 (Xiao and Zhu, 2014). All of them display average radii

between 50 and 100 pc, consistent with our results, and show obvious signs of fragmentation. With the exception of G106.3+2.7, they retain an approximately circular or elliptical shape on large scales.

These results suggest that the ERF has an important role in setting the overall luminosity of the remnants, especially in the optical and infrared regime. Besides the temperature structure of the shell, the ionisation and population balance of the gas is also set by radiative equilibrium (hence the effect on the cooling function), and therefore not only the luminosity but also the optical and infrared (e.g. Reach et al., 2006) emission line ratios will be different in the unshielded and shielded shells.

Furthermore, the distinction between the shielded and unshielded scenarios may have implications regarding supernova feedback, even if the energy and momentum injection into the ISM are not significantly affected. Specifically, the interaction of SNR with molecular clouds and star formation has been extensively studied under different conditions and strategies (e.g. Iffrig and Hennebelle, 2015; Korolev et al., 2015; Körtgen et al., 2016; Lucas et al., 2020; Lu et al., 2020, and references therein) and it is still an open problem. In general terms, shocks propagating through a low-density medium (or channel) will be able to propagate far away from the original place of the explosion, whereas dense media will be more resilient to shock passage. Albeit these results are robust with respect to an external radiation field, the physical state of the post-shocked gas is radically different in the warm ($T \sim 10^4$ K) thick shell of an unshielded SNR and its cold ($T \sim 100$ K) dense counterpart.

3.3 Supernova remnant evolution at extreme environments

We have found that, in the Solar Neighborhood, the external radiation field can alter the internal structure of the SNR but not the temporal evolution, except SNR luminosity.

Is this still true outside those conditions? The answer is no. The SNR evolution in low-density media, as commented in 3.2.1, fails to become radiative before disappearing, and the shock radius accelerates from the Sedov-Taylor solution because the ISM swept-up energy begins to be relevant for the evolution, as we saw in previous chapter. However, the heating of the gas due to radiation field is not well known outside our Solar Neighborhood, and more types of SNR may exist there, displaying a different evolution and feedback than radiative and low-density SNR.

In this section, posed as an academic exercise, I explore with SNR simulations all theoretical possibilities regarding the ambient density, pressure and also the net energy gain/loss due to radiation.

3.3.1 Initial conditions and SNR scenarios

I run multiple simulations for a different set of initial conditions with a range of ambient densities $\frac{\rho_0}{m_H} = \{10^{-2}, 10^{-1.5}, 10^{-1}, 10^{-0.5}, 1, 10^{0.5}, 10, 10^{1.5}, 10^2\}$ cm^{-3}, and a range of pressures $\frac{P_0}{k_B} = \{10^4, 10^{4.5}, 10^5, 10^{5.5}, 10^6\}$ K/cm^3, all of them with metallicity $Z = 0.02$. This yields a total of 45 simulations. Resolution of each run is 26000 cells in a simulation box of radius $8 \cdot 10^{20}$ cm (≈ 260 pc). At $t = 0$, the closest 100 cells to the center follow the same energy and entropy injection (3.44)-(3.45) as section 3.2.2.

Unlike the methodology done in 3.2.1, the cooling function is based on the one given by Grackle chemistry and cooling library (Smith et al., 2017) in their equilibrium mode. This is displayed in Figure 3.12 for reference. The Grackle cooling function, when compared with the upper panel of Figure 3.7, is similar to an unshielded case for $T > 10^4$ K but is closer to shielded behaviour for lower temperatures.

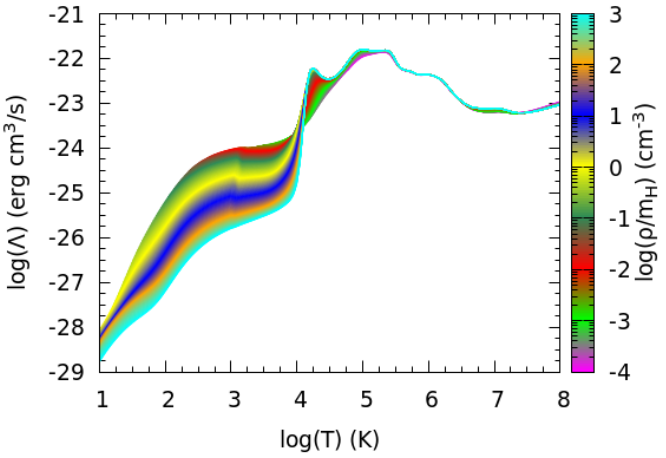

Figure 3.12: Cooling function ($\Lambda = (\frac{\mu m_H}{\rho})^2 \dot{u}_C$) obtained from the Grackle library (Smith et al., 2017).

Heating is not given by Grackle and, for this exercise, it is assumed to balance radiative cooling in the surrounding ambient

$$\dot{u}_H = (\frac{\rho}{\rho_0})\dot{u}_{C,0} \tag{3.50}$$

The choice of this heating is due to its convenience. First, as stated above, it prevents the environment from cooling at some ambient temperature $T_0 \sim (\frac{P_0}{k_B})(\frac{\rho_0}{m_H})^{-1}$ without switching cooling off. This gives a range of ambient temperatures between 10^2 and 10^8 K. Second, a fixed heating according to cooling at T_0 allows to study four possible SNR evolutionary paths:

1. **Radiative** cases, where $T_0 \lesssim 10^4$ K. Heating cannot compensate radiative cooling of the SNR, which have higher temperatures until the SNR ends the Sedov-Taylor phase.

2. **Heated** cases, where $T_0 \sim 10^{5.5}$ K at the peak of the cooling function in Figure 3.12. In this case, Cooling is inefficient and thus it cannot be higher than heating.

3. **Critical** cases, with temperatures near the cooling function peak. In this situation, cooling is more prevalent than heating but the latter is not negligible compared with the radiative cases.

4. **Adiabatic** cases, when $T_0 \gtrsim 10^6$ K. In this scenario, cooling, an so heating, are negligible because the shock front dies before becoming radiative, following the evolution of Tang and Wang (2005).

The main criticism of this heating is that we are not sure if it can truly exist in astrophysical context. On one hand, it is a good approximation for higher and lower temperatures, as it resembles the classical SNR evolutionary path for radiative cases and the non-radiative evolution for adiabatic SNR. On the other hand, critical and heated cases may resemble environments where heating prevents cooling for temperatures higher than 10^4 K due to a quasar irradiating its own halo (Sazonov et al., 2005; Gnedin and Hollon, 2012), or in galaxies at high redshifts (Ceverino et al., 2014), but that they be as important as to alter the SNR evolution is yet uncertain.

In any case, it still provides a valuable insight on the outcome of a supernova explosion in the hypothetical case where heating in the SNR evolution may be more important than cooling. Furthermore, it also motivates the development of tools (see chapter 4) to build heating rates from realistic astrophysical contexts.

3.3.2 Radius, energy, momentum and luminosity

Figures 3.13 and 3.14 display the shock radius, energy, momentum and luminosity as function of time, like I did for Figure 3.9 in previous section. Each panel represents a different initial ambient condition, labelled with the pair (ρ_0, P_0).

Energy in Figure 3.13 differs from the definition done in (3.46) and plotted in Figure 3.9. Here, I subtract the swept-up energy by the SNR as

$$\Delta E = E(t) - \frac{P_0}{(\gamma - 1)} \frac{4\pi}{3} R^3(t) \tag{3.51}$$

Second term is not significant for the analysis of radiative SNR because it dies before being higher than E_0, which is never the case for the remaining cases.Furthermore, ΔE represents the energy that remains from E_0 plus the energy gained by radiation.

Radiative cases, with a blue background in Figures 3.13 and 3.14, reproduces the same results found in the literature for both 1D (e.g.: Cioffi et al., 1988; Thornton et al., 1998) and 3D simulations (e.g. Walch and Naab, 2015; Kim and Ostriker, 2015; Li et al., 2015), as well as the shielded SNR cases of previous sections. The properties of these SNR are the constant momentum injection into the ISM and the clear peak in luminosity that signals the start of the radiative phases in energy, showing losses due to radiation; and shock radius, which have a slope change at the time of the luminosity peak.

Adiabatic SNR are painted with a white background in Figures 3.13 and 3.14. Luminosity of these SNR are, in general, negligible for the energy, which shows a horizontal line. This result supports the SNR described by Tang and Wang (2005) and Dorfi and Voelk (1996), which does not consider radiative cooling in their simulations. On the other hand, this means that the ISM will receive the full E_0 energy. In fact, it would be a very effective mechanism of quenching star formation in the surroundings of the SNR.

For the other two scenarios heating plays an important role. Critical cases, with a green background in Figures 3.13 and 3.14, cooling is still important and thus they show some features of radiative SNR such as the luminosity peak. However, momentum is no longer constant after that and energy loses are not so pronounced.

Finally, red panels in Figures 3.13 and 3.14 show heated SNR. In this case, all magnitudes increases catastrophically due to inefficient cooling. Formally, these shocks would never die, would increase their velocity due to energy gain, and reach any simulation boundary. Actually, heated shocks die due to multiple reasons, as they will reach a region where heating is not as efficient compared to cooling, or they may fail condition (3.40) before they accelerate. In any case, they would have a much stronger impact than their adiabatic counterparts. Therefore, should just only one of these SNR occur, no matter how unlikely they may be, then all subsequent analysis will be dictated by this single event.

3.3.3 Quantitative analysis of the SNR outcome

In Chapter 2 I presented the parameter ε_{sw} in (2.23) to discriminate between radiative and adiabatic cases. However, that parameter does not include the effects of heating into the SNR evolution. To solve that, I estimate

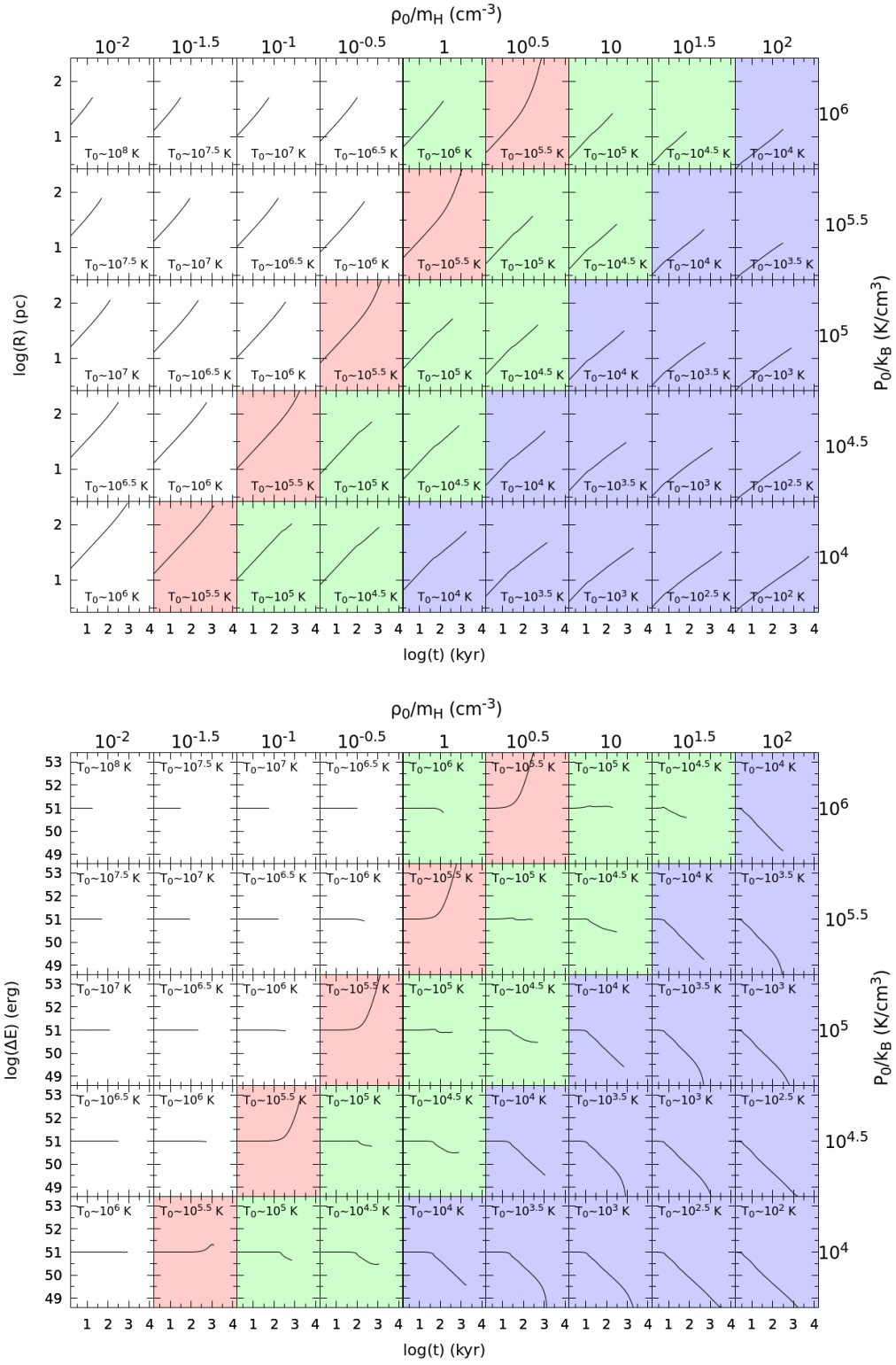

Figure 3.13: Shock radius (upper panel) and injected energy (lower panel, eq. 3.51) of all simulations as function of ambient density and pressure. Blue, red, green and white backgrounds represent SNR that are radiative, heated, critical and adiabatic, respectively.

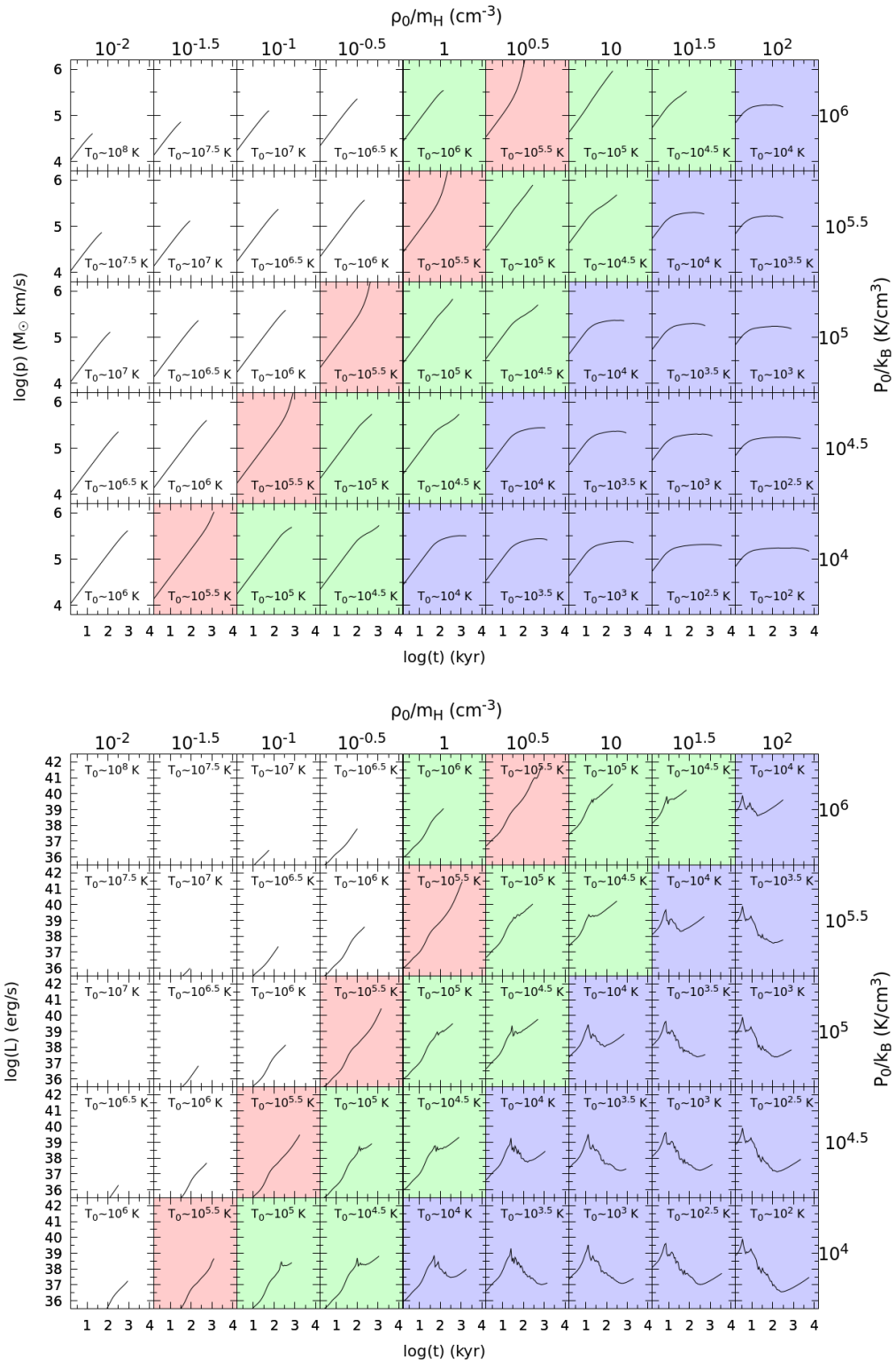

Figure 3.14: Same as Figure 3.13, but showing momentum (upper panel) and luminosity (lower panel).

the conditions that will eventually lead to each scenario, so we can compare the cooling/heating time scales with the expected life time of the remnant through a dimensionless parameter β which we define as:

$$\beta \equiv \frac{\dot{u}}{u} t_S, \tag{3.52}$$

where $u = \frac{P}{(\gamma-1)}$ denotes the thermal energy density, $\dot{u} = \dot{u}_H - \dot{u}_C$ is its associated loss/gain, in contrast with ε_{sw} that only considers cooling through t_Λ. Lastly, t_S is the time it takes a Sedov blast wave to reach $\mathcal{M} = 1$

$$t_S = (\frac{2}{5})^{\frac{5}{3}} (\chi E_0)^{\frac{1}{3}} \ (\gamma P_0)^{-\frac{5}{6}} \ \rho_0^{\frac{1}{2}}, \tag{3.53}$$

where $\chi \approx 2$. Equation (3.53) comes from reverting Sedov-Taylor velocity (2.8), and assuming that v_s is equal to the ambient sound speed $c_{s,0} = \sqrt{\frac{\gamma P_0}{\rho_0}}$.

The parameter β can take a very negative value if the cooling time of the SNR, included in $\dot{u}$, is less than t_S, and can take as well a very small value when the SNR outcome is not radiative. Furthermore, if there are heating processes included in $\dot{u}$, the sign of β may also be positive, opening the possibility of studying SNR in which heating may play a role.

In order to predict the outcome it is needed to find a relationship between the initial conditions and anything related to SNR, and evaluate β for these values. In that regard, one can obtain β evaluated just behind the shock front, or post-shock conditions, with the help of the Rankine-Hugoniot relations (see appendix B.1).

Looking at the sign and value of all possible post-shock β (hereinafter β_1), the four theoretical cases are:

1. If $|\beta_1| < 1$ for all times, the SNR outcome is adiabatic, as $t_S(1)$ is much smaller than $\frac{u_1}{\dot{u}_1}$.
2. If $\beta_1 < 0$ for all times and the previous condition is not fulfilled (i.e. $\beta_1 < -1$) at some point, then SNR outcome is radiative.
3. If $\beta_1 \geq 0$ at all times, with $\beta_1 > 1$ at any moment, then the SNR becomes heated, in which heating plays an important role whereas cooling is negligible.
4. If none of the above is fulfilled, the SNR outcome is critical, where both cooling and heating are important processes to consider.

This analysis allows to know the outcome of the SNR without running any simulation as long as cooling and heating are known, which can avoid a computationally expensive simulation, in particular for 3D ones.

Figure 3.15 shows one way to interpret β. There, I plotted a map of β as function of (ρ, P) for each initial ambient condition, labelled with the pair (ρ_0, P_0). The map is colored with warm and cold colors for positive and negative values of β, respectively. Moreover, there two warm (cold) colors to represent $|\beta| > 1$ and vice-versa. On the map, there is a solid line that represent the values of β_1. That is, those (ρ, P) values that can be at the SNR shock front (i.e.: post-shock values of the ambient).

From here, you only have to look what colors the black line go through.

1. If the line crosses only yellow and grey areas, it means that $|\beta_1| < 1$ and the SNR is adiabatic. That happens when $T_0 > 10^6$ K and $\frac{P_0}{k_B} \neq 10^6$ K/cm^3.
2. When the line traverses grey and cyan areas, then β_1 is always negative and there is a point where $\beta_1 < -1$. Therefore, the SNR is radiative and it happens when $T_0 \leq 10^4$ K.
3. If the opposite happens and the line crosses yellow and magenta areas, the SNR is heated, and only occurs when $T_0 \sim 10^{5.5}$ K.
4. Finally, if the line crosses three or more colors, then the SNR is critical.

Comparing Figure 3.15 with Figures 3.13 and 3.14, we can see that β_1 line can predict the outcome of each SNR. In contrast with ε_{sw} which only considers radiative cooling, β is more prepared for SNR outside solar neighborhood, where heating may be relevant.

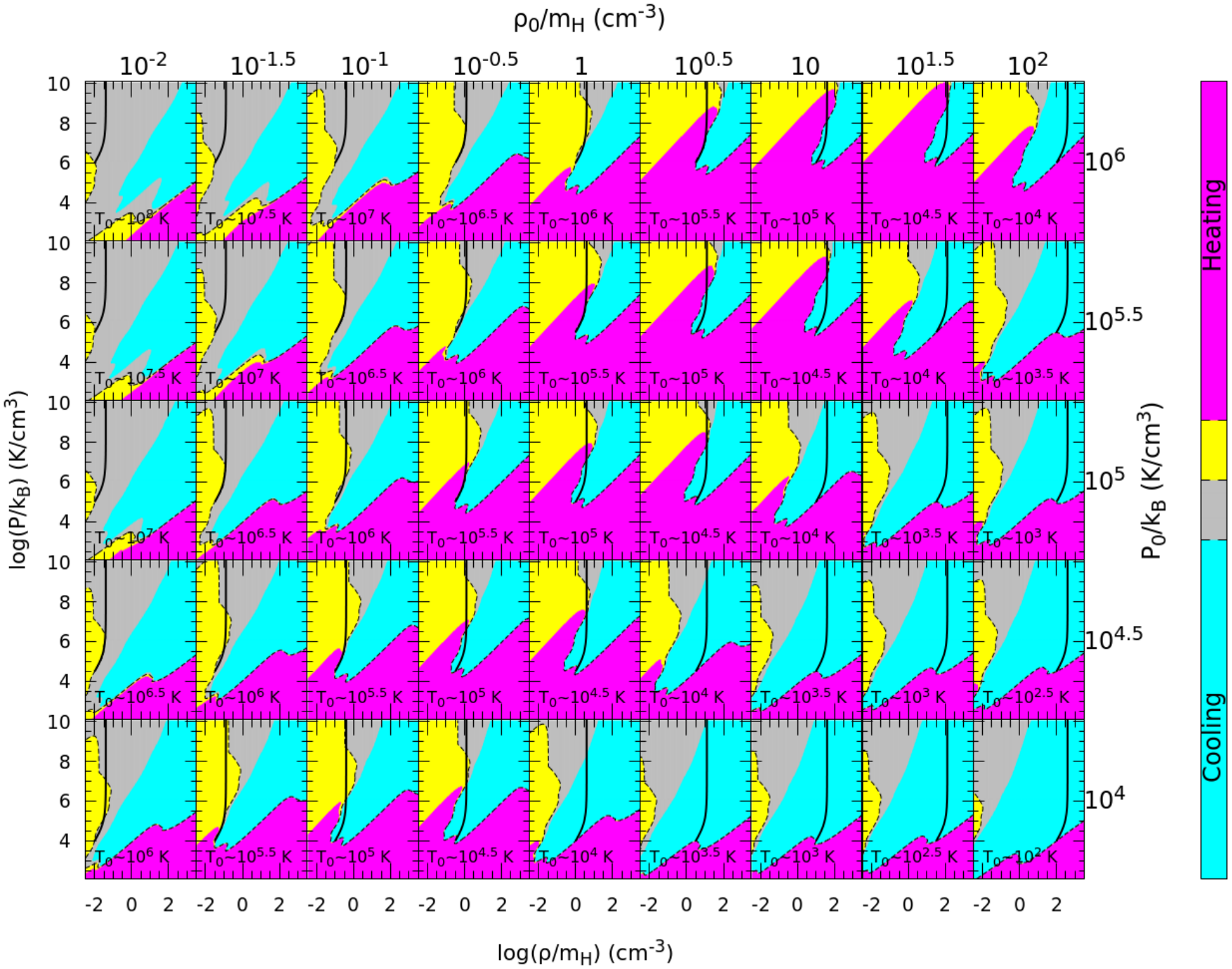

Figure 3.15: Sign and value of β as function of ambient density and pressure. The value $\beta = 0$ is represented as a dashed line. Post-shock values of the ambient, β_1, are plotted as a solid line and represent the SNR evolution (see 3.3.3).

Chapter 4

The Interstellar Radiation Field from a Distribution of Stars, Gas and Dust

This chapter is based on the paper:
"Predicting interstellar radiation fields from chemical evolution models"
by M. Romero, P. Corcho-Caballero, I. Millán-Irigoyen, M. Mollá and Y. Ascasibar
Submitted to MNRAS. arXiv:2203.04782 (2022)

4.1 Modelling an external radiation field self-consistently

In previous chapter, I showed how the internal structure of SNR changes due to the effect of an ERF. The approach taken there is to precompute the cooling and heating rates from a default mean intensity field given by Cloudy, `table ism`. In this context, the ERF is just the interstellar radiation field (ISRF) of the solar neighborhood. What can we do for other ISRF, which definitely will have a different share of stars, gas and dust?

For the Milky Way Galaxy (MWG), the ISRF has been computed long time ago (Habing, 1968; Mathis et al., 1983; Black, 1987), and there are some recent models nowadays (e.g.: Porter and Strong, 2005; Popescu et al., 2017; Natale et al., 2022). All these works have a phenomenological approach. That is, these models calibrate directly with observations.

In addition, the ISRF as ingredient is not as prevalent in the literature. There are some applications such as: modelling cosmic-rays transfer within the Galaxy (Evoli et al., 2017; Porter et al., 2017), predict the star formation rate (SFR) in Galaxies (Natale et al., 2022), as well as altering the shell structure in SNR as I showed in the last chapter (see also Romero et al., 2021).

In this chapter, I focus on producing an ISRF from chemical evolution models (CEM). CEM track the evolution of different chemical species within a galaxy, as well as the total stellar mass and its star formation rate (SFR). From their results, distributions of gas, stars and dust are obtained, which can be used to compute an ISRF. Stars can be used to predict the stellar population emission of the ISRF while gas and dust can be used to predict an emissivity and opacity, following the processes described in 1.2.1 and 1.2.2.

4.1.1 Mixing Cloudy and Skirt

Here I introduce the code Mixclask (**Mix**ing **Cl**oudy **a**nd **Sk**irt). As the name implies, this code combines the photoionization code Cloudy (last described in Ferland et al., 2017) with the monte-carlo radiative transfer code Skirt (Baes et al., 2003; Camps and Baes, 2020). Mixclask has its own Github repository[1].

For this section, I explain the main aspects of Mixclask. To begin with, I would like to explain the reasons that lead me to mix both codes

1. **Physical**: Radiation fields have to be considered as a parameter somehow to handle gas cooling (Gnedin and Hollon, 2012), in contrast with the usual CIE approximation that avoids its treatment.

2. **Efficiency**: To make a detailed model of how radiation affects gas in the ISM, you have to include radiative transfer in your work, which is easier said than done. From this point, you have two main choices: Do it yourself or use available codes in the literature. First option, when done right, is the most versatile option but it may take several years to yield results (an attempt was made, though, see appendix D), whereas the second option is the fastest but comes with the limitations of the chosen code. The latter option

[1] https://github.com/MarioRomeroC/Mixclask

Notation	Description	Mathematical definition
	Chemical composition and abundances	
ISM	Mixture of gas and dust.	
M	Total ISM mass.	$M = M_{gas} + M_{dust}$
ρ	Mass density	
n_H	Hydrogen Number density.	
X_i	Mass fraction of element i relative to gas.	M_i/M_{gas}
Z	Metallicity	$\sum_{i \geq Li} X_i$
N_i	Column number density of element i.	
A_i	Mass number of element i.	
Dust	Mixture of grains and PAH.	
DTG	Dust-to-gas ratio	M_{dust}/M_{gas}
q_{PAH}	PAH-to-dust ratio	M_{PAH}/M_{dust}
	Radiative transfer magnitudes	
λ	Wavelength.	
I_λ	Energy per unit of time, area, wavelength and solid angle.	
j_λ	Emitted energy per unit of time, volume, wavelength and solid angle.	
τ_λ	Optical depth	
κ_λ	Extinction mass coefficient.	See (4.6)
ϖ_λ	Albedo.	$\tau_\lambda^{(scattering)}/\tau_\lambda$
$4\pi\lambda J_\lambda$	Mean intensity field, averaged to solid angle.	$\lambda \int I_\lambda d\Omega$
λL_λ	Neutral luminosity (radiated energy per unit of time).	$\lambda \int j_\lambda dV d\Omega$
	Geometry	
domain	The whole simulated physical volume	
region	Subdivision of the simulation domain, it contains either stellar or ISM material.	
$\{R, z\}$	Cylindrical coordinates	
$\{x, y, z\}$	Cartesian coordinates	
ring geometry	Assumes a ring of radius R_0, width w and height h, with density proportional to	$\exp[-\frac{(R-R_0)^2}{2w^2}] \exp[-\frac{\lvert z \rvert}{h}]$
shell geometry	Assumes a spherical shell with constant density between R_{in} and R_{out}	
point geometry	Assumes a point source located in (x_0, y_0, z_0). Only available for stellar regions.	

Table 4.1: Summary of relevant magnitudes and definitions (in **bold**) used thorough this chapter.

was chosen because it was a good opportunity to learn SKIRT, as it is a monte-carlo radiative-transfer technique in contrast with CLOUDY and the code of appendix D.

3. **Code synergy**: It is possible to combine results of several codes to improve results of a single one, and to increase their predictive power. In that regard, CLOUDY excels in computing the gas quantities related to radiation fields, such as emission spectra, cooling functions, ionization fractions, etc; but it limited to 1D. On the other hand, SKIRT does 3D radiative transfer for defined regions of stars and dust, but the gas is not fully included in it (at least at the moment of writing this work), which is an obligatory element when studying SNR or CEM.

All quantities defined in MIXCLASK are in Table 4.1 and the flow of the code is shown in Figure 4.1. MIXCLASK is a `python` code that reads an input given by the user and calls CLOUDY and SKIRT to produce a map of the radiation field. In the code, the simulation domain is subdivided in several regions, defined by the user, of stars and ISM material (gas and dust) separately. The main output of MIXCLASK is the mean intensity field at desired positions inside the physical domain. Mean intensity field is taken from is usual definition (1.3), multiplied by wavelength:

$$4\pi\lambda J_\lambda = \lambda \int I_\lambda d\Omega, \tag{4.1}$$

where I_λ is the radiative energy per unit of time, area, solid angle and wavelength (1.1). From now on, I will explain each step done by MIXCLASK.

4.1.1.1 The configuration input files

The user has to provide three configuration files as input. The first two are the needed magnitudes to initialize the stellar and ISM regions, and the third one are the locations, in Cartesian coordinates, where the mean intensity will be saved. Each file must have a header, in which each row starts with #, explaining what parameter is shown in each column. After the header, each row represent a different region, in the case of stellar and ISM input files, or positions for the output locations.

Stellar configuration file is the easiest to fill, as it only needs two inputs. Below there is an example:

```
# Column 1 : SedFile
# Column 2 : Geometry ['type',params](pc)
file1.stab ['point',0.0,0.0,0.0]
file2.stab ['ring',1.0,0.1,0.2]
file3.stab ['shell',2.0,3.0]
```

Here I defined three stellar regions. First one is a point source at the origin; second one a ring at 1.0 pc with width 0.1 pc and height of 0.2 pc; and a third stellar region consisting of a shell between 2.0 and 3.0 pc. First column is a filename, ending in *.stab*, that contains the neutral luminosity, λL_λ, of that region as function of wavelength.

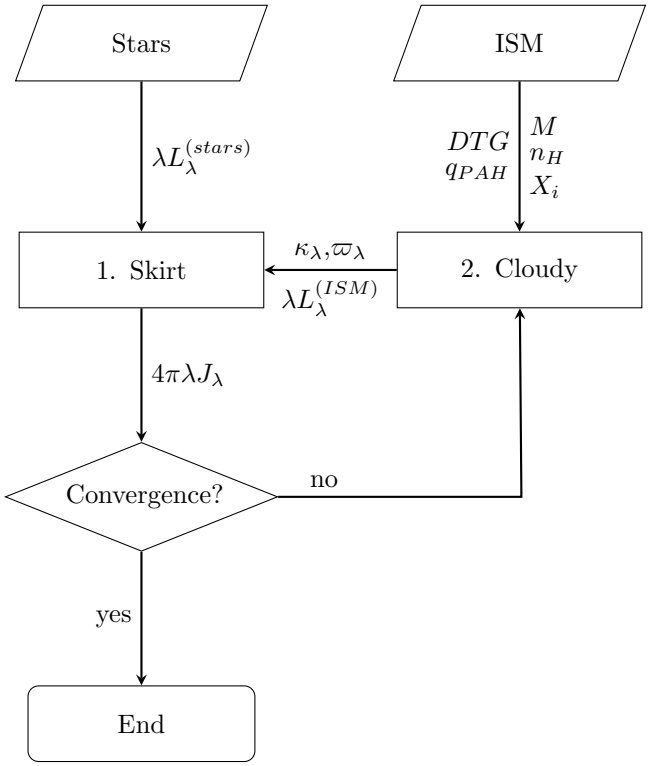

Figure 4.1: Flowchart summarizing all processes done by MIXCLASK. Stellar spectra and ISM composition (i.e.: gas and dust) are used as inputs, and it predicts the mean intensity of the simulation domain when convergence is achieved (see text). Adapted from Romero et al. (2022).

The ISM configuration file follows the same criterion, but it needs far more parameters than the previous one, while other are optional. The mandatory parameters are the file name that contains the output, the mean intensity $4\pi\lambda J_\lambda$, of that region; the ISM mass, M; the Hydrogen number density, n_H; and the geometry of the region, defined as a `python list` like in the stellar file. From here, the user is allowed to have some flexibility for the chemical composition of the ISM. On one hand, the user can give any mass fraction he wants, as long as is relative to ISM mass, and elements between Helium to Zinc, because CLOUDY cannot handle heavier elements. Each element adds a column in the input file, and will overwrite the default values used (By default, used abundances are from Grevesse et al., 2010, see also appendix A). An alternative is to give the total gas metallicity, Z, instead. In both cases, Helium mass fraction have to be provided by the user. On the other hand, dust in the ISM is parameterized with the dust-to-gas ratio, DTG, and the pah-to-dust ratio, q_{PAH}.

The last configuration file contains a header that denotes the Cartesian coordinate of the column. This is the same input file required in SKIRT for saving the mean intensity field of a simulation[2].

Finally, there are other options that the user can configure inside the `main.py` file, such as the wavelength range, resolution, and the convergence criterion, but these will be discussed in their respective sections.

Stellar and ISM input files are read at the beginning of the simulation, reading the header to know what magnitude is in that column, and then filling the data for each stellar/ISM region asked.

4.1.1.2 Skirt implementation

SKIRT (Baes et al., 2003, see also his home page[3]) is a monte-carlo radiative transfer code written in `C++` and `python`. It launches a large number of `photon packets` in the simulation domain that advance in a straight line until they interact with dust (i.e.: the photon is scattered or absorbed) or leaves the domain. The path taken and interactions of the `photon packets` are handled with probability distributions.

MIXCLASK uses the version 9 of SKIRT, described in Camps and Baes (2020). This version makes a distinction between a `source`, which models everything related with radiative emission, and a `medium`, which contains all properties about the material where photons are travelling. There are several options in SKIRT to define these, but I opted to provide text files for both. On one hand, `sources` need a file that contains the neutral luminosity

[2]See its documentation for more details: https://skirt.ugent.be/skirt9/class_radiation_field_at_positions_probe.html
[3]https://skirt.ugent.be/root/_landing.html

as function of wavelength. As normalization, MIXCLASK uses the value of λL_λ at a defined wavelength. These files are the `SedFile` of the stellar input files, and are structured as

```
# Column 1: Wavelength (nm)
# Column 2: Luminosity (erg/s)
# Normalization wavelength 550.0
# Value 1.172e+43
9.1 2.236e+37
...
```

following the same notation as SKIRT documentation[4].

On the other hand, a `medium` is also defined with a text file[5], created by MIXCLASK during execution (i.e.: no input from the user is needed). These files requires, as function of wavelength, the extinction mass coefficient, κ_λ, the albedo, ϖ_λ, and the scattering asymmetry parameter, which is set to 0. Normalization is set with total mass of the `medium`, which corresponds to the ISM mass of the region.

MIXCLASK translates regions into SKIRT `sources` and `media`. In particular, stellar regions are their own `sources` whose data is given by the user, whereas each ISM regions are divided in both a `source` and a `medium` defined by MIXCLASK before running SKIRT.

In order to execute SKIRT, a input `.ski` file that follows a `.xml` structure should be provided. MIXCLASK creates that file for the user during runtime. In that regard, all MIXCLASK internal parameters are converted into `python dictionaries` and then are written with a `.xml` structure. There are other options required in SKIRT that are not asked to the user in MIXCLASK are filled here as well. The SKIRT input file is configured in `expert` mode under `dust extinction only` to have the radiation field in the domain as output, and because CLOUDY performs ISM emission. All models shown here are run with 10^8 `photon packets` (although this can be changed inside the code), in the Local universe at redshift $z = 0$ with axisymmetric spatial grids. MIXCLASK is restricted to isotropic and non-polarized emission for all `sources`. The simulation domain is delimited with the farthest region, in terms of the coordinate origin, given in the user input. When regions are defined by shells, this code uses R_{out} to define the radial and vertical size of the simulation. In ring regions, on the other hand, distances $R_0 + w$ are used for the radial size, whereas for the vertical size, MIXCLASK uses h multiplied by a factor of 10, although this can be changed if the user desires. This factor is included in order to allow an output of the radiation field above the ring region, which is useful for studying astrophysical entities that can be modelled with a ring geometry, such as the mean intensity above a galactic disk.

4.1.1.3 Cloudy implementation

CLOUDY is a photoionization code that focuses on the microphysics of the ISM. It predicts several magnitudes of the diffuse ISM, such as temperature, chemical composition and ionization, etc. Nevertheless, MIXCLASK is only interested in the diffuse emission spectra that the ISM produces (i.e.: nebular or continuum emission). Here I used version 17.01 of CLOUDY, as described in Ferland et al. (2017) (see also his home page[6]).

CLOUDY always consider a cloud in 1D with several parameters that must be given in order to execute it properly. These parameters are the cloud chemical composition, its geometry and the radiation field that hits the cloud. CLOUDY is called per each ISM region, and their input files are generated by MIXCLASK for the user, as described below.

The chemical composition is provided by the user in MIXCLASK ISM input file. On one hand, the density n_H is mandatory to establish the Hydrogen number density of the ISM region. If the user does not give more data about other chemical elements, MIXCLASK will configure CLOUDY to use chemical abundances generated by the command `abundances gass`, which follows Grevesse et al. (2010) solar composition. These abundances are scaled with Z if given, and overwritten when the user gives custom abundances. For example, if the user gives only Carbon abundances, MIXCLASK will use `abundances gass` composition for all elements but Carbon, in which the value given is used instead. One important detail when giving custom abundances in CLOUDY is that it asks for the number of particles relative to Hydrogen, N_i/N_H, while MIXCLASK demands mass fractions X_i relative to ISM mass. The conversion between both is

$$\frac{N_i}{N_H} = \frac{X_i}{A_i X_H}, \tag{4.2}$$

where A_i denotes the mass number of each element i.

Dust is included as grains and PAH separately. Grains are added with `grains ism` scaled with $DTG \times (1 - q_{PAH})$ in order to consider only grains. Likewise, PAH uses `grains pah`, scaled with $DTG \times q_{PAH}$ to scale

[4] https://skirt.ugent.be/skirt9/class_file_s_e_d.html
[5] See its documentation for more details: https://skirt.ugent.be/skirt9/class_mean_file_dust_mix.html
[6] https://gitlab.nublado.org/cloudy/cloudy/-/wikis/home

with PAH only. To place PAH through the whole cloud, MIXCLASK includes the command `set pah constant` into CLOUDY input. For both dust types, values are scaled relative to their default abundances.

Default values of N_i/N_H, DTG and q_{PAH} are given in appendix A, and they may also be found in CLOUDY documentation (Hazy 1).

Since CLOUDY is restricted to 1D, each ISM region is approximated as a slab with half of the full width of that region. That is, each run starts at the middle radius of the region (R_0 and $\frac{1}{2}(R_{out} + R_{in})$ for ring and shell geometries, respectively), and ends when the depth of the CLOUDY cloud reaches w or $\frac{1}{2}(R_{out} - R_{in})$, depending on the region geometry. The default stop condition of CLOUDY, which is when the cloud reaches an equilibrium temperature, is disabled with `stop temperature off`.

As radiation field, MIXCLASK uses the mean intensity field given by SKIRT as output at the middle radius of the ISM region. This is added with `table sed` and `nuf(nu) ... at ...` to establish the sed file used and its normalization at a particular wavelength, respectively. There are other commands that are configured in the CLOUDY input file. First, MIXCLASK sets the `cosmic rays background` command to consider the presence of cosmic rays. In practice, this assumes an H^0 cosmic ray ionization rate of $2 \cdot 10^{-16}\,s^{-1}$ and $4.6 \cdot 10^{-16}\ s^{-1}$ for H_2 secondary ionization rate (see Glassgold and Langer, 1974; Indriolo et al., 2007).

Finally, MIXCLASK asks CLOUDY to provide the emission spectra of the cloud with `save continuum`, that returns $4\pi\lambda J_\lambda$ emitted by the ISM region among other spectra [7]. On the other hand, CLOUDY also returns the optical depths, τ_λ of the cloud with `save optical depth` command, and the gas number density of all elements with `save abundances`.

4.1.1.4 Iterative process and convergence

When MIXCLASK is executed, it performs a SKIRT run for the whole simulation domain first, using only stellar regions, to make a first estimate of $4\pi\lambda J_\lambda$. These results are recorded for the middle point of each ISM region and are used as the incident radiation field in CLOUDY.

Then, CLOUDY is run for each ISM region, approximated as a slab with half of the total depth of the region, and returns its emission spectra, $\tilde{J}_\lambda$, and optical depth, τ_λ. Likewise, the output is passed to SKIRT, for which it needs to be converted into the magnitudes required by SKIRT. As a first step, the emission spectra and optical depths are downsampled in order to meet SKIRT resolution. This is done by interpolating the integral of $\tilde{J}_\lambda$ and τ_λ. On one hand, MIXCLASK transforms the downsampled $4\pi\lambda\tilde{J}_\lambda$ to a neutral luminosity, defined from emissivity (i.e.: emitted energy per unit of time, volume, solid angle and wavelength) as:

$$\lambda L_\lambda = \lambda \int j_\lambda \, dV d\Omega, \tag{4.3}$$

which is the input magnitude required by SKIRT. This expression (4.3) is approximated by dividing the mean intensity by the depth of the cloud modelled in CLOUDY, s, and then multiplying by the volume V of the current region:

$$\lambda L_\lambda \approx \frac{4\pi\lambda\tilde{J}_\lambda \, V}{s} \cdot \frac{\tau_\lambda}{1 - e^{-\tau_\lambda}}, \tag{4.4}$$

where I have added a second quotient is a first-order correction that considers the absorption across the region if it is optically-thick (note that this fraction is unity for optically-thin media). The volume V, on the other hand, is computed from the ISM mass and density as $V = M/\rho$. This density, in turn, is computed from dust-to-gas ratio and the chemical gas abundances provided by CLOUDY for each region:

$$\rho = (1 + DTG) \sum_{i=H}^{Zn} A_i m_H n_i \tag{4.5}$$

where m_H is the Hydrogen mass, and n_i is the number density of element i.

From here, the ISM opacity is computed from τ_λ. MIXCLASK requires the extinction mass density, κ_λ, and albedo, ϖ_λ. κ_λ is computed with mass density:

$$\kappa_\lambda = \frac{\tau_\lambda}{\rho s}, \tag{4.6}$$

whereas the albedo is calculated as the ratio between the scattering optical depth, $\tau_\lambda^{(sca)}$ and τ_λ

$$\varpi_\lambda = \frac{\tau_\lambda^{(sca)}}{\tau_\lambda} \tag{4.7}$$

[7] Actually, the output of `save continuum` depends on the radiation field entered in CLOUDY. When a mean intensity is given without a distance to the radiative source, then `save continuum` returns $4\pi\lambda J_\lambda$. Otherwise, if the radiative source location is given to CLOUDY , it returns λL_λ instead. In CLOUDY documentation, these are referred as `intensity case` and `luminosity case`, respectively. MIXCLASK always works under `intensity case`, but an user should be careful when compared against standalone CLOUDY, as done for the test case 4.1.2

Commands	Comments
`# INPUT`	
`hden 0`	$\log(n_H)$.
`abundances gass`	See Table A.1 for more details.
`grains ism`	
`grains pah`	
`set pah constant`	
`cosmic rays background`	
`blackbody 3e4`	$T_{BB} = 3 \cdot 10^4\ K$
`luminosity 38.28 range 0.1 to 1e9 nm`	$\int_{0.1\ nm}^{10^9\ nm} L_\lambda\ d\lambda = 10^{38.28}\ erg/s \simeq 5 \cdot 10^4\ L_\odot$.
`stop temperature off`	
`iterate to convergence`	
`radius 10.0 parsec linear`	Beginning of the cloud.
`stop thickness 30.0 parsec linear`	Depth of the cloud (i.e.: cloud ends at 40 pc).
`# OUTPUT`	
`save continuum 'spectra_control.txt' last units nm`	Returns λL_λ

Table 4.2: Cloudy input file to generate the solution of the HII region.

Finally, Mixclask repeats the Skirt run, but this time with both stellar and ISM regions. The result is the mean intensity field, $4\pi\lambda J_\lambda$, of all defined regions, which can be used as a final output or as new estimate to repeat Cloudy runs.This process is iterated until convergence as illustrated in Figure 4.1. In order to check that, the condition:

$$|\langle \lambda J_{\lambda,\text{new}} - \lambda J_{\lambda,\text{old}} \rangle| \leq \epsilon \frac{|\langle \lambda J_{\lambda,\text{new}} + \lambda J_{\lambda,\text{old}} \rangle|}{2} \tag{4.8}$$

is evaluated at a series of specific wavelengths or wavelength intervals specified by the user. When an specific wavelength λ_0 is given, $\langle \lambda J_\lambda \rangle(\lambda_0)$ is just the mean intensity at that wavelength. For a wavelength interval (λ_0, λ_1), $\langle \lambda J_\lambda \rangle(\lambda_0)$ is the integral

$$\langle \lambda J_\lambda \rangle(\lambda_0, \lambda_1) = \int_{\lambda_0}^{\lambda_1} \lambda J_\lambda d\lambda. \tag{4.9}$$

For the rest of this chapter, Mixclask considers the intervals $(\lambda_0, \lambda_1) = (10, 90)\,\text{nm}$, with a tolerance of $\epsilon = 0.67$, and $(100, 300)\,\mu\text{m}$ to test gas absorption in the ultraviolet and far infrared ranges with $\epsilon = 0.10$ for thermal dust emission, respectively. UV tolerance, allowing errors up to a factor of 2, is much higher compared with IR because wavelengths lower than 91 nm are heavily absorbed, and hence the monte-carlo noise from Skirt becomes more significant. Nevertheless, these values are defaults that can be changed by the user if desired. The algorithm stops iterating when (4.8) is fulfilled by all the ISM regions in all the selected wavelength ranges, or when a specified maximum number of iterations (15 by default) has been reached to avoid the case that it is impossible to reach a selected tolerance due to monte-carlo noise (if that happens, Mixclask gives a warning about convergence when it finishes).

4.1.2 Test case: HII region

In order to check if Mixclask can predict correctly mean intensities, I designed a test where the results are compared against standalone Cloudy. This test consists on a Black-body of $3 \cdot 10^4$ K with a total luminosity of $5 \cdot 10^4\,\text{L}_\odot$, surrounded by a spherical ISM shell between 10 to 40 pc with an Hydrogen density of $1.0\,\text{cm}^{-3}$. This test can be interpreted as a main-sequence B star inside a HII region.

The input for standalone Cloudy is reproduced in Table 4.2. The simulation is set with the Black-body at $r = 0$ pc with a spherical cloud whose initial and outer radius are 10 and 30 pc, respectively. Standalone Cloudy performs its calculation between those two radius, and this simulation is repeated again until convergence by asking Cloudy to do so. Neither custom abundances nor dust are given as inputs, and therefore the default values of `abundances gass`, `grains ism` and `grains pah` (see Table A.1 for details) are used. An important detail of this Cloudy input is that it gives λL_λ as output, in contrast with Mixclask outputs as it returns $4\pi\lambda J_\lambda$. In order to recover mean intensities, I follow the section 2.6 of Hazy II of Cloudy documentation, and I divide λL_λ by $4\pi r^2$, being $r = 40$ pc, the distance between the Black-body and the outer radius of the shell.

In Mixclask, the spherical shell is divided in fifteen regions with 2 pc width each and the same chemical composition for all of them. As described in 4.1.1.3, I want to highlight that Mixclask asks Cloudy to solve plane-parallel slabs from the mean radiation field generated by Skirt in order to estimate ISM emission spectra and opacity in each iteration. That is, the shell geometry of the problem is considered by Skirt in

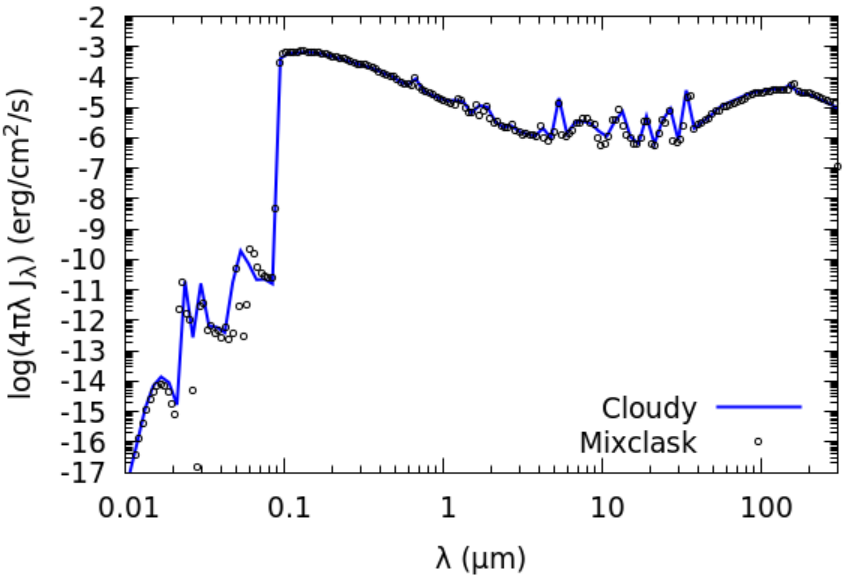

Figure 4.2: Predicted spectrum of a Black-body after its radiation traverses a spherical shell between 10 to 40 pc. CLOUDY transmitted continuum has been downsampled by interpolating the integral of J_λ to have the same resolution as MIXCLASK. This Figure is also shown in Romero et al. (2022).

MIXCLASK, which performs the radiative transfer calculations. The wavelength ranges from 0.01 to 300 μm in 200 logarithmic steps, and the default convergence criterion is used.

The result of this test is displayed in Figure 4.2, where $4\pi\lambda J_\lambda$ predicted by both codes are plotted. The spectrum shows three distinct ranges: a heavily absorbed region, due to the presence of gas, for energies below 13.6 eV ($\approx$ 91 nm); the incident Black-body spectrum; and the dust with PAH emission in the IR. The agreement between both codes is excellent for $\lambda > 91$ nm, and the main trend in the heavily absorbed region is very well followed despite the noise generated by SKIRT. Thus, this demonstrates that the scheme suggested in Figure 4.1 can successfully add gas into the radiative transfer of SKIRT while retaining dust emission if treated alongside gas.

4.2 The interstellar radiation field of the Milky Way Galaxy

Let me show an application of MIXCLASK in a scientific case. In particular, here I generate the Milky Way Galaxy (MWG) radiation field. As told at the beginning of this chapter, I am taking a very different approach. Instead of starting with calibrated data of stars and dust from observations (e.g.: Mathis et al., 1983; Porter and Strong, 2005; Popescu et al., 2017, an references therein), I am going to use Chemical Evolution Models (CEM) that generate the relevant abundances of stars, dust and also gas during the lifetime of the Galaxy.

In that regard, I consider two different CEM: MULCHEM (Mollá et al., 2022) and Millán-Irigoyen et al. (2020) (hereinafter MMA) models. Both models have different aims when they were developed, as I will describe below.

Figure 4.3 shows a flowchart of all processes needed before running MIXCLASK. A CEM gives the surface mass densities of gas, stars and, in the case of MMA model, dust; as well as the star formation rate (SFR) to track the formation of new stars. Before converting this output into MIXCLASK input, there are some steps to do first. ISM material (i.e.: gas and dust) is easier to translate into MIXCLASK input, while stellar data needs to be transformed into a stellar population luminosity. Next subsections explain these processes in more detail before showing the final results in 4.2.4.

4.2.1 Description of the selected Chemical Evolution Models

4.2.1.1 Mulchem model

MULCHEM (Mollá et al., 2017, 2022) assumes that the Galaxy is divided in two zones, halo and disk, with a total dynamical mass of $9.55 \cdot 10^{11}$ $M_\odot$. The mass is distributed following Salucci et al. (2007) equations, which give the rotation velocity curves for both components as well as their radial distributions. The initial mass is assumed to infall over the equatorial plane, forming a disk, with a rate inversely proportional to a collapse time scale $t_{infall}(R)$. This is calculated in that way that the mass in each radial region of the disk at the present

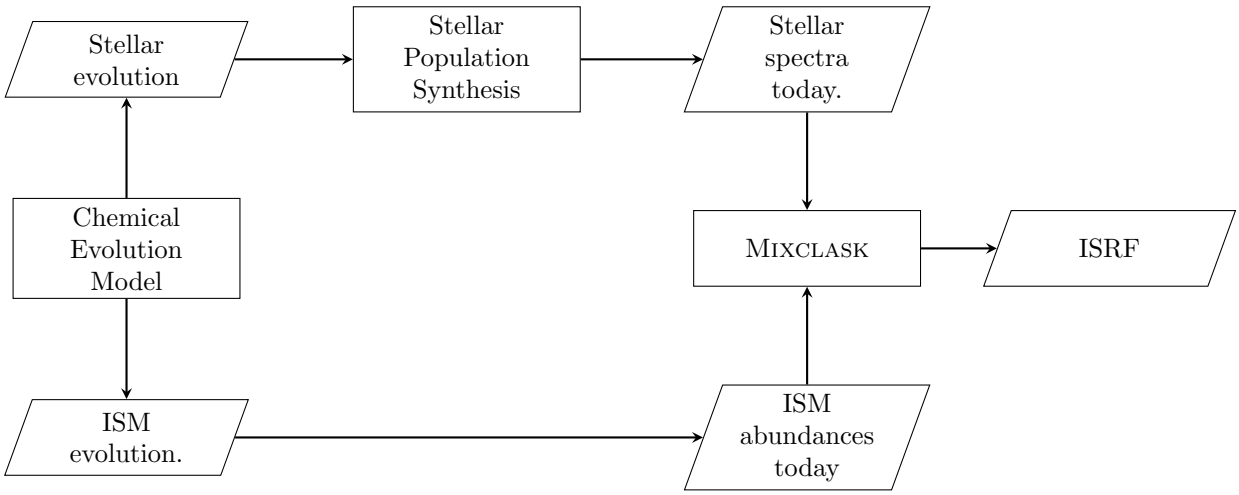

Figure 4.3: Necessary steps in order to use the output of a Chemical Evolution Model into an input for MIXCLASK .

time be the observed value (Mollá et al., 2016, see details in). The disk is divided in concentric rings with a height $h = 0.2\,\mathrm{kpc}$, located at a radius R with a width $w = 0.5\,\mathrm{kpc}$.

The star formation law in the Galactic disk regions takes places into two steps, first forming molecular clouds from the diffuse gas, then forming stars by cloud-cloud collisions. In the model computed for this particular work, both processes depends on free parameters or efficiencies selected to reproduce the radial distribution of diffuse gas, molecular cloud, and star formation surface densities. Elements appear in the interstellar medium as a consequence of their ejection by stellar winds, as planetary nebular or supernova explosions. The stellar yields used are those from Cristallo et al. (2011, 2015) and Limongi and Chieffi (2018) for low and intermediate mass stars and massive stars, respectively, and Iwamoto et al. (1999) for supernovae Ia yields.

The equation system, related with the change of mass from a phase to other along time, that the code solves is given in Mollá et al. (2017). The basic inputs of the model are the selected stellar yield sets, the Initial Mass function (IMF) used, Kroupa (2001) in this case, the chosen virial mass, that defines the infall rate, given above, and the efficiencies to form molecular gas and stars. As a result, the model gives the time evolution of the masses in form of ISM material (diffuse or molecular phases), stars (low and intermediate mass, massive ones and remnants), star formation rate, total mass in the disk zone, supernova –core collapse and SN-Ia types–rates and elemental abundances for 15 elements: H, ^{2}H, ^{3}He, ^{4}He, ^{12}C, ^{13}C, N, O, Ne, Mg, Si, S, Ca and Fe.

The MULCHEM model used is calibrated to reproduce the radial distributions of gas (for both phases, diffuse and molecular gas), stars and star formation rate, for the disk of MWG as the age-metallicity relation and the star formation history data of the Solar Vicinity. The evolution of the C, N and O abundances in this region, as the radial gradients of these same elements are also well fitted. The data used for this calibration are summarized in Mollá et al. (2015). See details in Mollá et al. (2022).

4.2.1.2 MMA model

MMA model, instead of following the abundances of specific elements in the ISM, tracks the gas phases (ionized, atomic and molecular) and cosmic dust grains separately. Dust is a critical ingredient in order to model correctly the ISRF in the IR (e.g.: Freudenreich, 1998; Robitaille et al., 2012; Natale et al., 2022), where its emission dominates. Furthermore, it also contributes to the absorption of starlight like diffuse gas, in which dust is considered a good tracer (Eales et al., 2012; Groves et al., 2015). Thus, it is crucial to implement the evolution of dust and the actual dust content of the MWG into CEM in order to reproduce the ISRF.

The MMA models have five variables: first three are free parameters that are needed for the modelization of dust (ζ,t_{dest} and $\mathrm{n_{cloud}}$). ζ is the sticking coefficient, i.e., the probability that an atom gets stuck to a grain when they collide, t_{dest} is the destruction timescale of dust grains, and $\mathrm{n_{cloud}}$ is the density of Giant Molecular Clouds. The other two parameters, Σ_{total} and t_{infall}, represent the total mass (stars and ISM material) and size of different regions of a galaxy, respectively. Specifically, Σ_{total} is the total surface density in the region at the end of the evolution, and t_{infall} is the parameter that regulate gas infall rate.

Originally, MMA models were created to reproduce galaxies as a whole. Instead, these models have been adapted in the present work to represent different disk regions in the Galaxy with the same $\{R, w, h\}$, as MULCHEM. In addition, dust physics parameters have been set to constant values of $\zeta = 0.7$, $t_{\mathrm{dest}} = 1.3\,\mathrm{Gyr}$ and $\mathrm{n_{cloud}} = 5000\,\mathrm{cm^{-3}}$ in order to be consistent with the results of Mollá et al. (2015). Variations are allowed

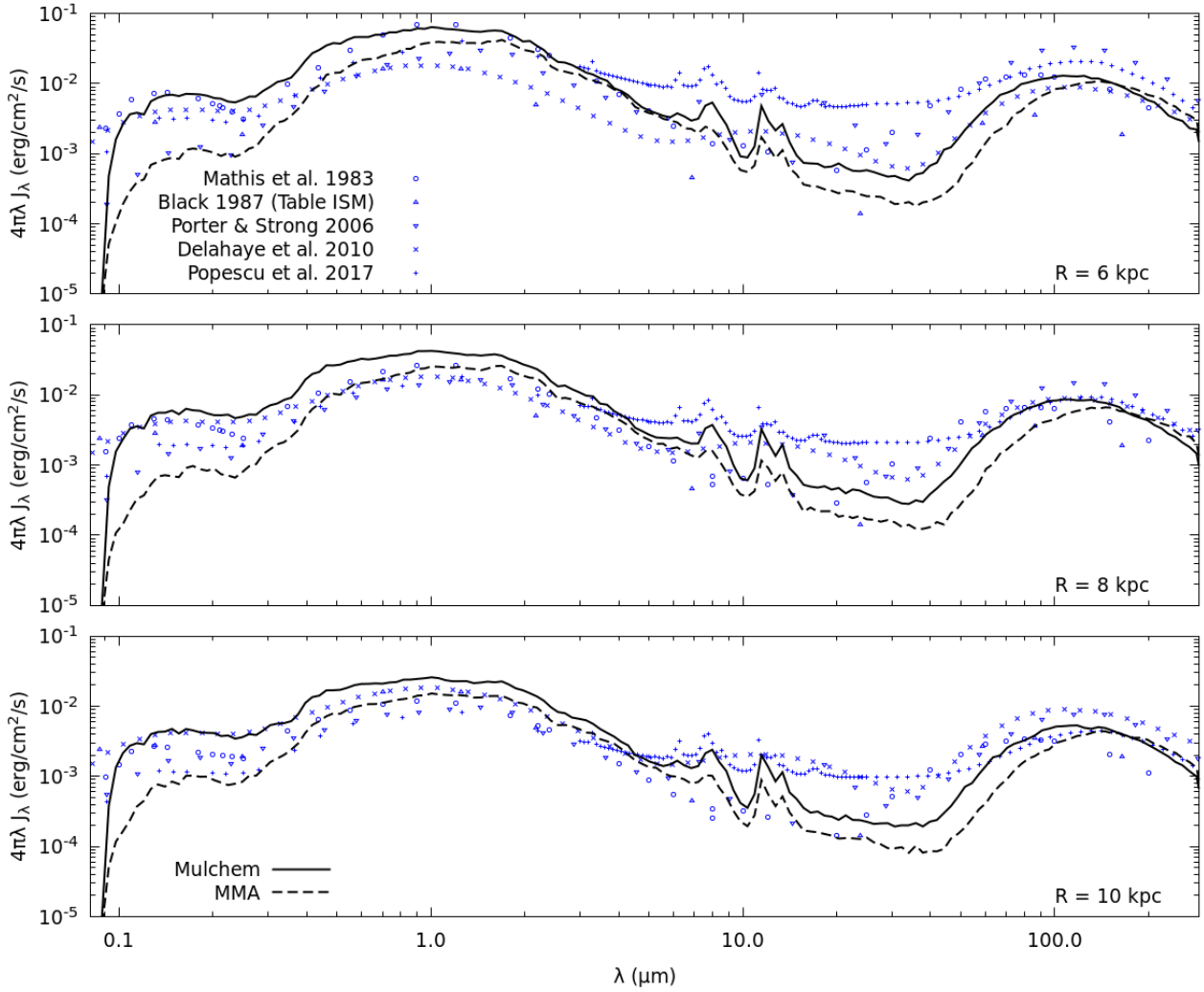

Figure 4.4: Interstellar radiation field at midplane for different locations near solar neighborhood for previous works in the literature (in blue). ISRF predicted by MIXCLASK for MULCHEM (black solid line) and MMA (Millán-Irigoyen et al., 2020, black dashed line). This figure was originally shown in Romero et al. (2022).

for $\Sigma_{\rm total}$, and the $t_{\rm infall}$ according to the following parametrizations:

$$\Sigma_{total} = (1000\,{\rm M}_\odot\,{\rm pc}^{-2})\; e^{-R/3.3\,{\rm kpc}} \tag{4.10}$$

$$t_{infall} = (2\,{\rm Gyr})\;(\frac{R}{8.5\,{\rm kpc}})^{\frac{1}{6}} \tag{4.11}$$

that has been manually optimised to reproduce the observed radial distributions of gas and stars given in Mollá et al. (2015) for the MWG.

Regarding other parameters, the MMA models also adopt the Kroupa (2001) IMF. The stellar yields used are taken from Mollá et al. (2015), selecting Gavilán et al. (2005, 2006) for low and intermediate mass stars, Woosley and Weaver (1995) for massive stars, and Iwamoto et al. (1999) for supernovae Ia. For the dust, yields are taken from Ventura et al. (2012a,b); Di Criscienzo et al. (2013) and Dell'Agli et al. (2017) for AGB stars, from Marassi et al. (2015) for massive stars dying as core-collapse supernovae, and from Nozawa et al. (2011) for the Supernoave Ia. The reader is referred to Millán-Irigoyen et al. (2020) for further details.

4.2.2 Stellar population synthesis

One of the outputs of CEM is the Star Formation Rate (SFR, mass of gas that become stars, per unit of time). In conjunction with the luminosity, $L_{SSP,\lambda}$, of a group of stars with same age and metallicity, known as simple stellar population (SSP), it is possible to compute the stellar spectra of a region within the Galaxy according

to:

$$L_\lambda = \int_0^t \psi(t-t') L_{\mathrm{SSP},\lambda}(Z(t-t'), t') dt' \tag{4.12}$$

This expression means that the total stellar spectra can be computing by adding different SSP of different age and metallicity, weighed by the SFR denoted as $\psi(t-t')$.

For each $L_{\mathrm{SSP},\lambda}$, PopStar evolutionary synthesis models were used (Mollá et al., 2009; Millán-Irigoyen et al., 2021, see also his home page[8]) with a Kroupa (2001) IMF. In particular, we have used the low resolution models of Mollá et al. (2009) instead of the newer high-resolution ones of Millán-Irigoyen et al. (2021) because the former cover a broader wavelength range, from 9.1 to $1.6 \cdot 10^5$ nm, and the high spectral resolution provided by the newer models is not a necessary ingredient for computing nebular ISRF emission.

4.2.3 Mixclask setup

The geometry of the Galaxy is approximated as a sum of concentric rings in MIXCLASK, following the same dimensions as described in 4.2.1.1. Each ring is set up with a stellar source given by Eq. (4.12). ISM mass, and Hydrogen number density are taken from surface densities at the present time, provided by both CEM.

However, both CEM differs in some physical magnitudes and outputs. On one hand, MULCHEM gives mass fractions relative to the ISM, $\tilde{X}_i = M_i/M$, regardless if either these elements are forming grains or are dispersed in diffuse gas. Therefore, MULCHEM abundances are depleted into grains in order to obtain the gas mass fractions required by MIXCLASK. For an element i, the conversion into X_i is

$$X_i = \frac{\mathcal{D}_i \tilde{X}_i}{\sum_j \mathcal{D}_j \tilde{X}_j} \tag{4.13}$$

$\mathcal{D}_i$ denotes the depletion factor of an element i. These are tabulated values given in Table 7.8 of CLOUDY documentation (Hazy 1), but they are also given in Table A.1 of appendix A. The summation shown in (4.13), which is equivalent to the gas mass, is done only for the elements given by MULCHEM. In addition, dust-to-gas ratio can be computed taking advantage of the depletion factors as

$$DTG = (\sum_j \mathcal{D}_j \tilde{X}_j)^{-1} - 1 \tag{4.14}$$

MMA model, on the other hand, follows gas metallicity Z and the mass ratio between grains and gas, without PAH. The 'grain-to-gas' ratio is converted into a DTG dividing that value by $1 - q_{pah}$. Helium abundance is not given by MMA, and its mass fraction is set to 0.24 for all regions.

Neither model follow PAH, and a value of $q_{pah} = 7\%$ is used for all regions. This is below the upper limit reported in Galliano et al. (2018) for nearby galaxies, and it is motivated on the results obtained by Robitaille et al. (2012) as well. In their work, they modelled the ISRF in the IR and found that they had to increase their fiducial q_{pah} from 4.6%, the maximum value given in the dust models of Draine and Li (2007) by a 50% in order to provide a good fit to MWG observations.

Wavelength range and convergence is the same as done in 4.1.2. That is, a wavelength range between 0.01 to 300 μm in 200 logarithmic steps, checking condition (4.8) for the default parameters.

4.2.4 Results

Figure 4.4 shows the mean intensity field predicted by MIXCLASK at three regions located at the mid-plane of the disk and $R = \{6, 8, 10\}$ kpc way from the galactic centre (top, middle and bottom panels, respectively). For the sake of comparison, it is added a representative sample of models from the literature for the Milky Way ISRF that cover the whole electromagnetic spectrum from UV to IR wavelengths. Reported values of the radiation energy density λu_λ are converted to average intensities by means of the usual relation $4\pi\lambda J_\lambda = c\lambda u_\lambda$, where c is the speed of light.

The radial dependence of the mean intensity at the mid-plane is shown in the top rows of Figure 4.5 for six different wavelengths between 0.2 and 150 μm that are representative of the different constituents of the ISRF: 0.2 μm for the (heavily absorbed) ultraviolet light from the young stellar population; Johnson B, V and K bands for older stars; and 12 and 150 μm in the infrared, where the emission PAH and grains peak, respectively, according to Figure 4.4. The corresponding vertical profiles at $R = 8$ kpc are plotted in the bottom rows of Figure 4.5.

The models by Black (1987) and Delahaye et al. (2010) were initially proposed for the Solar vicinity, and therefore they are not represented in Figure 4.5. Nevertheless, it is perhaps interesting to note that both of them have often been applied to other galactocentric distances. Black (1987) is widely used in a variety of Galactic

[8] https://www.fractal-es.com/PopStar/

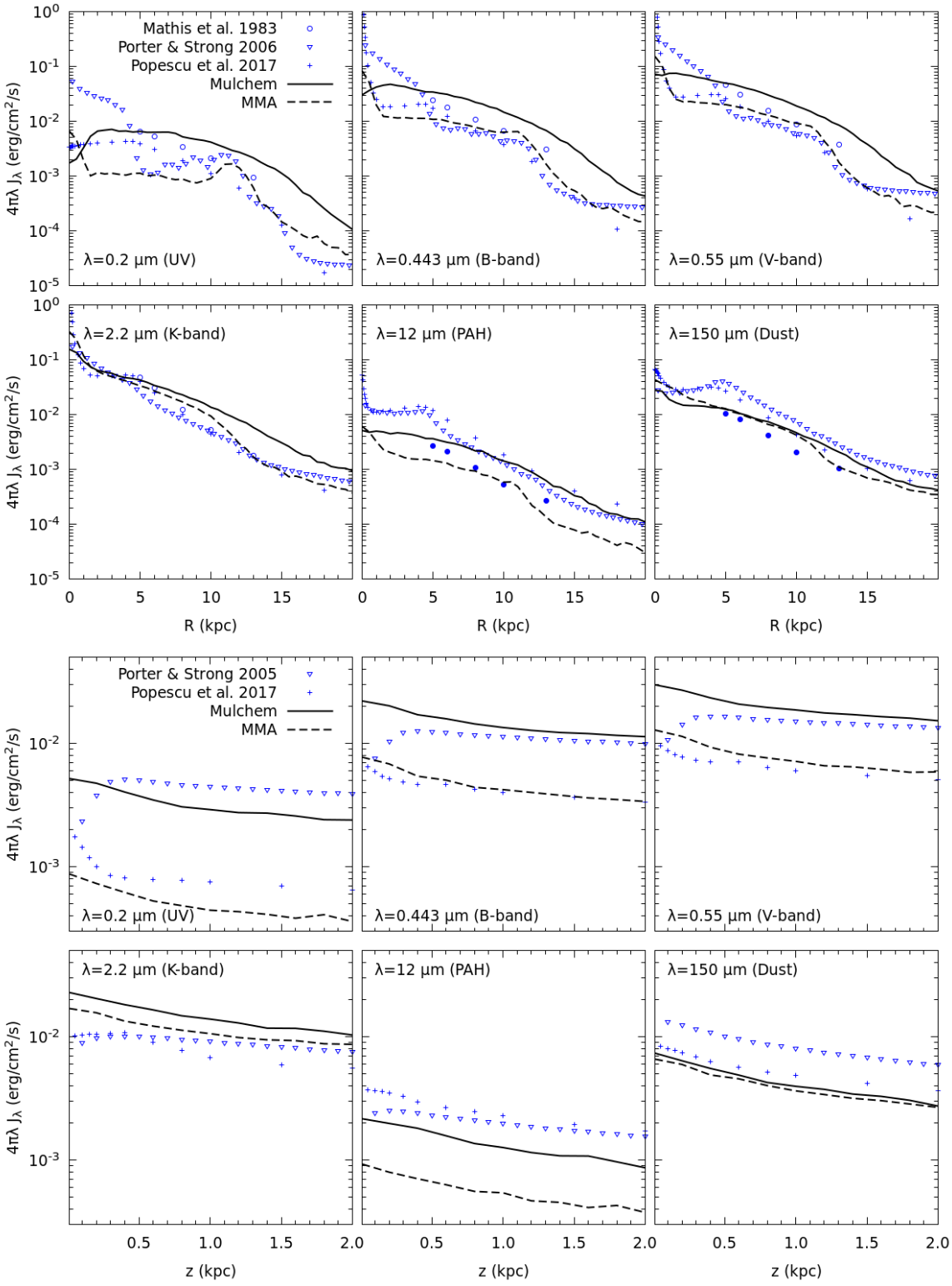

Figure 4.5: Top: Radial profiles at midplane of the interstellar radiation field for a set of characteristic wavelengths. Bottom: Vertical profiles of the ISRF at $R = 8$ *kpc* for the same wavelengths. Values predicted by MIXCLASK for MULCHEM and Millán-Irigoyen et al. (2020) (MMA) are colored black. This figure was adapted from Romero et al. (2022).

and extragalactic settings, as it is the default ISM radiation field adopted in CLOUDY (the user is able to specify an optional scaling parameter to change its overall normalisation, but the spectral shape is fixed), while the ISRF model by Delahaye et al. (2010) has received considerable attention in the astroparticle literature. It is included, for instance, as one of the available options in the cosmic ray propagation code DRAGON Evoli et al. (2017), albeit most studies based on this code make use of more elaborate prescriptions, such as e.g. Porter and Strong (2005), that provide information not only about the radial variation of the ISRF but also its vertical structure (Figure 4.5).

The set of ISRF spectra compiled is consistent within a range from about a factor of 2 to an order of magnitude between each other in the Solar neighbourhood, with the largest differences occurring in the mid-IR regime dominated by PAH emission. They also feature different radial and vertical gradients for the ultraviolet and optical bands. The discrepancy between the two models in this set that predicts the ISRF at high latitudes amounts to a factor of $3-55$, while the precise shape of the ISRF at the Galactic centre is remarkably uncertain, with differences between models that can be as high as one order of magnitude in the UV.

The predictions of the two CEMs considered in this work are broadly consistent with these trends. The fact that we do not observe an obvious systematic departure from previous results in any region of the electromagnetic spectrum (except perhaps the underestimation of the mid-IR emission discussed below) further validates the proposed approach. Note that, at variance with previous reconstructions of the Galactic ISRF, this method is not fine-tuned to reproduce the observed emission, but to provide a physically meaningful and self-consistent picture of a MWG disk galaxy, describing not only its current state but its entire assembly history.

On the other hand, there are significant differences between both chemical evolution models, which in this case can be traced to the underlying physics. Due to the assumed mass distribution, based on the Salucci et al. (2007) rotation curve, MULCHEM tends to predict a higher stellar surface density than MMA, built upon the simple parameterisation described in Section 4.2.1.2. Furthermore, the conversion of gas into stars is less efficient in MMA, and therefore this model yields a larger amount of gas and dust at the present time, and thus a more absorbed contribution of young blue stars in the short-wavelength band of the spectra. This feature is also reflected into the IR regime, where MULCHEM predicts systematically higher dust emission than MMA due to its higher stellar mass density, albeit the FIR-to-UV ratio, indicative of dust re-processing, is higher in MMA.

Regarding the spatial distribution of the ISRF, MMA predicts a flatter radial gradient compared with MULCHEM up to $R \sim 10\,\mathrm{kpc}$. At that point, the profile displays a sharp truncation due to the different star formation prescription, that features a fairly sharp transition when a critical metallicity is reached (Millán-Irigoyen et al., 2020). The vertical structure is fairly similar in both models, but one must bear in mind that this is hardly surprising, as the same geometry has been imposed in MIXCLASK to their concentric rings. In terms of the normalisation, the discrepancy between MULCHEM and MMA is quite similar to the systematic offset observed between Porter and Strong (2005) and Popescu et al. (2017).

Differences in the stellar yields may also play a role (Mollá et al., 2015; Côté et al., 2016) and lead to subtle effects in the chemical evolution of the galaxy that ultimately reflect on the predicted ISRF. One of the most relevant differences between the two models is the treatment of dust extinction, which has a significant influence at UV and IR wavelengths. Unfortunately, none of them incorporates a prescription to directly follow the evolution of PAH, and this is why we have selected the constant value $q_{\mathrm{PAH}} = 7\,\%$ as a crude, first-order approximation, following Robitaille et al. (2012). The physical properties of dust and PAH is still an open problem, and these results suggest that a simple prescription fails to reproduce the observed radiation field in the mid-IR range.

Regardless of this potential caveat, the proposed scheme can successfully predict the ISRF from a chemical evolution model. This yields significant advantages over a purely phenomenological fit. First, it is possible to trace back the different physical processes needed for the CEM, as they now have to correctly fit the observable ISRF at several wavelengths. Once the CEM is fully calibrated, it can be used to reproduce ISRF from very different kind of systems that are not only spiral galaxies (e.g.: Popescu and Tuffs, 2013), allowing to investigate its physics and elements from this observable.

Chapter 5

Final Remarks

5.1 Effects of the radiation field

5.1.1 Structure, evolution and feedback of SNR

The analytical models considered in Chapter 2 show that radiative cooling is crucial in order to determine the physical properties of SNR shocks and the amount of energy that is ultimately transferred to the surrounding interstellar medium. Depending on the ambient gas density, these solutions provide an analytical understanding of the transition from the canonical evolutionary path, where most of the explosion energy is radiated away, towards a low-density regime where the strong shock gradually decays into a sound wave that carries most of the initial energy.

On the one hand, young massive stars generate Core-Collapse SNe. Following statistical studies from Aramyan et al. (2016) and Hakobyan et al. (2017) these SNe, and hence their corresponding SNR, are heavily correlated with spiral arms and the thick disk, respectively. Thus, these SNR follow the canonical path since the ISM density is high enough to allow the remnant to become radiative, albeit some of these SNe will explode inside another SNR and form superbubbles, which is another whole story (for the interested reader, see Keller et al., 2014; Sharma et al., 2014; Kim et al., 2017; Gentry et al., 2017, 2019).

On the other hand, a fraction of massive stars become runaways (Gies and Bolton, 1986) and may die in the hot ISM. This can also be the case for the fraction of white dwarfs that explode as Type Ia SNe, as they start to appear between 1 to 10 Gyr (see, for example Greggio, 2005; Maoz and Mannucci, 2012; Castrillo et al., 2021) after their original stellar population formed, giving the SN progenitor more than enough time to leave its birthplace. The same studies cited above (Aramyan et al., 2016; Hakobyan et al., 2017) support the idea that Type Ia SNe locations are more sparse that core-collapse SNe. They can also appear in elliptical galaxies (e.g.: Barkhudaryan et al., 2019) and even outside the ISM (Maoz et al., 2005; Mannucci et al., 2008).

The formalism presented in Chapter 2 may provide a fairly accurate approximate description that covers the whole range of ambient densities, and it could be used to devise a simple analytical prescription for supernova energy injection in large-scale simulations, which cannot solve the evolution of individual SNR due limited resolution. These analytical prescriptions represent a physically-motivated model rather than a mere phenomenological fit, and they shift the focus back to the injected energy, considered by the first numerical studies (e.g.: Thornton et al., 1998) some decades ago, rather than the momentum input to the ISM that is nowadays highlighted in more recent models. There are two reasons to return to energy injection: First, the momentum-conserving regime is never reached in low-density environments (see Figure 3.14). Second, the convenience of my model to obtain energy directly from $\mathcal{I}^2$.

In addition to radiative cooling, Chapter 3 addresses the heating arising from the absorption of photons from the ISRF, going significantly beyond the first-order approximations that are commonly found in the literature. By defining an external radiation field (ERF) based on the ISRF tabulated by Cloudy, appropriate for the Solar neighborhood, I reconcile the two most popular prescriptions for radiative heating (i.e.: turning off cooling at a threshold temperature around $\sim 10^4$K, and the constant heating rate advocated by Koyama and Inutsuka, 2002) and recover previous results regarding the evolution of isolated SNR under these conditions.

However, quite importantly, I find differences in the SNR luminosity and shell structure. Unlike energy and momentum, the SNR luminosity does discriminate between shielded and unshielded regions of the interstellar medium. Due to its unquestionable importance as an observable tracer, in combination with its key role in the description of the shock evolution in the analytical models, the SNR luminosity is arguably one of the most interesting quantities to be predicted by future, more elaborate theoretical models. The shell structure is important for knowing the gas fractions that will end as hot, warm or cold ISM after shock passage. If the SNR is fully adiabatic, then the swept-up ISM will end up in a hot phase, while if it is a shielded SNR, there will be a cold ISM fraction in the shell, albeit for unshielded ones this fraction would be in warm state. These results

are similar to those found in Walch and Naab (2015) for molecular clouds, where the authors encounter that most of the SNR mass is in the cold state ($T < 300\,\mathrm{K}$, from its paper) when heating is enabled with Koyama and Inutsuka (2002) heating rate, which is the equivalent to the shielded cases. These differences will propagate in the star formation rate. According to the scheme of Fig. 1 displayed at the beginning of this dissertation, only the cold ISM is able to form stars. If the ERF is unshielded, the SNR will leave behind a warm medium that will not efficiently form new stars. In contrast, if the environment where the supernova explodes is well shielded from external radiation, the ambient medium will end up in a cold, dense state, resulting in *positive* SN feedback that will enhance further star formation.

This picture stands for the solar neighborhood, and the next question is what happens outside of this region. When the heating by an ERF is considered, the location where a SNe explodes is even more important compared with the low-density and high-density discussion above. From the *heating versus cooling* perspective outlined in section 3.3, two new possible types of SNR appear: critical and heated. The conditions where these uncommon SNR may arise are extremely rare, but they would bring more catastrophic feedback compared with the canonical, purely radiative SNR. Just one of them (in particular, a heated SNR) would dictate the ensuing evolution of its surroundings. However, for a heated SNR to take place one needs: 1) a location where heating is very important (e.g.: close to an AGN) and, 2) the possibility that a SNe may appear there (e.g.: a Type Ia SN from a binary star close to the galactic centre). Chances to meet these two requirements at once are really small, but it is a possibility that cannot be truly ruled out. It would be interesting to carry out the academic exercise of Section 3.3 in a more realistic way, and that is what MIXCLASK tries to solve in Chapter 4. Thanks to this radiative transfer code, you are now able to self-consistently compute the ISRF for a chemical evolution model and repeat the exercise of the SNR evolution under a realistic ERF in other plausible conditions, such as at the galactic centre, close to an AGN, in elliptical galaxies, etc.

To sum up, I am able to reach the following two conclusions about the effect of radiative processes on SNR:

- First, the luminosity of the SNR is a more suited quantity, compared with the energy and momentum injected into the ISM, for developing (semi-)analytical models and for tracking the SNR evolution. This is because it is able to discriminate if the SNR is shielded (or not) from radiation.

- Second, studies of the SNR evolution in different environments, in particular outside solar neighborhood, must include a treatment of the ERF permeating the surroundings of the SNR.

5.1.2 Other environments and applications

Besides the particular case of SNR, it is expected that the radiation field has an important effect in many different contexts. The methodology developed in Chapter 4 may be applied not only to compute the ISRF of the Milky Way in the solar neighborhood, but also in a wide variety of environments (cf. the Popescu and Tuffs, 2013, library for star-forming galaxies). Let me name here a few instances of science cases that would benefit from a model of the ISRF along the lines proposed in this thesis:

1. **Stellar regions**: Our methodology would also be useful to characterise the radiation field around astrophysical objects such as e.g. planetary nebulae or HII regions. For the latter, a very simplistic model has been used in section 4.1.2 as a test case, but a more realistic simulation would be fairly straightforward.

2. **Elliptical galaxies**: These objects present very different properties compared with the Milky Way. There are no significant young stellar population because the gas within the galaxy is so hot to produce new stars. Such a high temperature has been suggested to be the cause of several mechanical feedback mechanisms into action, such as Type Ia SNe and AGN (Mathews and Baker, 1971; Gaspari et al., 2012), among others (for a review, see Mathews and Brighenti, 2003). As a result, you will encounter different ingredients that compose their radiation fields: in addition to the already mentioned AGN, gas emits in X-rays (Diehl and Statler, 2007), and there is an important contribution of stellar populations at Horizontal-Branch or later stages (Binette et al., 1994; Dorman et al., 1995). As shown in this thesis, the ensuing differences in the ISRF is expected to have an impact on how this galaxies evolve.

3. **Extragalactic background**: The UV emission from external galaxies is an extra component in addition to the ISRF.Its spectrum was reported in the literature a long time ago (Haardt and Madau, 1996, 2012), and it has already been suggested that it should be accounted for in the cooling function (Wiersma et al., 2009). In spiral galaxies, ionizing radiation will be absorbed when it reaches the galactic disk, but this argument does not hold outside disks (and perhaps outside spiral arms) as the UV/X-ray background becomes much less shielded. These photons may not completely prevent star formation, but they will certainly alter the gas properties and change the SNR feedback as shown in this thesis.

4. **Early universe**: Studies of galaxy formation at high redshift have suggested that UV radiation pays an even more important role than at the present time (Wise et al., 2012; Okamoto et al., 2014; Ceverino

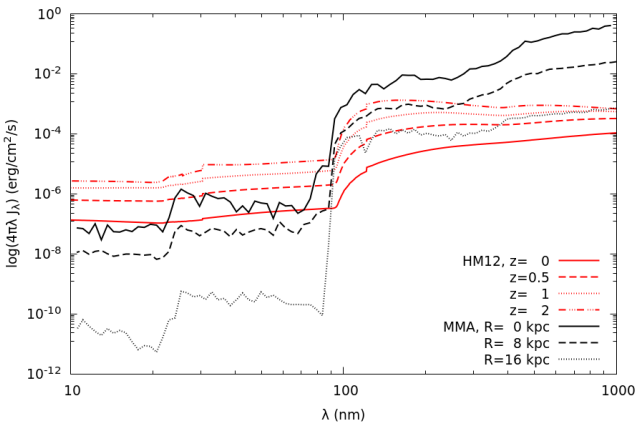

Figure 5.1: Millán-Irigoyen et al. (2020) ISRF (MMA) obtained with MIXCLASK at different galactocentric radius against Haardt and Madau (2012) (HM12) background field at different redshifts.

et al., 2014). To begin with, there were many more UV/X-Ray photons at earlier times. To illustrate this, I compare in Figure 5.1 the ISRF obtained from Millán-Irigoyen et al. (2020) at different galactocentric radius with the Haardt and Madau (2012) background for different redshifts. You do not have to go that far back in time ($z = 1$, which is roughly 8 Gyr ago[1]) to see how the UV background becomes comparable to the solar neighborhood ISRF.

5. **Observational constraints**: Explicitly modelling the ISRF in different environments will greatly increase the predictive power of chemical evolution models. The estimated intensity of the radiation field (e.g. computed by MIXCLASK) can be used as a self-consistency check and a probe to constrain the CEM parameters by direct comparison with observations at different wavelengths. This approach applies both to the calibration of internal model parameters, as well as to the estimation of physical properties of real galaxies. For example, Natale et al. (2022) predicted the Milky Way ISRF in order to compute the current SFR and stellar mass of our Galaxy.

This list is by no means exhaustive, and it is only meant to illustrate some straightforward applications of our methodologies to other science cases related to galaxy formation and evolution. I therefore argue that a detailed treatment of the ISRF can shed light on multiple open problems in the field:

- Third, it is possible to compute the ISRF predicted by chemical evolution models and use it as initial condition to study different processes that take place within galaxies, as well as a theoretical prediction that can be used to constrain the model parameters and/or estimate the physical properties of a real galaxy from observational data.

5.2 The technical side of this thesis

The resources used are other element in common of these chapters. Figure 5.2 shows the main two computers used for this thesis. The laptop processor is an Intel-Core i7-6500U with four cores of 2.5 GHz while the desktop has also an Intel-Core i5-4570 with four cores of 3.2 GHz. The only exception is in 3.1.2.2, for the test case of the numerical code against FLASH, which was performed in Astronomical Institute of the Czech Academy of Sciences.

Each chapter presents a very different technical approach: First, I present analytical solutions that can be used as semi-analytical model of SNR. This is a cheaper method compared with full simulations, which is the selected method in chapter 3, which is attached with some approximations, such as spherical symmetry and precomputed tables for cooling/heating, as well as some techniques, such as AMR and rewriting some equations in spherical coordinates (see appendix C).

Chapter 4 combines two public codes into a new one in order to enhance their predictions. In this case, the taxing part and all the optimization burden go to CLOUDY and SKIRT, while the communication between both

[1] Assuming a flat universe with $H_0 = 69\,\mathrm{km/s/Mpc}$, $\Omega_{\Lambda,0} = 0.7$ and $\Omega_{M,0} = 0.3$, the conversion to time since the Big Bang is

$$t(z) = \frac{2}{3H_0\sqrt{\Omega_{\Lambda,0}}} \log[\sqrt{\frac{\Omega_{\Lambda,0}}{\Omega_{M,0}}(\frac{1}{z+1})^3} + \sqrt{\frac{\Omega_{\Lambda,0}}{\Omega_{M,0}}(\frac{1}{z+1})^3 + 1}] \tag{5.1}$$

yielding $\{13.7, 8.5, 5.8, 3.2\}$ *Gyr* for $z = \{0, 0.5, 1, 2\}$ in Figure 5.1

Figure 5.2: Main computers used in the PhD. No supercomputers were harmed during the realization of this thesis.

programs can be done with slower, yet easier to learn, programming languages such as `python`. The reader should realize that you can solve the same question, computing an ISRF, with your own code as well, as shown in appendix D, or even with analytical solutions (see Mathis et al., 1983; Delahaye et al., 2010). Therefore, I am able to claim the following:

- Fourth, it is feasible to incorporate radiation without restrictive assumptions such as CIE, nor relying into computationally-expensive simulations that on-the-fly radiative transfer brings.

Nevertheless, this does not mean that you can do everything in your personal computer. The computationally-cheap argument breaks down when you need to do simulations in 3D or to include on-the-fly radiative transfer. 3D simulations, or at least 2D ones, are a must when you are interested in instabilities, inhomogeneities and magnetic fields because they do not properly manifest in 1D simulations, although you can still use them as demonstrated in previous works (Slavin et al., 2015; Petruk et al., 2018; Pittard, 2019). On-the-fly radiative transfer brings the issue that you have to track the ionization state of gas alongside its own dynamics plus the radiation sources (mainly stars), which can be more complicated if the simulation follows chemical species instead of only gas. Actually, all these caveats can be summarized as you have to increase the number of equations required to solve numerically.

However, an ISRF model, which can be done with Mixclask as commented previously, it is still useful even with an on-the-fly radiative transfer in a hydrodynamic simulation due to spectral and spatial resolution. On the spectral side, you have to add an extra equation per wavelength (or wavelength range, say, UV photons) for ray-tracing algorithms. In the case of monte-carlo ones, it is the sample of photon packets that has to be increased. Therefore, it becomes impractical to make an on-the-fly ISRF full spectra. On the spatial side, there are two cases: in lower scales, up to galactic scale, you still have to include an ERF, regardless of whether is the ISRF or the extragalactic background, both having an UV/X-ray part that should not be ignored. For bigger scales, galaxies may not be resolved and thus they will greatly benefit to have an ISRF attached into them to become a radiative source themselves.

5.3 Conclusions

Within a galaxy, you find three major actors: dark matter, stars and the interstellar medium (ISM). The latter is further subdivided into gas, dust, cosmic rays, magnetic fields and the radiation that pervades the ISM. This dissertation puts the spotlight on radiative transfer and the interaction that the ISM has with light. To highlight the importance of radiative transfer, I include radiation into the well-studied problem of supernova remnant (SNR) evolution to illustrate the differences and improvements over previous works in the literature. Then, I present a way to model the interstellar radiation field (ISRF) for a given distribution of stars, gas and dust. All these works are made neither with very restrictive assumptions of radiation fields nor the computationally-expensive on-the-fly radiative transfer.

Chapter 2 first reviews the basics of SNR, describing the classical evolutionary path along with the evolution in a low-density regime such as the hot ISM or elliptical galaxies. There, I present a formalism in terms of SNR energy balance as functions of new parameters $\mathcal{I}$ and $\mathcal{T}$. The former is intimately related with total energy as $E \propto \mathcal{I}^2$, whereas the latter is a time that follows the deviation from the Sedov-Taylor solution. Both quantities are related with the time derivative. In order to derive analytical solutions, I use the swept-up ISM thermal energy by the SNR and its luminosity. On one hand, swept-up energy allows to merge the low-density SNR evolution with its classical path. On the other hand, the luminosity plays a greater role for deriving more sophisticated approximations of the canonical SNR evolution. In particular, a ~ 15 % of SNR energy is radiated away before any proper radiative phase begins. After that, from the luminosity of a fully radiative shock, I am able to recover a off-set power-law reminiscent of the ansatz given by Cioffi et al. (1988) that converges into the Pressure-Driven snowplough result at large times. Furthermore, these solutions are also tested against numerical simulations. Analytical solutions agree considerably well with a numerical SNR, but the parameterization used for the different SNR stages are unable to reproduce the discontinuity that occurs at the transition to the radiative phases because its luminosity was not modelled properly.

Chapter 3 focuses on SNR under the effects of an external radiation field (ERF), and expands the published results of Romero et al. (2021). In this aspect, an Eulerian hydrodynamic code is developed to run 1D simulations where cooling and heating is handled by interpolating tables. On the other hand, ERF are generated using the photoionization code Cloudy (Ferland et al., 2017) twice. First, I study SNR place in the solar neighborhood. In order to do that, I generate the mean intensity field attenuated by an effective column density $N_{\rm eff}$ from 10^{18} to 10^{21} cm^{-2}. Then, I use Cloudy again to create the cooling and heating tables for the numerical code. The effective column density represents how obscured the ionizing stars of the ISRF are from the environment where the SNR appears, and divides it into two regimes: At high $N_{\rm eff}$, the ISM is shielded from ionizing radiation, and its heating rate resembles the constant value advocated by Koyama and Inutsuka (2002). At low $N_{\rm eff}$, the heating rate prevents cooling at temperatures lower than $\sim$ 7000 K, which is labelled in the chapter as unshielded case. For solar neighborhood conditions, the usual SNR parameters used in the literature does not change significantly if the media is shielded or not. That is, its shock radius, R, SNR energy, E, and momentum p. However, there are important differences between shielded and unshielded SNR for its luminosity and its shell structure. For the former, the SNR luminosity follows a different logarithmic slope after the SNR becomes radiative, which leads to a value several orders of magnitude higher for unshielded SNR. For the latter, the SNR thin-shell is unable to generate cold gas in the unshielded case. Moreover, at its very late stages, the shell becomes thicker over time. At the end of the chapter, I also present an academic exercise that answers what happens if heating and/or cooling are relevant for SNR evolution or not. From that point of view, there are four distinct regimes: radiative and adiabatic, which heating is irrelevant and resembles the classical SNR and Tang and Wang (2005) evolution, respectively; and critical and heated cases, where heating is always important, but cooling can, or cannot, be relevant, respectively. For these two cases, whose conditions are yet to be seen in a realistic context, albeit one single SNR happening there, no matter how unlikely it may be, will dictate the subsequent analysis of the galaxy evolution, specifically for the heated SNR.

Last chapter of this thesis revisits the submitted paper of Romero et al. (2022), devoted to the modelling of the ISRF from a composition of stars, gas and dust. In that regard, I released a code called Mixclask (https://github.com/MarioRomeroC/Mixclask) that combines Cloudy with the monte-carlo radiative transfer code Skirt (Camps and Baes, 2020) to calculate the mean intensity field at different positions. Mixclask works by asking Skirt to perform a simulation considering only stellar sources first to make a first guess. Then, this result is imported to Cloudy to predict the emissivity and opacity of a mixture of gas and dust as function of wavelength. Finally, Skirt is run again to make a new guess now adding the total contribution of stars, gas and dust. This process is repeated iteratively, calling both codes sequentially in order to make more accurate estimates of the mean intensity field. To test this code, I designed a test case consisting of a black-body surrounded by a spherical shell of gas and dust with uniform density, reminiscent of a HII region irradiated by a B star. Mixclask results are in excellent agreement against a standalone, spherically symmetric, Cloudy simulation. I also show how to use Mixclask for a realistic scientific application by computing the ISRF of the Milky Way Galaxy (MWG). To do that, I utilize the chemical evolution models (CEM) of Mollá et al. (2017, 2022) (Mulchem) and Millán-Irigoyen et al. (2020) (MMA). A CEM is a semi-analytical model that follows the

evolution of a galaxy in terms of the interstellar gas and stars. There are some differences between MULCHEM and MMA models. For the former, it predicts the evolution of many chemical elements in the ISM, whereas the latter tracks the formation and destruction of dust grains. Both models give broadly consistent ISRF compared with previous and phenomenological results from the literature, although both CEM underestimate the mid-IR emission. Furthermore, they also present notable differences in their ISRF. In particular, they predict different stellar and dust emission and radial gradients between the UV to optical wavelengths. In any case, these results show the feasibility of including radiative transfer into a CEM. Their predictions can give more insight to the underlying physics of both CEM, increasing their predicting power, and in galaxies, being able to recreate ISRF for non-spiral galaxies.

Having summarized the contents of this thesis, and putting everything into the same context, I hereby conclude:

1. The luminosity of the SNR is a more suited quantity, compared with the energy and momentum injected into the ISM, for developing (semi-)analytical models and for tracking the SNR evolution. This is because it is able to discriminate if the SNR is shielded (or not) from radiation.

2. Studies of the SNR evolution in different environments, in particular outside solar neighborhood, must include a treatment of the ERF permeating the surroundings of the SNR.

3. It is possible to compute the ISRF predicted by chemical evolution models and use it as initial condition to study different processes that take place within galaxies, as well as a theoretical prediction that can be used to constrain the model parameters and/or estimate the physical properties of a real galaxy from observational data.

4. It is feasible to incorporate radiation without restrictive assumptions nor relying into computationally-expensive simulations that on-the-fly radiative transfer brings.

5.4 Conclusiones

En una galaxia, hay tres actores importantes: materia oscura, estrellas y el medio interestelar (ISM, por sus siglas en inglés). Este último se subdivide en gas, polvo, rayos cósmicos, campos magnéticos y el campo de radiación que atraviesa el ISM. Esta tesis pone el foco en el transporte radiativo y en la interacción que el ISM tiene con la luz. Para destacar la importancia del transporte radiativo, incluyo radiación en la evolución de los remanentes de supernova (SNR, en inglés), un problema bien estudiado, para recalcar las diferencias y mejoras frente a trabajos previos en la literatura. Después, presento una forma de modelar el campo de radiación interestelar (llamado ISRF en inglés) para una distribución concreta de estrellas, gas y polvo. Todos estos trabajos se han realizado sin recurrir a aproximaciones muy restrictivas del campo de radiación ni aplicando transporte radiativo sobre la marcha porque es caro computacionalmente.

El capítulo 2 empieza revisando los fundamentos de los SNR, describiendo la evolución clásica junto con la que se produce en medios de baja densidad tales como el ISM caliente o en galaxias elípticas. Ahí presento un formalismo en términos del balance energético de los SNR como funciones de dos nuevos parámetros $\mathcal{I}$ y $\mathcal{T}$. El primero esta íntimamente relacionado con la energía total como $E \propto \mathcal{I}^2$, mientras que el segundo es un tiempo que sigue como se desvía la evolución de la solución de Sedov-Taylor. Ambas cantidades están relacionadas con la derivada temporal. A la hora de obtener soluciones analíticas, uso la energía térmica barrida del ISM por el SNR y su luminosidad. Por una parte, la energía barrida permite juntar la evolución de SNR en medios poco densos con el camino clásico. Por otra parte, la luminosidad juega un papel mayor a la hora de derivar aproximaciones más sofisticadas de la evolución canónica de SNR. En concreto, sobre ~ 15 % de la energía del SNR se radia antes de que empiece una fase radiativa. Después de eso, soy capaz de recuperar una solución de la ley de potencias desplazada que recuerda al ansatz dado por Cioffi et al. (1988) que converge al resultado la fase conocida en inglés como *Pressure-Driven snowplough* a tiempos grandes. Las soluciones analíticas coinciden considerablemente bien con SNR numéricos, pero la parametrización usada para las distintas fases es incapaz de reproducir la discontinuidad que ocurre en la transición a las fases radiativas porque la luminosidad no fue modelada correctamente.

El capítulo 3 se enfoca en SNR bajo los efectos de un campo de radiación externo (bautizado en inglés como ERF), y expande los resultados publicados de Romero et al. (2021). En este aspecto, se desarrolla un código hidrodinámico Euleriano para correr simulaciones en 1D donde el enfriamiento y el calentamiento se trata interpolando tablas. Por otra parte, los ERF son generados usando el código de fotoionización CLOUDY (Ferland et al., 2017) dos veces. En primer lugar, estudio SNR localizadas en la vecindad solar. Para empezar, creo el campo de radiación promedio atenuado por una densidad de columna efectiva, N_{eff}, de 10^{18} hasta 10^{21} cm^{-2}. Después, uso CLOUDY de nuevo para crear las tablas de enfriamiento y calentamiento para el código numérico. La densidad de columna efectiva representa como de bloqueada esta la radiación proveniente de estrellas ionizantes

en el ISRF del entorno donde aparece el SNR, y divide el mismo en dos regiones: Para N_{eff} altos, el ISM esta protegido de radiación ionizante, y su tasa de calentamiento recuerda al valor constante propuesto por Koyama and Inutsuka (2002). Para N_{eff} bajos, la tasa de calentamiento evita el enfriamiento para temperaturas inferiores a $\sim$ 7000 K, que se ha denotado como caso no-protegido, o expuesto. Para la vecindad solar, los parámetros habituales para SNR usados en la literatura no cambian significativamente con respecto a si el medio esta protegido o no de radiación. Estos parámetros son, su radio de choque, R, la energía, E, y el momento, p del SNR. Sin embargo, si hay cambios importantes en la luminosidad del SNR así como la estructura de su capa. Para empezar, la luminosidad presenta una pendiente logarítmica distinta cuando el SNR se vuelve radiativo, siendo varios órdenes de magnitud superior para el caso donde el SNR esta expuesto a radiación. Además, el SNR es incapaz de generar gas frío en la capa fina que forma. Es más, en etapas muy tardias de su evolución, la capa se va volviendo más gruesa progresivamente. Al final del capítulo, también presento un ejercicio académico que trata de responder a qué pasaría si el calentamiento y/o el enfriamiento son relevantes para la evolución de SNR. Desde ese punto de vista, hay cuatro regímenes: radiativo y adiabático, donde el calentamiento es irrelevante y recuerda a la evolución clásica de SNR y a la propuesta por Tang and Wang (2005), respectivamente; y críticos y calentados, donde el calentamiento es siempre importante, pero no necesariamente el enfriamiento. Para estos dos últimos casos, todavía pendientes de que se vean en un contexto realista, un único SNR ocurriendo ahí, por muy improbable que sea, dictará el análisis posterior de la evolución de una galaxia, sobre todo para SNR calentados.

El último capítulo de esta tesis revisita el artículo enviado de Romero et al. (2022), centrado en la modelización del ISRF a partir de una composición de estrellas, gas y polvo. En este aspecto, he liberado un código llamado Mixclask (https://github.com/MarioRomeroC/Mixclask) que combina Cloudy con el código de transporte radiativo, basado en métodos monte-carlo,Skirt (Camps and Baes, 2020) para calcular el campo de radiación promedio en distintas posiciones. Mixclask funciona llamando a Skirt para hacer una primera estimación del campo de radiación considerando sólo fuentes estelares. Después, el resultado se importa a Cloudy para predecir la emisividad y opacidad de una mezcla de gas y polvo en función de la longitud de onda. Finalmente, se ejecuta de nuevo Skirt para hacer una nueva estimación con la contribución total de estrellas, gas y polvo. El proceso se repite de manera iterativa, llamando a ambos códigos de manera secuencial para hacer estimaciones más precisas del campo de radiación promedio. Para testear este código, he diseñado un caso de prueba que consiste en un cuerpo negro rodeado de una corona esférica de gas y polvo a densidad uniforme, que recuerda una región Hii irradiada por una estrella de tipo B. Los resultados de Mixclask son prácticamente idénticos frente a los generados por una simulación de Cloudy por si sola asumiendo simetría esférica. También muestro como usar Mixclask para un caso científico más realista calculando el ISRF de la Vía Láctea. Para ello, utilizo los modelos de evolución química (CEM, por sus siglas en inglés) de Mollá et al. (2017, 2022) (Mulchem) y de Millán-Irigoyen et al. (2020) (MMA). Un CEM es un modelo semi-analítico que sigue la evolución de una galaxia en términos de las estrellas y gas interestelar. Para los modelos de Mulchem y MMA hay algunas diferencias, ya que el primero predice las abundancias totales del ISM para bastantes elementos químicos, mientras que el segundo traza la creación y destrucción de los granos de polvo. Ambos modelos dan ISRF consistentes con resultados anteriores, fenomenológicos, de la literatura, aunque ambos CEM subestiman la emisión en el IR medio. Además, estos modelos presentan diferencias notables en sus ISRF. En particular, predicen distinta emisión de estrellas y polvo, así como un gradiente radial diferente en el UV y en el óptico. En cualquier caso, los resultados demuestran la posibilidad de incluir transporte radiativo en un CEM. Sus predicciones podrían dar más información acerca de las físicas añadidas en los CEM, aumentando su poder predictivo, y en galaxias, pudiéndose recrear ISRF en galaxias no espirales.

Habiendo resumido el contenido de esta tesis, y poniendo todo bajo el mismo contexto, concluyo:

1. La luminosidad del SNR es una cantidad más idónea, en comparación con la energía y momento inyectado al ISM, para desarrollar modelos (semi) analíticos y para trazar la evolución del SNR. Esto es debido a que es capaz de discriminar si el SNR esta protegido (o no) de la radiación.

2. Los estudios de SNR en distintos entornos, en particular fuera de la vecindad solar, deben incluir un tratamiento del ERF que esta presente en los alrededores del SNR.

3. Es posible calcular el ISRF predicho por modelos de evolución química y usarlos como condición inicial para estudiar distintos procesos que tienen lugar en galaxias, así como una predicción teórica que puede usarse para restringir parámetros en modelos y/o estimar las propiedades físicas de una galaxia real a partir de datos observacionales.

4. Es viable incorporar radiación sin necesidad de suposiciones restrictivas ni recurriendo a simulaciones computacionalmente costosas que implican el transporte radiativo sobre la marcha.

Bibliography

L. S. Aramyan, A. A. Hakobyan, A. R. Petrosian, V. de Lapparent, E. Bertin, G. A. Mamon, D. Kunth, T. A. Nazaryan, V. Adibekyan, and M. Turatto. Supernovae and their host galaxies - IV. The distribution of supernovae relative to spiral arms. *Monthly Notices of the Royal Astronomical Society*, 459(3):3130–3143, July 2016. doi: 10.1093/mnras/stw873.

B. Arbutina. Evolution of Supernova Remnants. *Publications de l'Observatoire Astronomique de Beograd*, 97: 1–92, Dec. 2017.

D. A. Badjin, S. I. Glazyrin, K. V. Manukovskiy, and S. I. Blinnikov. On physical and numerical instabilities arising in simulations of non-stationary radiatively cooling shocks. *Monthly Notices of the Royal Astronomical Society*, 459(2):2188–2211, June 2016. doi: 10.1093/mnras/stw790.

M. Baes, J. I. Davies, H. Dejonghe, S. Sabatini, S. Roberts, R. Evans, S. M. Linder, R. M. Smith, and W. J. G. de Blok. Radiative transfer in disc galaxies - III. The observed kinematics of dusty disc galaxies. *Monthly Notices of the Royal Astronomical Society*, 343(4):1081–1094, Aug. 2003. doi: 10.1046/j.1365-8711.2003.06770.x.

L. V. Barkhudaryan, A. A. Hakobyan, A. G. Karapetyan, G. A. Mamon, D. Kunth, V. Adibekyan, and M. Turatto. Supernovae and their host galaxies - VI. Normal Type Ia and 91bg-like supernovae in ellipticals. *Monthly Notices of the Royal Astronomical Society*, 490(1):718–732, Nov. 2019. doi: 10.1093/mnras/stz2585.

L. Binette, C. G. Magris, G. Stasińska, and A. G. Bruzual. Photoionization in elliptical galaxies by old stars. *Astronomy and Astrophysics*, 292:13–19, Dec. 1994.

G. S. Bisnovatyi-Kogan and S. A. Silich. Shock-wave propagation in the nonuniform interstellar medium. *Reviews of Modern Physics*, 67:661–712, July 1995. doi: 10.1103/RevModPhys.67.661.

J. H. Black. Heating and Cooling of the Interstellar Gas. In D. J. Hollenbach and J. Thronson, Harley A., editors, *Interstellar Processes*, volume 134, page 731, Jan. 1987. doi: 10.1007/978-94-009-3861-8_27.

J. M. Blondin, E. B. Wright, K. J. Borkowski, and S. P. Reynolds. Transition to the Radiative Phase in Supernova Remnants. *The Astrophysical Journal*, 500:342–354, June 1998. doi: 10.1086/305708.

F. Brighenti and W. G. Mathews. Thermal Evolution of Supernova Iron in Elliptical Galaxies. *The Astrophysical Journal*, 630(2):864–874, Sep 2005. doi: 10.1086/432042.

P. Camps and M. Baes. SKIRT 9: Redesigning an advanced dust radiative transfer code to allow kinematics, line transfer and polarization by aligned dust grains. *Astronomy and Computing*, 31:100381, Apr. 2020. doi: 10.1016/j.ascom.2020.100381.

A. Castrillo, Y. Ascasibar, L. Galbany, S. F. Sánchez, C. Badenes, J. P. Anderson, H. Kuncarayakti, J. D. Lyman, and A. I. Díaz. The delay time distribution of supernovae from integral-field spectroscopy of nearby galaxies. *Monthly Notices of the Royal Astronomical Society*, 501(3):3122–3136, Mar. 2021. doi: 10.1093/mnras/staa3876.

D. Ceverino, A. Klypin, E. S. Klimek, S. Trujillo-Gomez, C. W. Churchill, J. Primack, and A. Dekel. Radiative feedback and the low efficiency of galaxy formation in low-mass haloes at high redshift. *Monthly Notices of the Royal Astronomical Society*, 442(2):1545–1559, Aug. 2014. doi: 10.1093/mnras/stu956.

R. A. Chevalier. The Evolution of Supernova Remnants. Spherically Symmetric Models. *The Astrophysical Journal*, 188:501–516, Mar. 1974. doi: 10.1086/152740.

D. F. Cioffi, C. F. McKee, and E. Bertschinger. Dynamics of radiative supernova remnants. *The Astrophysical Journal*, 334:252–265, Nov. 1988. doi: 10.1086/166834.

B. Côté, C. Ritter, B. W. O'Shea, F. Herwig, M. Pignatari, S. Jones, and C. L. Fryer. Uncertainties in Galactic Chemical Evolution Models. *The Astrophysical Journal*, 824(2):82, June 2016. doi: 10.3847/0004-637X/824/2/82.

E. R. Coughlin. The structure of nearly isothermal, adiabatic shock waves. *Monthly Notices of the Royal Astronomical Society*, 496(1):L43–L47, July 2020. doi: 10.1093/mnrasl/slaa087.

S. Cristallo, L. Piersanti, O. Straniero, R. Gallino, I. Domínguez, C. Abia, G. Di Rico, M. Quintini, and S. Bisterzo. Evolution, Nucleosynthesis, and Yields of Low-mass Asymptotic Giant Branch Stars at Different Metallicities. II. The FRUITY Database. *The Astrophysical Journal Supplement*, 197(2):17, Dec. 2011. doi: 10.1088/0067-0049/197/2/17.

S. Cristallo, O. Straniero, L. Piersanti, and D. Gobrecht. Evolution, Nucleosynthesis, and Yields of AGB Stars at Different Metallicities. III. Intermediate-mass Models, Revised Low-mass Models, and the ph-FRUITY Interface. *The Astrophysical Journal Supplement*, 219(2):40, Aug. 2015. doi: 10.1088/0067-0049/219/2/40.

T. Delahaye, J. Lavalle, R. Lineros, F. Donato, and N. Fornengo. Galactic electrons and positrons at the Earth: new estimate of the primary and secondary fluxes. *Astronomy and Astrophysics*, 524:A51, Dec. 2010. doi: 10.1051/0004-6361/201014225.

F. Dell'Agli, D. A. García-Hernández, R. Schneider, P. Ventura, F. La Franca, R. Valiante, E. Marini, and M. Di Criscienzo. Asymptotic giant branch and super-asymptotic giant branch stars: modelling dust production at solar metallicity. *Monthly Notices of the Royal Astronomical Society*, 467(4):4431–4440, June 2017. doi: 10.1093/mnras/stx387.

M. Di Criscienzo, F. Dell'Agli, P. Ventura, R. Schneider, R. Valiante, F. La Franca, C. Rossi, S. Gallerani, and R. Maiolino. Dust formation in the winds of AGBs: the contribution at low metallicities. *Monthly Notices of the Royal Astronomical Society*, 433(1):313–323, July 2013. doi: 10.1093/mnras/stt732.

S. Diehl and T. S. Statler. The Hot Interstellar Medium of Normal Elliptical Galaxies. I. A Chandra Gas Gallery and Comparison of X-Ray and Optical Morphology. *The Astrophysical Journal*, 668(1):150–167, Oct. 2007. doi: 10.1086/521009.

E. A. Dorfi and H. J. Voelk. Supernova remnant dynamics and particle acceleration in elliptical galaxies. *Astronomy and Astrophysics*, 307:715–725, Mar. 1996.

B. Dorman, R. W. O'Connell, and R. T. Rood. Ultraviolet Radiation from Evolved Stellar Populations. II. The Ultraviolet Upturn Phenomenon in Elliptical Galaxies. *The Astrophysical Journal*, 442:105, Mar. 1995. doi: 10.1086/175428.

T. Doumler and A. Knebe. Investigating the influence of magnetic fields upon structure formation with AMIGA - a C code for cosmological magnetohydrodynamics. *Monthly Notices of the Royal Astronomical Society*, 403:453–473, Mar. 2010. doi: 10.1111/j.1365-2966.2009.16144.x.

B. T. Draine and A. Li. Infrared Emission from Interstellar Dust. IV. The Silicate-Graphite-PAH Model in the Post-Spitzer Era. *The Astrophysical Journal*, 657(2):810–837, Mar. 2007. doi: 10.1086/511055.

G. Dubner and E. Giacani. Radio emission from supernova remnants. *The Astronomy and Astrophysics Review*, 23:3, Sept. 2015. doi: 10.1007/s00159-015-0083-5.

C. P. Dullemond, A. Juhasz, A. Pohl, F. Sereshti, R. Shetty, T. Peters, B. Commercon, and M. Flock. RADMC-3D: A multi-purpose radiative transfer tool, Feb. 2012.

J. E. Dyson and D. A. Williams. *The physics of the interstellar medium*. Bristol: Institute of Physics Publishing, 1997. doi: 10.1201/9780585368115.

S. Eales, M. W. L. Smith, R. Auld, M. Baes, G. J. Bendo, S. Bianchi, A. Boselli, L. Ciesla, D. Clements, A. Cooray, L. Cortese, J. Davies, I. De Looze, M. Galametz, W. Gear, G. Gentile, H. Gomez, J. Fritz, T. Hughes, S. Madden, L. Magrini, M. Pohlen, L. Spinoglio, J. Verstappen, C. Vlahakis, and C. D. Wilson. Can Dust Emission be Used to Estimate the Mass of the Interstellar Medium in Galaxies—A Pilot Project with the Herschel Reference Survey. *The Astrophysical Journal*, 761(2):168, Dec. 2012. doi: 10.1088/0004-637X/761/2/168.

B. Ercolano, M. J. Barlow, P. J. Storey, and X. W. Liu. MOCASSIN: a fully three-dimensional Monte Carlo photoionization code. *Monthly Notices of the Royal Astronomical Society*, 340(4):1136–1152, Apr. 2003. doi: 10.1046/j.1365-8711.2003.06371.x.

B. Ercolano, M. J. Barlow, and P. J. Storey. The dusty MOCASSIN: fully self-consistent 3D photoionization and dust radiative transfer models. *Monthly Notices of the Royal Astronomical Society*, 362(3):1038–1046, Sept. 2005. doi: 10.1111/j.1365-2966.2005.09381.x.

C. Evoli, D. Gaggero, A. Vittino, G. Di Bernardo, M. Di Mauro, A. Ligorini, P. Ullio, and D. Grasso. Cosmic-ray propagation with DRAGON2: I. numerical solver and astrophysical ingredients. *Journal of Cosmology and Astroparticle Physics*, 2017(2):015, Feb. 2017. doi: 10.1088/1475-7516/2017/02/015.

G. J. Ferland, M. Chatzikos, F. Guzmán, M. L. Lykins, P. A. M. van Hoof, R. J. R. Williams, N. P. Abel, N. R. Badnell, F. P. Keenan, R. L. Porter, and P. C. Stancil. The 2017 Release Cloudy. *Revista Mexicana de Astronomía y Astrofísica*, 53:385–438, Oct. 2017.

K. M. Ferrière. The interstellar environment of our galaxy. *Reviews of Modern Physics*, 73:1031–1066, Oct. 2001. doi: 10.1103/RevModPhys.73.1031.

J. Franco, I. Miller, Walter Warren, S. J. Arthur, G. Tenorio-Tagle, and R. Terlevich. Thin Shell Formation in Radiative Shocks. I. Supernova Remnants in Low-Density Media. *The Astrophysical Journal*, 435:805, Nov. 1994. doi: 10.1086/174859.

H. T. Freudenreich. A COBE Model of the Galactic Bar and Disk. *The Astrophysical Journal*, 492(2):495–510, Jan. 1998. doi: 10.1086/305065.

B. Fryxell, K. Olson, P. Ricker, F. X. Timmes, M. Zingale, D. Q. Lamb, P. MacNeice, R. Rosner, J. W. Truran, and H. Tufo. FLASH: An Adaptive Mesh Hydrodynamics Code for Modeling Astrophysical Thermonuclear Flashes. *The Astrophysical Journal Supplement*, 131(1):273–334, Nov. 2000. doi: 10.1086/317361.

F. Galliano, M. Galametz, and A. P. Jones. The Interstellar Dust Properties of Nearby Galaxies. *Annual Review of Astronomy and Astrophysics*, 56:673–713, Sept. 2018. doi: 10.1146/annurev-astro-081817-051900.

M. Gaspari, F. Brighenti, and P. Temi. Mechanical AGN feedback: controlling the thermodynamical evolution of elliptical galaxies. *Monthly Notices of the Royal Astronomical Society*, 424(1):190–209, July 2012. doi: 10.1111/j.1365-2966.2012.21183.x.

M. Gavilán, J. F. Buell, and M. Mollá. Low and intermediate mass star yields: The evolution of carbon abundances. *Astronomy and Astrophysics*, 432(3):861–877, Mar. 2005. doi: 10.1051/0004-6361:20041949.

M. Gavilán, M. Mollá, and J. F. Buell. Low and intermediate mass star yields. II. The evolution of nitrogen abundances. *Astronomy and Astrophysics*, 450(2):509–521, May 2006. doi: 10.1051/0004-6361:20053590.

E. S. Gentry, M. R. Krumholz, A. Dekel, and P. Madau. Enhanced momentum feedback from clustered supernovae. *Monthly Notices of the Royal Astronomical Society*, 465:2471–2488, Feb. 2017. doi: 10.1093/mnras/stw2746.

E. S. Gentry, M. R. Krumholz, P. Madau, and A. Lupi. The momentum budget of clustered supernova feedback in a 3D, magnetized medium. *Monthly Notices of the Royal Astronomical Society*, 483:3647–3658, Mar. 2019. doi: 10.1093/mnras/sty3319.

D. R. Gies and C. T. Bolton. The binary frequency and origin of the OB runaway stars. *The Astrophysical Journal Supplement*, 61:419–454, June 1986. doi: 10.1086/191118.

A. E. Glassgold and W. D. Langer. Model calculations for diffuse molecular clouds. *The Astrophysical Journal*, 193:73–91, Oct. 1974. doi: 10.1086/153130.

O. Gnat. Time-dependent Cooling in Photoionized Plasma. *The Astrophysical Journal Supplement*, 228(2):11, Feb 2017. doi: 10.3847/1538-4365/228/2/11.

O. Gnat and A. Sternberg. Time-dependent Ionization in Radiatively Cooling Gas. *The Astrophysical Journal Supplement*, 168(2):213–230, Feb. 2007. doi: 10.1086/509786.

N. Y. Gnedin and N. Hollon. Cooling and Heating Functions of Photoionized Gas. *The Astrophysical Journal Supplement*, 202(2):13, Oct. 2012. doi: 10.1088/0067-0049/202/2/13.

D. A. Green. A catalogue of 294 Galactic supernova remnants. *Bulletin of the Astronomical Society of India*, 42(2):47–58, June 2014.

L. Greggio. The rates of type Ia supernovae. I. Analytical formulations. *Astronomy and Astrophysics*, 441(3): 1055–1078, Oct. 2005. doi: 10.1051/0004-6361:20052926.

N. Grevesse, M. Asplund, A. J. Sauval, and P. Scott. The chemical composition of the Sun. *Astrophysics and Space Science*, 328(1-2):179–183, July 2010. doi: 10.1007/s10509-010-0288-z.

J. J. Grond, R. M. Woods, J. W. Wadsley, and H. M. P. Couchman. TREVR: A general N $\log^2$N radiative transfer algorithm. *Monthly Notices of the Royal Astronomical Society*, 485(3):3681–3695, May 2019. doi: 10.1093/mnras/stz525.

B. A. Groves, E. Schinnerer, A. Leroy, M. Galametz, F. Walter, A. Bolatto, L. Hunt, D. Dale, D. Calzetti, K. Croxall, and J. Kennicutt, Robert. Dust Continuum Emission as a Tracer of Gas Mass in Galaxies. *The Astrophysical Journal*, 799(1):96, Jan. 2015. doi: 10.1088/0004-637X/799/1/96.

F. Haardt and P. Madau. Radiative Transfer in a Clumpy Universe. II. The Ultraviolet Extragalactic Background. *The Astrophysical Journal*, 461:20, Apr. 1996. doi: 10.1086/177035.

F. Haardt and P. Madau. Radiative Transfer in a Clumpy Universe. IV. New Synthesis Models of the Cosmic UV/X-Ray Background. *The Astrophysical Journal*, 746:125, Feb. 2012. doi: 10.1088/0004-637X/746/2/125.

H. J. Habing. The interstellar radiation density between 912 A and 2400 A. *Bulletin of the Astronomical Institutes of the Netherlands*, 19:421, Jan. 1968.

S. Haid, S. Walch, T. Naab, D. Seifried, J. Mackey, and A. Gatto. Supernova blast waves in wind-blown bubbles, turbulent, and power-law ambient media. *Monthly Notices of the Royal Astronomical Society*, 460:2962–2978, Aug. 2016. doi: 10.1093/mnras/stw1082.

A. A. Hakobyan, L. V. Barkhudaryan, A. G. Karapetyan, G. A. Mamon, D. Kunth, V. Adibekyan, L. S. Aramyan, A. R. Petrosian, and M. Turatto. Supernovae and their host galaxies - V. The vertical distribution of supernovae in disc galaxies. *Monthly Notices of the Royal Astronomical Society*, 471(2):1390–1400, Oct. 2017. doi: 10.1093/mnras/stx1608.

O. Iffrig and P. Hennebelle. Mutual influence of supernovae and molecular clouds. *Astronomy and Astrophysics*, 576:A95, Apr. 2015. doi: 10.1051/0004-6361/201424556.

N. Indriolo, T. R. Geballe, T. Oka, and B. J. McCall. H^+_3 in Diffuse Interstellar Clouds: A Tracer for the Cosmic-Ray Ionization Rate. *The Astrophysical Journal*, 671(2):1736–1747, Dec. 2007. doi: 10.1086/523036.

K. Iwamoto, F. Brachwitz, K. Nomoto, N. Kishimoto, H. Umeda, W. R. Hix, and F.-K. Thielemann. Nucleosynthesis in Chandrasekhar Mass Models for Type IA Supernovae and Constraints on Progenitor Systems and Burning-Front Propagation. *The Astrophysical Journal Supplement*, 125(2):439–462, Dec. 1999. doi: 10.1086/313278.

S. Jiménez, G. Tenorio-Tagle, and S. Silich. The full evolution of supernova remnants in low- and high-density ambient media. *Monthly Notices of the Royal Astronomical Society*, 488(1):978–990, Sept. 2019. doi: 10.1093/mnras/stz1749.

H. M. Johnson and J. M. MacLeod. The Spatial Distribution of Supernovae in Galaxies. *Publications of the Astronomical Society of the Pacific*, 75(443):123, Apr. 1963. doi: 10.1086/127915.

P. Jonsson. SUNRISE: polychromatic dust radiative transfer in arbitrary geometries. *Monthly Notices of the Royal Astronomical Society*, 372(1):2–20, Oct. 2006. doi: 10.1111/j.1365-2966.2006.10884.x.

J.-h. Kang, B.-C. Koo, and C. Salter. An Old Supernova Remnant within an H II Complex at l $\approx$ 173°: FVW 172.8+1.5. *The Astronomical Journal*, 143(3):75, Mar. 2012. doi: 10.1088/0004-6256/143/3/75.

B. W. Keller, J. Wadsley, S. M. Benincasa, and H. M. P. Couchman. A superbubble feedback model for galaxy simulations. *Monthly Notices of the Royal Astronomical Society*, 442:3013–3025, Aug. 2014. doi: 10.1093/mnras/stu1058.

C.-G. Kim and E. C. Ostriker. Momentum Injection by Supernovae in the Interstellar Medium. *The Astrophysical Journal*, 802:99, Apr. 2015. doi: 10.1088/0004-637X/802/2/99.

C.-G. Kim, E. C. Ostriker, and R. Raileanu. Superbubbles in the Multiphase ISM and the Loading of Galactic Winds. *The Astrophysical Journal*, 834:25, Jan. 2017. doi: 10.3847/1538-4357/834/1/25.

V. V. Korolev, E. O. Vasiliev, I. G. Kovalenko, and Y. A. Shchekinov. Dynamics of a supernova envelope in a cloudy interstellar medium. *Astronomy Reports*, 59(7):690–708, July 2015. doi: 10.1134/S1063772915070057.

B. Körtgen, D. Seifried, R. Banerjee, E. Vázquez-Semadeni, and M. Zamora-Avilés. Supernova feedback in molecular clouds: global evolution and dynamics. *Monthly Notices of the Royal Astronomical Society*, 459 (4):3460–3474, July 2016. doi: 10.1093/mnras/stw824.

H. Koyama and S.-i. Inutsuka. An Origin of Supersonic Motions in Interstellar Clouds. *The Astrophysical Journal*, 564(2):L97–L100, Jan 2002. doi: 10.1086/338978.

P. Kroupa. On the variation of the initial mass function. *Monthly Notices of the Royal Astronomical Society*, 322(2):231–246, Apr. 2001. doi: 10.1046/j.1365-8711.2001.04022.x.

A. Kurganov, S. Noelle, and G. Petrova. Semidiscrete central-upwind schemes for hyperbolic conservation laws and hamilton–jacobi equations. *SIAM J. Sci. Comput.*, 23(3):707–740, Mar. 2001. ISSN 1064-8275. doi: 10.1137/S1064827500373413. URL http://dx.doi.org/10.1137/S1064827500373413.

D. A. Leahy and J. E. Williams. A Python Calculator for Supernova Remnant Evolution. *The Astronomical Journal*, 153:239, May 2017. doi: 10.3847/1538-3881/aa6af6.

J. H. Lee and M. G. Lee. A New Optical Survey of Supernova Remnant Candidates in M31. *The Astrophysical Journal*, 786(2):130, May 2014a. doi: 10.1088/0004-637X/786/2/130.

J. H. Lee and M. G. Lee. Properties of Optically Selected Supernova Remnant Candidates in M33. *The Astrophysical Journal*, 793(2):134, Oct. 2014b. doi: 10.1088/0004-637X/793/2/134.

I. Leonidaki, A. Zezas, and P. Boumis. A Multiwavelength Study of Supernova Remnants in Six Nearby Galaxies. I. Detection of New X-ray-selected Supernova Remnants with Chandra. *The Astrophysical Journal*, 725(1): 842–867, Dec. 2010. doi: 10.1088/0004-637X/725/1/842.

A. K. Leroy, F. Walter, E. Brinks, F. Bigiel, W. J. G. de Blok, B. Madore, and M. D. Thornley. The Star Formation Efficiency in Nearby Galaxies: Measuring Where Gas Forms Stars Effectively. *The Astronomical Journal*, 136:2782–2845, Dec. 2008. doi: 10.1088/0004-6256/136/6/2782.

M. Li, J. P. Ostriker, R. Cen, G. L. Bryan, and T. Naab. Supernova Feedback and the Hot Gas Filling Fraction of the Interstellar Medium. *The Astrophysical Journal*, 814:4, Nov. 2015. doi: 10.1088/0004-637X/814/1/4.

M. Limongi and A. Chieffi. Presupernova Evolution and Explosive Nucleosynthesis of Rotating Massive Stars in the Metallicity Range -3 $\leq$ [Fe/H] $\leq$ 0. *The Astrophysical Journal Supplement*, 237(1):13, July 2018. doi: 10.3847/1538-4365/aacb24.

K. S. Long, W. P. Blair, P. F. Winkler, R. H. Becker, T. J. Gaetz, P. Ghavamian, D. J. Helfand, J. P. Hughes, R. P. Kirshner, K. D. Kuntz, E. K. McNeil, T. G. Pannuti, P. P. Plucinsky, D. Saul, R. Tüllmann, and B. Williams. The Chandra ACIS Survey of M33: X-ray, Optical, and Radio Properties of the Supernova Remnants. *The Astrophysical Journal Supplement*, 187(2):495–559, Apr. 2010. doi: 10.1088/0067-0049/187/2/495.

Z.-J. Lu, V.-M. Pelkonen, P. Padoan, L. Pan, T. Haugbølle, and Å. Nordlund. The Effect of Supernovae on the Turbulence and Dispersal of Molecular Clouds. *The Astrophysical Journal*, 904(1):58, Nov. 2020. doi: 10.3847/1538-4357/abbd8f.

W. E. Lucas, I. A. Bonnell, and J. E. Dale. Supernova feedback and the energy deposition in molecular clouds. *Monthly Notices of the Royal Astronomical Society*, 493(4):4700–4710, Apr. 2020. doi: 10.1093/mnras/staa451.

F. Mannucci, D. Maoz, K. Sharon, M. T. Botticella, M. Della Valle, A. Gal-Yam, and N. Panagia. The supernova rate in local galaxy clusters. *Monthly Notices of the Royal Astronomical Society*, 383(3):1121–1130, Jan. 2008. doi: 10.1111/j.1365-2966.2007.12603.x.

D. Maoz and F. Mannucci. Type-Ia Supernova Rates and the Progenitor Problem: A Review. *Publications of the Astronomical Society of Australia*, 29(4):447–465, Jan. 2012. doi: 10.1071/AS11052.

D. Maoz, E. Waxman, and A. Loeb. The Remnants of Intergalactic Supernovae. *The Astrophysical Journal*, 632(2):847–853, Oct. 2005. doi: 10.1086/433174.

D. Maoz, F. Mannucci, and G. Nelemans. Observational Clues to the Progenitors of Type Ia Supernovae. *Annual Review of Astronomy and Astrophysics*, 52:107–170, Aug. 2014. doi: 10.1146/annurev-astro-082812-141031.

S. Marassi, R. Schneider, M. Limongi, A. Chieffi, M. Bocchio, and S. Bianchi. The metal and dust yields of the first massive stars. *Monthly Notices of the Royal Astronomical Society*, 454(4):4250–4266, Dec. 2015. doi: 10.1093/mnras/stv2267.

S. Martínez-González, R. Wünsch, J. Palouš, C. Muñoz-Tuñón, S. Silich, and G. Tenorio-Tagle. Pyroclastic Blowout: Dust Survival in Isolated versus Clustered Supernovae. *The Astrophysical Journal*, 866(1):40, Oct. 2018. doi: 10.3847/1538-4357/aadb88.

S. Martínez-González, R. Wünsch, S. Silich, G. Tenorio-Tagle, J. Palouš, and A. Ferrara. Supernovae within Pre-existing Wind-blown Bubbles: Dust Injection versus Ambient Dust Destruction. *The Astrophysical Journal*, 887(2):198, Dec. 2019. doi: 10.3847/1538-4357/ab571b.

D. Martizzi, C.-A. Faucher-Giguère, and E. Quataert. Supernova feedback in an inhomogeneous interstellar medium. *Monthly Notices of the Royal Astronomical Society*, 450:504–522, June 2015. doi: 10.1093/mnras/stv562.

W. G. Mathews and J. C. Baker. Galactic Winds. *The Astrophysical Journal*, 170:241, Dec. 1971. doi: 10.1086/151208.

W. G. Mathews and F. Brighenti. Hot Gas in and around Elliptical Galaxies. *Annual Review of Astronomy and Astrophysics*, 41:191–239, Jan. 2003. doi: 10.1146/annurev.astro.41.090401.094542.

J. S. Mathis, P. G. Mezger, and N. Panagia. Interstellar radiation field and dust temperatures in the diffuse interstellar matter and in giant molecular clouds. *Astronomy and Astrophysics*, 500:259–276, Nov. 1983.

B. C. Matthews, B. J. Wallace, and A. R. Taylor. G55.0+0.3: A Highly Evolved Supernova Remnant. *The Astrophysical Journal*, 493(1):312–325, Jan. 1998. doi: 10.1086/305112.

C. F. McKee and J. P. Ostriker. A theory of the interstellar medium: three components regulated by supernova explosions in an inhomogeneous substrate. *The Astrophysical Journal*, 218:148–169, Nov. 1977. doi: 10.1086/155667.

I. Millán-Irigoyen, M. Mollá, and Y. Ascasibar. Chemical evolution of galaxies: emerging dust and the different gas phases in a new multiphase code. *Monthly Notices of the Royal Astronomical Society*, 494(1):146–160, May 2020. doi: 10.1093/mnras/staa635.

I. Millán-Irigoyen, M. Mollá, M. Cerviño, Y. Ascasibar, M. L. García-Vargas, and P. R. T. Coelho. HR-PYPOPSTAR: high-wavelength-resolution stellar populations evolutionary synthesis model. *Monthly Notices of the Royal Astronomical Society*, 506(4):4781–4799, Oct. 2021. doi: 10.1093/mnras/stab1969.

M. Mollá, M. L. García-Vargas, and A. Bressan. PopStar I: evolutionary synthesis model description. *Monthly Notices of the Royal Astronomical Society*, 398(1):451–470, Sept. 2009. doi: 10.1111/j.1365-2966.2009.15160.x.

M. Mollá, O. Cavichia, M. Gavilán, and B. K. Gibson. Galactic chemical evolution: stellar yields and the initial mass function. *Monthly Notices of the Royal Astronomical Society*, 451(4):3693–3708, Aug. 2015. doi: 10.1093/mnras/stv1102.

M. Mollá, Á. I. Díaz, B. K. Gibson, O. Cavichia, and Á.-R. López-Sánchez. The role of gas infall in the evolution of disc galaxies. *Monthly Notices of the Royal Astronomical Society*, 462(2):1329–1340, Oct. 2016. doi: 10.1093/mnras/stw1723.

M. Mollá, Á. I. Díaz, Y. Ascasibar, and B. K. Gibson. Galaxy chemical evolution models: the role of molecular gas formation. *Monthly Notices of the Royal Astronomical Society*, 468:305–318, June 2017. doi: 10.1093/mnras/stx419.

M. Mollá, O. Cavichia, J. J. Bazán, A. Castrillo, Y. Ascasibar, L. Galbany, I. Millán-Irigoyen, and Á. Díaz. Chemical evolution models: Supernova rates, [α/Fe] abundances, and their variations is time and space. to be submitted, 2022.

T. Naab and J. P. Ostriker. Theoretical Challenges in Galaxy Formation. *Annual Review of Astronomy and Astrophysics*, 55:59–109, Aug. 2017. doi: 10.1146/annurev-astro-081913-040019.

G. Natale, C. C. Popescu, M. Rushton, R. Yang, J. J. Thirlwall, and D. Pricopi. A radiation transfer model for the Milky Way: II. The global properties and large-scale structure. *Monthly Notices of the Royal Astronomical Society*, 509(2):2339–2361, Jan. 2022. doi: 10.1093/mnras/stab2771.

U. M. Noebauer and S. A. Sim. Monte Carlo radiative transfer. *Living Reviews in Computational Astrophysics*, 5(1):1, June 2019. doi: 10.1007/s41115-019-0004-9.

T. Nozawa, K. Maeda, T. Kozasa, M. Tanaka, K. Nomoto, and H. Umeda. Formation of Dust in the Ejecta of Type Ia Supernovae. *The Astrophysical Journal*, 736(1):45, July 2011. doi: 10.1088/0004-637X/736/1/45.

A. Obreja, A. V. Macciò, B. Moster, S. M. Udrescu, T. Buck, R. Kannan, A. A. Dutton, and M. Blank. Local photoionization feedback effects on galaxies. *Monthly Notices of the Royal Astronomical Society*, 490(2): 1518–1538, Dec. 2019. doi: 10.1093/mnras/stz2639.

T. Okamoto, I. Shimizu, and N. Yoshida. Reproducing cosmic evolution of galaxy population from z = 4 to 0. *Publications of the Astronomical Society of Japan*, 66(4):70, July 2014. doi: 10.1093/pasj/psu046.

J. H. Oort. Interaction of Nova and Supernova Shells With the Interstellar Medium. In *Problems of Cosmical Aerodynamics*, page 118, Jan. 1951.

B. D. Oppenheimer and J. Schaye. Non-equilibrium ionization and cooling of metal-enriched gas in the presence of a photoionization background. *Monthly Notices of the Royal Astronomical Society*, 434(2):1043–1062, Sept. 2013. doi: 10.1093/mnras/stt1043.

J. P. Ostriker and C. F. McKee. Astrophysical blastwaves. *Reviews of Modern Physics*, 60:1–68, 1988. doi: 10.1103/RevModPhys.60.1.

T. Padmanabhan. *Theoretical Astrophysics - Volume 1, Astrophysical Processes*, volume 1. Cambridge University Press, 2000. doi: 10.2277/0521562406.

O. Petruk, T. Kuzyo, and V. Beshley. Post-adiabatic supernova remnants in an interstellar magnetic field: parallel and perpendicular shocks. *Monthly Notices of the Royal Astronomical Society*, 456:2343–2353, Mar. 2016. doi: 10.1093/mnras/stv2746.

O. Petruk, T. Kuzyo, S. Orlando, M. Pohl, M. Miceli, F. Bocchino, V. Beshley, and R. Brose. Post-adiabatic supernova remnants in an interstellar magnetic field: oblique shocks and non-uniform environment. *Monthly Notices of the Royal Astronomical Society*, 479:4253–4270, Sept. 2018. doi: 10.1093/mnras/sty1750.

C. Pfrommer, R. Pakmor, K. Schaal, C. M. Simpson, and V. Springel. Simulating cosmic ray physics on a moving mesh. *Monthly Notices of the Royal Astronomical Society*, 465:4500–4529, Mar. 2017. doi: 10.1093/mnras/stw2941.

S. Pineault and G. Joncas. G106.3+2.7: A Supernova Remnant in a Late Stage of Evolution. *The Astronomical Journal*, 120(6):3218–3225, Dec. 2000. doi: 10.1086/316863.

J. M. Pittard. Momentum and energy injection by a supernova remnant into an inhomogeneous medium. *arXiv e-prints*, art. arXiv:1907.03519, Jul 2019.

J. M. Pittard, M. S. Dobson, R. H. Durisen, J. E. Dyson, T. W. Hartquist, and J. T. O'Brien. The shocking properties of supersonic flows: Dependence of the thermal overstability on M, α, and T_c / T_0. *Astronomy and Astrophysics*, 438(1):11–21, July 2005. doi: 10.1051/0004-6361:20042260.

S. Ploeckinger and J. Schaye. Radiative cooling rates, ion fractions, molecule abundances, and line emissivities including self-shielding and both local and metagalactic radiation fields. *Monthly Notices of the Royal Astronomical Society*, 497(4):4857–4883, Oct. 2020. doi: 10.1093/mnras/staa2172.

C. C. Popescu and R. J. Tuffs. Radiation fields in star-forming galaxies: the disc, thin disc and bulge. *Monthly Notices of the Royal Astronomical Society*, 436(2):1302–1321, Dec. 2013. doi: 10.1093/mnras/stt1666.

C. C. Popescu, R. Yang, R. J. Tuffs, G. Natale, M. Rushton, and F. Aharonian. A radiation transfer model for the Milky Way: I. Radiation fields and application to high-energy astrophysics. *Monthly Notices of the Royal Astronomical Society*, 470(3):2539–2558, Sept. 2017. doi: 10.1093/mnras/stx1282.

T. A. Porter and A. W. Strong. A new estimate of the Galactic interstellar radiation field between 0.1um and 1000um. In *29th International Cosmic Ray Conference (ICRC29), Volume 4*, volume 4 of *International Cosmic Ray Conference*, page 77, Jan. 2005.

T. A. Porter, G. Jóhannesson, and I. V. Moskalenko. High-energy Gamma Rays from the Milky Way: Three-dimensional Spatial Models for the Cosmic-Ray and Radiation Field Densities in the Interstellar Medium. *The Astrophysical Journal*, 846(1):67, Sept. 2017. doi: 10.3847/1538-4357/aa844d.

F. D. Priestley, H. Chawner, M. Matsuura, I. De Looze, M. J. Barlow, and H. L. Gomez. Revisiting the dust destruction efficiency of supernovae. *Monthly Notices of the Royal Astronomical Society*, 500(2):2543–2553, Jan. 2021. doi: 10.1093/mnras/staa3445.

A. C. Raga, J. Cantó, L. F. Rodríguez, and P. F. Velázquez. An analytic model for the strong-/weak-shock transition in a spherical blast wave. *Monthly Notices of the Royal Astronomical Society*, 424:2522–2527, Aug. 2012. doi: 10.1111/j.1365-2966.2012.21208.x.

W. T. Reach, J. Rho, A. Tappe, T. G. Pannuti, C. L. Brogan, E. B. Churchwell, M. R. Meade, B. Babler, R. Indebetouw, and B. A. Whitney. A Spitzer Space Telescope Infrared Survey of Supernova Remnants in the Inner Galaxy. *The Astronomical Journal*, 131(3):1479–1500, Mar. 2006. doi: 10.1086/499306.

D. Robinson, C. Avestruz, and N. Y. Gnedin. Do cooling and heating functions actually exist? *arXiv e-prints*, art. arXiv:2109.01674, Sept. 2021.

T. P. Robitaille. HYPERION: an open-source parallelized three-dimensional dust continuum radiative transfer code. *Astronomy and Astrophysics*, 536:A79, Dec. 2011. doi: 10.1051/0004-6361/201117150.

T. P. Robitaille, E. Churchwell, R. A. Benjamin, B. A. Whitney, K. Wood, B. L. Babler, and M. R. Meade. A self-consistent model of Galactic stellar and dust infrared emission and the abundance of polycyclic aromatic hydrocarbons. *Astronomy and Astrophysics*, 545:A39, Sept. 2012. doi: 10.1051/0004-6361/201219073.

M. Romero, Y. Ascasibar, J. Palouš, R. Wünsch, and M. Mollá. Impact of the ERF on the structure and evolution of SNRs. *Monthly Notices of the Royal Astronomical Society*, 505(4):5301–5310, Aug. 2021. doi: 10.1093/mnras/stab1660.

M. Romero, P. Corcho-Caballero, I. Millán-Irigoyen, M. Mollá, and Y. Ascasibar. Predicting interstellar radiation fields from chemical evolution models. *arXiv e-prints*, art. arXiv:2203.04782, Mar. 2022.

D. Ryu, J. P. Ostriker, H. Kang, and R. Cen. A cosmological hydrodynamic code based on the total variation diminishing scheme. *The Astrophysical Journal*, 414:1–19, Sept. 1993. doi: 10.1086/173051.

P. Salucci, A. Lapi, C. Tonini, G. Gentile, I. Yegorova, and U. Klein. The universal rotation curve of spiral galaxies - II. The dark matter distribution out to the virial radius. *Monthly Notices of the Royal Astronomical Society*, 378(1):41–47, June 2007. doi: 10.1111/j.1365-2966.2007.11696.x.

K. C. Sarkar, O. Gnat, and A. Sternberg. Non-equilibrium ionisation and radiative transport in an evolving supernova remnant. *Monthly Notices of the Royal Astronomical Society*, Mar. 2021. doi: 10.1093/mnras/stab582.

M. Sasaki, W. Pietsch, F. Haberl, D. Hatzidimitriou, H. Stiele, B. Williams, A. Kong, and U. Kolb. Supernova remnants and candidates detected in the XMM-Newton M 31 large survey. *Astronomy and Astrophysics*, 544:A144, Aug. 2012. doi: 10.1051/0004-6361/201219025.

S. Y. Sazonov, J. P. Ostriker, L. Ciotti, and R. A. Sunyaev. Radiative feedback from quasars and the growth of massive black holes in stellar spheroids. *Monthly Notices of the Royal Astronomical Society*, 358(1):168–180, Mar. 2005. doi: 10.1111/j.1365-2966.2005.08763.x.

K. Schaal and V. Springel. Shock finding on a moving mesh - I. Shock statistics in non-radiative cosmological simulations. *Monthly Notices of the Royal Astronomical Society*, 446:3992–4007, Feb. 2015. doi: 10.1093/mnras/stu2386.

L. I. Sedov. *Similarity and Dimensional Methods in Mechanics*. New York: Academic Press, 1959.

P. Sharma, A. Roy, B. B. Nath, and Y. Shchekinov. In a hot bubble: why does superbubble feedback work, but isolated supernovae do not? *Monthly Notices of the Royal Astronomical Society*, 443:3463–3476, Oct. 2014. doi: 10.1093/mnras/stu1307.

J. D. Slavin, E. Dwek, and A. P. Jones. Destruction of Interstellar Dust in Evolving Supernova Remnant Shock Waves. *The Astrophysical Journal*, 803:7, Apr. 2015. doi: 10.1088/0004-637X/803/1/7.

B. D. Smith, G. L. Bryan, S. C. O. Glover, N. J. Goldbaum, M. J. Turk, J. Regan, J. H. Wise, H.-Y. Schive, T. Abel, A. Emerick, B. W. O'Shea, P. Anninos, C. B. Hummels, and S. Khochfar. GRACKLE: a chemistry and cooling library for astrophysics. *Monthly Notices of the Royal Astronomical Society*, 466:2217–2234, Apr. 2017. doi: 10.1093/mnras/stw3291.

G. A. Sod. A survey of several finite difference methods for systems of nonlinear hyperbolic conservation laws. *Journal of Computational Physics*, 27(1):1–31, 1978. ISSN 0021-9991. doi: https://doi.org/10.1016/0021-9991(78)90023-2. URL https://www.sciencedirect.com/science/article/pii/0021999178900232.

V. Springel. High Performance Computing and Numerical Modelling. *Saas-Fee Advanced Course*, 43:251, Jan. 2016. doi: 10.1007/978-3-662-47890-5_3.

J. Steinacker, M. Baes, and K. D. Gordon. Three-Dimensional Dust Radiative Transfer*. *Annual Review of Astronomy and Astrophysics*, 51(1):63–104, Aug. 2013. doi: 10.1146/annurev-astro-082812-141042.

S. Tang and Q. D. Wang. Supernova Blast Waves in Low-Density Hot Media: A Mechanism for Spatially Distributed Heating. *The Astrophysical Journal*, 628:205–209, July 2005. doi: 10.1086/430875.

G. Taylor. The Formation of a Blast Wave by a Very Intense Explosion. I. Theoretical Discussion. *Proceedings of the Royal Society of London Series A*, 201:159–174, Mar. 1950. doi: 10.1098/rspa.1950.0049.

K. Thornton, M. Gaudlitz, H.-T. Janka, and M. Steinmetz. Energy Input and Mass Redistribution by Supernovae in the Interstellar Medium. *The Astrophysical Journal*, 500:95–119, June 1998. doi: 10.1086/305704.

J. K. Truelove and C. F. McKee. Evolution of Nonradiative Supernova Remnants. *The Astrophysical Journal Supplement*, 120:299–326, Feb. 1999. doi: 10.1086/313176.

B. van Leer. Towards the Ultimate Conservative Difference Scheme. IV. A New Approach to Numerical Convection. *Journal of Computational Physics*, 23:276, Mar. 1977. doi: 10.1016/0021-9991(77)90095-X.

E. O. Vasiliev. Non-equilibrium cooling rate for a collisionally cooled metal-enriched gas. *Monthly Notices of the Royal Astronomical Society*, 431(1):638–647, May 2013. doi: 10.1093/mnras/stt189.

P. Ventura, M. di Criscienzo, R. Schneider, R. Carini, R. Valiante, F. D'Antona, S. Gallerani, R. Maiolino, and A. Tornambé. The transition from carbon dust to silicate production in low-metallicity asymptotic giant branch and super-asymptotic giant branch stars. *Monthly Notices of the Royal Astronomical Society*, 420(2): 1442–1456, Feb. 2012a. doi: 10.1111/j.1365-2966.2011.20129.x.

P. Ventura, M. di Criscienzo, R. Schneider, R. Carini, R. Valiante, F. D'Antona, S. Gallerani, R. Maiolino, and A. Tornambé. Dust formation around AGB and SAGB stars: a trend with metallicity? *Monthly Notices of the Royal Astronomical Society*, 424(3):2345–2357, Aug. 2012b. doi: 10.1111/j.1365-2966.2012.21403.x.

E. T. Vishniac and D. Ryu. On the Stability of Decelerating Shocks. *The Astrophysical Journal*, 337:917, Feb. 1989. doi: 10.1086/167161.

S. Walch and T. Naab. The energy and momentum input of supernova explosions in structured and ionized molecular clouds. *Monthly Notices of the Royal Astronomical Society*, 451:2757–2771, Aug. 2015. doi: 10.1093/mnras/stv1155.

S. Wang and E. Johnsen. High-order schemes for the Euler equations in cylindrical/spherical coordinates. *ArXiv e-prints*, Jan. 2017.

R. P. C. Wiersma, J. Schaye, and B. D. Smith. The effect of photoionization on the cooling rates of enriched, astrophysical plasmas. *Monthly Notices of the Royal Astronomical Society*, 393(1):99–107, Feb. 2009. doi: 10.1111/j.1365-2966.2008.14191.x.

J. H. Wise, T. Abel, M. J. Turk, M. L. Norman, and B. D. Smith. The birth of a galaxy - II. The role of radiation pressure. *Monthly Notices of the Royal Astronomical Society*, 427(1):311–326, Nov. 2012. doi: 10.1111/j.1365-2966.2012.21809.x.

M. G. Wolfire, D. Hollenbach, C. F. McKee, A. G. G. M. Tielens, and E. L. O. Bakes. The Neutral Atomic Phases of the Interstellar Medium. *The Astrophysical Journal*, 443:152, Apr. 1995. doi: 10.1086/175510.

S. E. Woosley and T. A. Weaver. The Evolution and Explosion of Massive Stars. II. Explosive Hydrodynamics and Nucleosynthesis. *The Astrophysical Journal Supplement*, 101:181, Nov. 1995. doi: 10.1086/192237.

R. Wünsch, S. Walch, F. Dinnbier, D. Seifried, S. Haid, A. Klepitko, A. P. Whitworth, and J. Palouš. Tree-based solvers for adaptive mesh refinement code FLASH - II: radiation transport module TreeRay. *Monthly Notices of the Royal Astronomical Society*, 505(3):3730–3754, Aug. 2021. doi: 10.1093/mnras/stab1482.

L. Xiao and M. Zhu. GSH 90-28-17: a possible old supernova remnant. *Monthly Notices of the Royal Astronomical Society*, 438(2):1081–1088, Feb. 2014. doi: 10.1093/mnras/stt2258.

U. Ziegler. A central-constrained transport scheme for ideal magnetohydrodynamics. *Journal of Computational Physics*, 196:393–416, May 2004. doi: 10.1016/j.jcp.2003.11.003.

U. Ziegler. Self-gravitational adaptive mesh magnetohydrodynamics with the NIRVANA code. *Astronomy and Astrophysics*, 435:385–395, May 2005. doi: 10.1051/0004-6361:20042451.

Appendix A

Default Cloudy Abundances used in this Thesis

Table A.1 shows default abundances and depletion factors used in this chapter. These values, and references for each number, can be found in Tables 7.4 and 7.8 of CLOUDY documentation, hazy 1. For the case of `abundances gass`, CLOUDY data is based on Grevesse et al. (2010) distribution. In addition, you can also reproduce these values, except the depletion factors, by running CLOUDY with the input displayed in Table A.2

Element	`abundances gass`	`abundances ism`	Depletion factor
H	0.00	0.00	≈ 0.00
He	−1.07	−1.01	0.00
Li	−10.95	−10.27	−0.08
Be	−10.62	−35.93	−0.22
B	−9.30	−10.05	−0.89
C	−3.57	−3.60	−0.40
N	−4.17	−4.10	0.00
O	−3.31	−3.50	−0.22
F	−7.44	−7.70	−0.52
Ne	−4.07	−3.91	0.00
Na	−5.76	−6.50	−0.70
Mg	−4.40	−4.90	−0.70
Al	−5.55	−7.10	−2.00
Si	−4.49	−5.50	−1.52
P	−6.59	−6.80	−0.60
S	−4.88	−4.49	0.00
Cl	−6.50	−7.00	−0.40
Ar	−5.60	−5.55	0.00
K	−6.97	−7.96	−0.52
Ca	−5.66	−9.39	−4.0
Sc	−8.85	−35.93	−2.30
Ti	−7.05	−9.24	−2.10
V	−8.07	−10.00	−2.22
Cr	−6.36	−8.00	−2.22
Mn	−6.57	−7.64	−1.30
Fe	−4.50	−6.20	−2.00
Co	−7.01	−8.23	−2.00
Ni	−5.78	−7.74	−2.00
Cu	−7.81	−8.82	−1.00
Zn	−7.44	−7.70	−0.60
DTG	−2.18	−2.19	
q_{PAH}	−2.40	−2.40	

Table A.1: Decimal logarithm of different magnitudes. Second and third columns are number densities considered under the `abundances ...` command, for $n_H = 1.0\ cm^{-3}$. Fourth column is the depletion factor of chemical elements into grains (i.e.: fraction of mass that *remains* in gaseous phase). Last two rows are the default values of the dust-to-gas and pah-to-dust ratios, which are also included for completeness.

Commands	Comments
`# INPUT`	
`hden 0`	$n_{H,0} = 1$ cm^{-3}
`abundances gass`	Change for `abundances ism no grains` for the other column.
`grains ism`	Adds grains proper of the Galactic ISM
`grains pah`	Adds Polycyclic Aromatic Hydrocarbons (PAH)
`set pah constant`	distributes PAH uniformly across the cloud
`table ism`	Interstellar radiation field
`# OUTPUT`	
`stop zone 1`	Stops the calculation after first subregion in the cloud
`save abundances "composition.txt" last`	Generates second (third) column in Table A.1
`save grain D/G ratio "DTG.txt" last units nm`	Generates last two rows of Table A.1

Table A.2: CLOUDY input needed to create most of Table A.1.

Appendix B

Adiabatic Spherical Blastwaves

A spherical blastwave is a shock that has been generated by a point source (e.g.: an explosion) and, because of geometry, you can establish a shock radius $R(t)$. These entities are a bit more complex than typical shocks that you can encounter in textbooks because these leave a spherical cavity inside R with some particularities in the structure which, for the case of SNR, it is relevant as it is a source of hot ISM gas.

B.1 Shock jump conditions

A shock consists in a sharp jump in all hydrodynamic magnitudes that, in case of the Euler equations (3.1)-(3.3), are mathematical discontinuities. In that regard, you can solve exactly for the particular case of a shock with velocity $v_s = \frac{dR}{dt}$ that separates its close surroundings into a pre-shock (or ambient) medium with (ρ_0, v_0, P_0) and the post-shock material (ρ_1, v_1, P_1).

For an adiabatic shock-wave, fluxes (3.9) of mass, momentum and energy are conserved. In the rest frame of the shock (i.e.: any velocity is related with v_0 and v_1 as $v' = v - v_s$), this means

$$\rho_0 v_0' = \rho_1 v_1' \tag{B.1}$$

$$\rho_0 {v_0'}^2 + P_0 = \rho_1 {v_1'}^2 + P_1 \tag{B.2}$$

$$v_0'(\epsilon_0 + P_0) = v_1'(\epsilon_1 + P_1) \tag{B.3}$$

where ϵ is the total energy density of the gas

$$\epsilon = \frac{1}{2}\rho v^2 + \frac{P}{(\gamma - 1)} \tag{B.4}$$

Note that this is (3.4) with energy as its left-hand term. Then, you can find a solution for $\{\rho_1, v_1, P_1\}$, assuming that $v_0 = 0$

$$\rho_1 = \tfrac{(\gamma+1)}{(\gamma-1)+2\mathcal{M}^{-2}}\rho_0 \tag{B.5}$$

$$v_1 = \tfrac{2}{\gamma+1}(1 - \mathcal{M}^{-2})v_s \tag{B.6}$$

$$P_1 = [1 + \tfrac{2\gamma}{\gamma+1}(\mathcal{M}^2 - 1)]P_0 \tag{B.7}$$

where $\mathcal{M}$ is the Mach number (2.1). These equations are the Rankine-Hugoniot conditions.

A very useful simplification comes for strong shocks, giving

$$\rho_1 = \tfrac{\gamma+1}{\gamma-1}\rho_0 \tag{B.8}$$

$$v_1 = \tfrac{2}{\gamma+1}v_s \tag{B.9}$$

$$P_1 = \tfrac{2\gamma}{\gamma+1}\mathcal{M}^2 P_0 = \tfrac{2}{\gamma+1}\rho_0 v_s^2 \tag{B.10}$$

From here, we can deduce two important properties to take advantage. First, post-shock density always saturates to a constant number (e.g.: to $4\rho_0$ for $\gamma = \frac{5}{3}$). Second, the other two quantities, v_1 and P_1, has a linear and quadratic dependence, respectively, with shock velocity v_s.

B.2 Internal structure

In order to obtain a solution for the internal structure, it is common to search for self-similar solutions of Euler equations, that is:

$$y(r,t) = \Xi(r)\Upsilon(t) \tag{B.11}$$

where y is an arbitrary hydrodynamic quantity, with a similar meaning as found in Chapter 3.

In general, Euler equations (3.1)-(3.3) do not accept these kind of solutions. Nevertheless, we can still try to find approximate solutions from (B.11). Following the methodology of Ostriker and McKee (1988) to derive approximate radial profiles, we can take an ansatz for density, velocity and pressure:

$$\rho = \rho_1[(1-\rho_3) + \rho_3 \hat{r}^{\rho_2}] \tag{B.12}$$
$$v = v_1 \hat{r} \tag{B.13}$$
$$P = P_1[(1-P_3) + P_3 \hat{r}^{P_2}] \tag{B.14}$$

where $\hat{r} = \frac{r}{R}$, and $\{\rho_1, v_1, P_1\}$ are the post-shock values reigned by the Rankine-Hugoniot conditions (B.8)-(B.10). Those expressions imply that we can write the suggested radial profiles as

$$y(r,t) = \Upsilon(v_s(t))\Xi(\hat{r}) \propto v_s^{\sigma}\ \Xi(\hat{r}) \tag{B.15}$$

where $\sigma = \{0, 1, 2\}$ for $y = \{\rho, v, P\}$.

The other four parameters of ρ and P are unknowns to be derived from four equations. First two comes from the mean density and pressure of the sphere with radius R:

$$\bar{\rho} = \frac{1}{V}\int_V \rho dV = 3\int_0^1 \rho(\hat{r})\hat{r}^2 d\hat{r} = 3\rho_1[\tfrac{1-\rho_3}{3} + \tfrac{\rho_3}{\rho_2+3}] \tag{B.16}$$
$$\bar{P} = \frac{1}{V}\int_V P dV = 3\int_0^1 P(\hat{r})\hat{r}^2 d\hat{r} = 3P_1[\tfrac{1-P_3}{3} + \tfrac{P_3}{P_2+3}] \tag{B.17}$$
$$\tag{B.18}$$

and both $\bar{\rho}$ and $\bar{P}$ are related with ISM swept-up mass and thermal energy, or pre-shock values, labelled with subindex 0

$$\bar{\rho} = \frac{M}{V} = \rho_0 \tag{B.19}$$
$$\bar{P} = \frac{E_{th}}{V}(\gamma - 1) = \frac{3E_0}{4\pi R^3}\varepsilon_{th}(\gamma - 1) \tag{B.20}$$

where $\varepsilon_{th} \simeq 0.717$. In particular, it is useful to compute $\frac{\bar{P}}{P_1}$, use (B.10) and to exploit that $R^3 v_s^2 = \frac{4\chi E_0}{25\rho_0}$ for Sedov-Taylor blastwaves

$$\frac{\bar{P}}{P_1} = \frac{75\varepsilon_{th}(\gamma^2 - 1)}{32\pi\chi} \tag{B.21}$$

Last two equations to derive the unknowns need to introduce a radial logarithmic derivative first

$$f^* \equiv \frac{\partial \ln(f)}{\partial \ln(r)} = \frac{\partial \ln(f_r)}{\partial \ln(\hat{r})} \tag{B.22}$$

to simplify the Euler equations of mass (3.5) and momentum (3.7). Partial derivatives of time and position are, using Sedov-Taylor velocity (2.8) to remove v_s

$$\frac{\partial f}{\partial r} = \frac{f}{\hat{r}R} f^* \tag{B.23}$$
$$\frac{\partial f}{\partial t} = f[\tfrac{\sigma}{v_s}\tfrac{\partial v_s}{\partial t} - \tfrac{v_s}{R} f^*] = -\tfrac{f}{5t}[3\sigma + 2f^*] \tag{B.24}$$

so Euler equations are now

$$\tfrac{2}{5t}\rho^* = \tfrac{v}{xR}(2 + \rho^* + v^*) \tag{B.25}$$
$$\tfrac{\rho v}{5t}(2\rho^* + 2v^* + 3) = \tfrac{\rho v^2}{xR}(\rho^* + 2v^*) + \tfrac{P}{\hat{r}R}P^* \tag{B.26}$$
$$\tag{B.27}$$

previous equations can be further simplified by computing the logarithmic derivatives of (B.12)-(B.14)

$$\rho^* = \tfrac{\rho_1\rho_2\rho_3\hat{r}^{\rho_2}}{\rho} \tag{B.28}$$
$$v^* = 1 \tag{B.29}$$
$$P^* = \tfrac{P_1 P_2 P_3 \hat{r}^{P_2}}{P} \tag{B.30}$$

introducing them into (B.25) and (B.26)

$$\tfrac{2}{5t}\rho_2\rho_3 = \tfrac{v_1}{R}(3 + \rho_2\rho_3) \tag{B.31}$$
$$\tfrac{\rho_1 v_1}{5t}(2\rho_2\rho_3 + 5) = \tfrac{\rho_1 v_1^2}{R}(\rho_2\rho_3 + 2) + \tfrac{P_1}{R}P_2P_3 \tag{B.32}$$

where I take $\hat{r} = 1$ as well to place this equation into the shock radius, where you can apply (B.8)-(B.10), plus $\frac{2}{5t} = \frac{v_s}{R}$ for Sedov-Taylor shocks, to reach the final equations

$$\rho_2\rho_3 = \tfrac{2}{\gamma+1}(3 + \rho_2\rho_3) \tag{B.33}$$

$$P_2P_3 = \tfrac{2\rho_2\rho_3(\gamma-1)+5\gamma-3}{2(\gamma-1)} \tag{B.34}$$

Solving (B.16) and (B.33) leads to

$$\rho = \rho_1\hat{r}^{\frac{6}{\gamma-1}} \tag{B.35}$$

That is, $\rho_2 = \frac{6}{\gamma-1}$ and $\rho_3 = 1$, which is the One Power Approximation solution of Ostriker and McKee (1988).

Likewise, pressure parameters come from solving (B.17) and (B.34), obtaining

$$P_2 = \tfrac{5\gamma+9-6(\gamma-1)(1-\frac{\bar{P}}{P_1})}{2(\gamma-1)(1-\frac{\bar{P}}{P_1})} \tag{B.36}$$

$$P_3 = \tfrac{(5\gamma+9)(1-\frac{\bar{P}}{P_1})}{5\gamma+9-6(\gamma-1)(1-\frac{\bar{P}}{P_1})} \tag{B.37}$$

In the case of $\gamma = \frac{5}{3}$, radial pressure can be written as

$$P \approx \frac{P_1}{5}(2 + 3\hat{r}^{22}) \tag{B.38}$$

Next, let me compute the radial profiles of number density and temperature for a monoatomic gas ($\gamma = \frac{5}{3}$). Number density is straightforward

$$n(\hat{r}) = \frac{4\rho_0}{\mu m_H}\hat{r}^9 \tag{B.39}$$

where $\mu \approx 0.6$ is the mean atomic weight and m_H the Hydrogen mass. Temperature is

$$T(r) = \frac{P}{nk_B} \approx \frac{\mu m_H}{20\rho_0 k_B}P_1(2\hat{r}^{-9} + 3\hat{r}^{13}) \tag{B.40}$$

being k_B the Boltzmann constant.

B.2.1 Validating approximate profiles

From this derivation, I have obtained

$$\rho = \rho_1\hat{r}^9 \tag{B.41}$$

$$v = v_1\hat{r} \tag{B.42}$$

$$P = \tfrac{P_1}{5}(2 + 3\hat{r}^{22}) \tag{B.43}$$

Figure B.1 compares this ansatz with a numerical Sedov-Taylor profile with an ISM number density $n_0 = 1$ cm^{-3} and $E_0 = 10^{51}$ erg. All profiles give a reasonable approximation to the numerical results, but velocity is overestimated.

Alternatively, you can also compute kinetic and thermal energies of the blastwave from (B.41)-(B.43). For a Sedov-Taylor shock, kinetic and thermal energies are constant in time, with $E_k = 0.283E_0$ and $E_{th} = 0.717E_0$. On the other hand, ansatz (B.41)-(B.43) yields:

$$E_k = \tfrac{1}{2}\int_V \rho v^2\, dV = \tfrac{9\pi\chi}{175}E_0 = 0.323E_0 \tag{B.44}$$

$$E_{th} = \tfrac{3}{2}\int_V P\, dV = \tfrac{354\pi\chi}{3125}E_0 = 0.712E_0 \tag{B.45}$$

This way, we know that pressure profile (B.43) is a great approximation with less than 1% of error, while density and velocity profiles are still good with a 15% error.

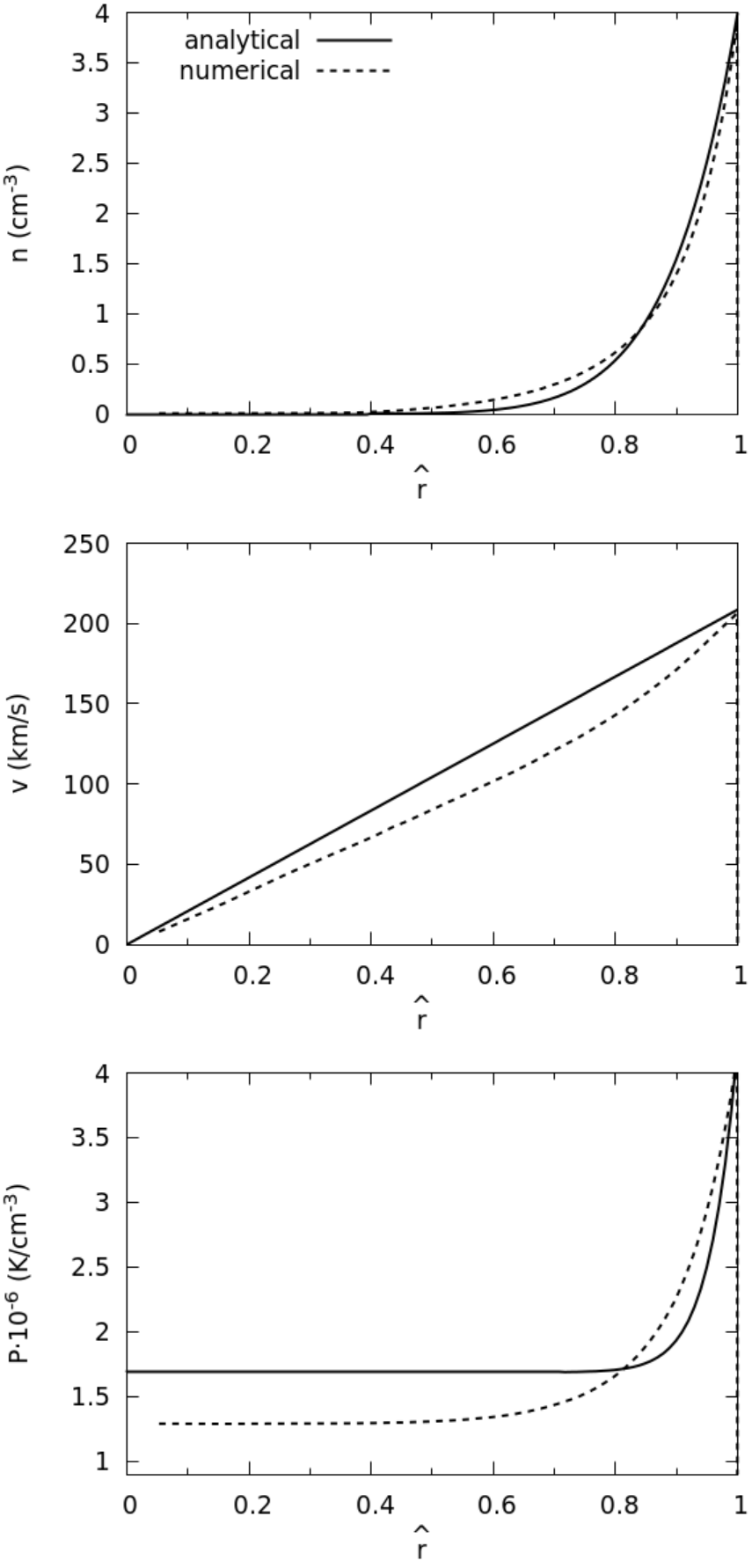

Figure B.1: Approximate density, fluid velocity and pressure profiles (solid line) against a numerical simulation (dashed line) at $t = 34\ kyr$, during the Sedov-Taylor phase of a SNR with ISM density of 1 cm^{-3} and $E_0 = 10^{51}\ erg$.

Appendix C

Euler Time Derivatives in Cylindrical and Spherical Coordinates

Here I show the full derivation for converting the Euler equations (3.5)-(3.7) into time derivatives (3.11). This is not the only option to generate these derivatives for cylindrical and spherical coordinates in 1D hydrodynamical simulations. For the interested reader, I refer to Wang and Johnsen (2017) for a discussion of different approaches.

In 3D, you can write mass (3.5) and energy (3.6) Euler equations in this manner:

$$\frac{\partial y}{\partial t} + \vec{\nabla} \cdot \vec{f} = \mathcal{U} \tag{C.1}$$

where $y = \{\rho, \epsilon\}$, $\vec{f}$ its fluxes and $\mathcal{U}$ the source terms. If we take the volume integral and apply the Divergence theorem to the flux term we have:

$$\frac{d}{dt}\int_V y \; dV + \oint_{\partial V} \vec{f} \cdot d\vec{A} = \int_V \mathcal{U} \; dV \tag{C.2}$$

Provided that space discretization is good enough (i.e. we can consider y and $\mathcal{U}$ to be a constant within the volume, which can be a cell), then

$$\frac{dy_i}{dt} \approx -\frac{1}{\Delta V}\oint_{\partial V} \vec{f} \cdot d\vec{A} + \mathcal{U}_i \tag{C.3}$$

ΔV is the cell volume

$$\Delta V = \frac{k_q}{q+1}(r_{i+\frac{1}{2}}^{q+1} - r_{i-\frac{1}{2}}^{q+1}) \tag{C.4}$$

where $q = \{1, 2\}$ and $k_q = \{2\pi, 4\pi\}$ for cylindrical and spherical coordinates, respectively; $r_{i\pm\frac{1}{2}}$ denotes the location of the left and right interface of the current i cell. Under spherical/cylindrical symmetry, the surface integral is easy to evaluate, as $\vec{f}$ is constant and normal to the cell surface:

$$\oint_{\partial V} \vec{f} \cdot d\vec{A} = k_q(r_{i+\frac{1}{2}}^q f_i^{(+)} - r_{i-\frac{1}{2}}^q f_i^{(-)}) \tag{C.5}$$

Combining previous two equations into (C.3), we get a finite-difference formula:

$$\frac{dy_i}{dt} = -(q+1)\frac{r_{i+\frac{1}{2}}^q f_i^{(+)} - r_{i-\frac{1}{2}}^q f_i^{(-)}}{r_{i+\frac{1}{2}}^{q+1} - r_{i-\frac{1}{2}}^{q+1}} + \mathcal{U}_i \tag{C.6}$$

This formula applies to mass, energy and entropy if dual energy formalism is included (see 3.1.1.3).

On the other hand, Euler equation for momentum is trickier. Equation (3.7) in vector notation reads like this

$$\frac{d\rho v}{dt} + \vec{\nabla}(\rho v^2 \hat{u}_r + P) = \mathcal{U} \tag{C.7}$$

where v denotes the velocity in the radial direction, and $\hat{u}_r$ is its unitary vector. We can repeat the same logic as above if we move the pressure to the right side of the equation, and consider its gradient as an extra source term. This leads to

$$\frac{d}{dt}(\rho v)_i = -(q+1)\frac{r_{i+\frac{1}{2}}^q (\rho v^2)_i^{(+)} - r_{i-\frac{1}{2}}^q (\rho v^2)_i^{(-)}}{r_{i+\frac{1}{2}}^{q+1} - r_{i-\frac{1}{2}}^{q+1}} - \nabla P + \mathcal{U}_i \tag{C.8}$$

and ∇P is a finite-difference

$$\nabla P = \frac{\partial P}{\partial r} \approx \frac{P_i^{(+)} - P_i^{(-)}}{r_{i+\frac{1}{2}} - r_{i-\frac{1}{2}}} \tag{C.9}$$

In order to recover an expression like (C.6), where fluxes are involved, I add and subtract this term

$$-(q+1)\frac{r_{i+\frac{1}{2}}^{q} P_i^{(+)} - r_{i-\frac{1}{2}}^{q} P_i^{(-)}}{r_{i+\frac{1}{2}}^{q+1} - r_{i-\frac{1}{2}}^{q+1}} \tag{C.10}$$

Hence

$$\begin{aligned}\frac{d}{dt}(\rho v)_i = &-(q+1)\frac{r_{i+\frac{1}{2}}^{q}(\rho v^2+P)_i^{(+)} - r_{i-\frac{1}{2}}^{q}(\rho v^2+P)_i^{(-)}}{r_{i+\frac{1}{2}}^{q+1} - r_{i-\frac{1}{2}}^{q+1}} + \\ &+(q+1)\frac{r_{i+\frac{1}{2}}^{q} P_i^{(+)} - r_{i-\frac{1}{2}}^{q} P_i^{(-)}}{r_{i+\frac{1}{2}}^{q+1} - r_{i-\frac{1}{2}}^{q+1}} - \frac{P_i^{(+)} - P_i^{(-)}}{r_{i+\frac{1}{2}} - r_{i-\frac{1}{2}}} + \mathcal{U}_i\end{aligned} \tag{C.11}$$

where the second and third terms of the right-hand side is the geometric term, $\mathcal{G}$, from (3.12).

Appendix D

Proof-of-Concept of a Radiative Transfer Code

A radiative transfer code was written before dropping it in favour of developing MIXCLASK. The purpose of this appendix is to make record of the existence of this code by outlining how it works and some test cases that a reader may find useful. This code has a Github[1] repository, dubbed NAIVERT (hereinafter NRT).

NRT is a ray-tracing `C++` code that computes the mean intensity, defined as

$$J_\lambda = \frac{1}{4\pi}\int I_\lambda d\Omega = \frac{1}{4\pi}\int_0^\pi \int_0^{2\pi} I_\lambda(\phi,\theta)\sin(\theta)\, d\phi d\theta \tag{D.1}$$

J_λ is obtained in 2D under the assumption of axial symmetry. In that regard, NRT needs a (R,z) map of the emissivity, j_λ, and opacity, α_λ. These parameters are needed from the radiative transfer equation (1.11) without photon addition due to scattering:

$$\frac{dI_\lambda}{ds} = j_\lambda - \alpha_\lambda I_\lambda \tag{D.2}$$

When an input has been provided, it computes $I_\lambda(R,z,\phi,\theta)$ by solving (D.2) in several lines of sight (ϕ,θ) for each point (R,z) given by the input using a Dormand-Prince integrator. In that regard, NRT considers lines that cross both the point (R,z) and a sphere centered in the origin $(0,0)$ with radius

$$r = \sqrt{R_{max}^2 + z_{max}^2} \tag{D.3}$$

That is, the diagonal of the simulation domain, and it is also the radius of the sphere that contains it. NRT finds the Cartesian coordinates where the line of sight crosses the sphere and computes the distance s to the (R,z) point. These computations give two valid solutions because they correspond to two different directions. First one gives the value of I_λ for (ϕ,θ) whereas the second one has angles $(\phi+\pi, \pi-\theta)$. This approach allows to loop ϕ between 0 an π instead to 2π.

Finally, mean intensity can be computed from (D.1) by summing pairs of I per (ϕ,θ) as

$$J_\lambda(R,z) \approx \frac{1}{4\pi}\sum_{\phi,\theta}[I_\lambda(R,z,\phi,\theta) + I_\lambda(R,z,\phi+\pi,\pi-\theta)]\sin(\theta)\Delta\phi\Delta\theta \tag{D.4}$$

D.1 Some test cases

One of the most easiest solutions to try is to solve the radiative transfer equation with $\{\alpha_\lambda, j_\lambda\}$ set to constants different to 0. That assumption gives the solution

$$I_\lambda(s) = \frac{j_\lambda}{\alpha_\lambda} + [I_\lambda(0) - \frac{j_\lambda}{\alpha_\lambda}]e^{-\alpha_\lambda s} \tag{D.5}$$

where s denotes the distance between the point and the simulation border. Although computing J_λ from (D.1) is not trivial with (D.5), you can simplify above solution by taking $s \to \infty$ (i.e.: far from the border), so $J_\lambda = j_\lambda/\alpha_\lambda$.

[1] https://github.com/MarioRomeroC/NaiveRT

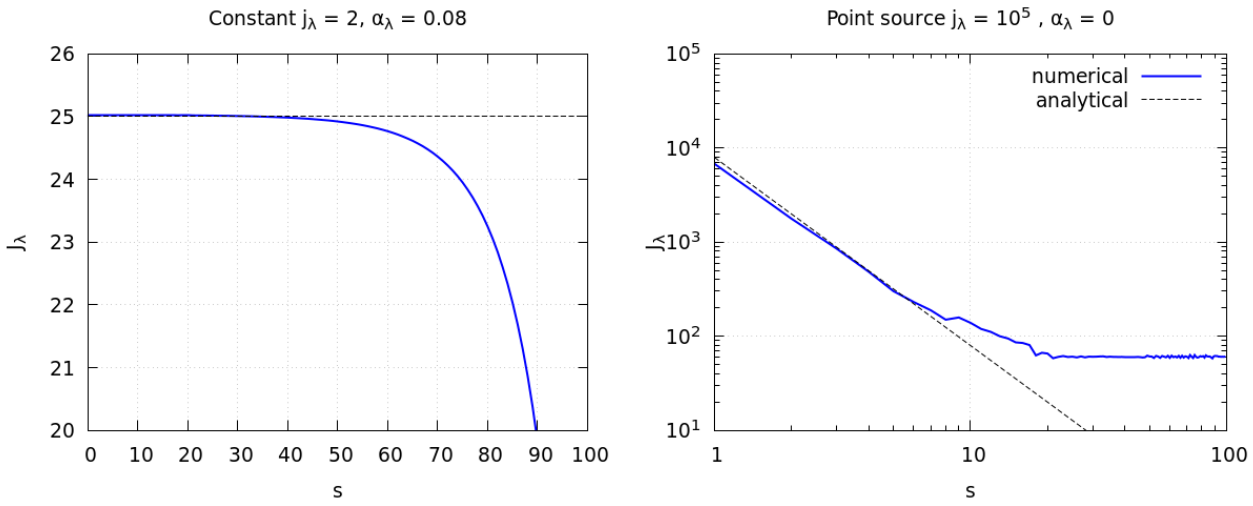

Figure D.1: Diagonal profiles (i.e.: Points along the line $R = z$) of both cases proposed in D.1, along with its analytical solution. All quantities are in favourite units.

On the other hand, you can also find analytical solutions with $\alpha_\lambda = 0$ because I_λ is just the integral of j_λ in the line of sight. For example, take a discrete source centered at the origin, which have an emissivity

$$j_\lambda = j_{\lambda,0} \frac{\delta(s)}{4\pi s^2} \tag{D.6}$$

where δ is the Dirac Delta function, and s the distance to the source. Integrating I_λ and then J_λ is now trivial, giving

$$J_\lambda = \frac{j_{\lambda,0}}{4\pi s^2} \tag{D.7}$$

Figure D.1 shows how well NRT performs against these two simple cases in a simulation box of $R_{max} = z_{max} = 100$ in the diagonal axis (i.e.: $z = R$) to cover the maximum distance inside the domain.All results are in favourite units and for an arbitrary wavelength. Left panel displays the case where the whole region have a constant $j_\lambda = 2$ and $\alpha_\lambda = 0.08$, yielding an analytical solution of $J_\lambda = 25$. The agreement is very good until $s = 50$ where border effects start to be important. On the other hand, NRT struggles to handle the point source far from it. This suggested that launching rays into several directions needed a much more refined approach to deal with discrete sources.

Although this code is functional, it was decided to not develop it further and use SKIRT instead because it would take a very long time to reproduce the same results of Chapter 4 with an own code.